Heliyon 10 (2024) e24689

Contents lists available at ScienceDirect

Heliyon

journal homepage: www.cell.com/heliyon

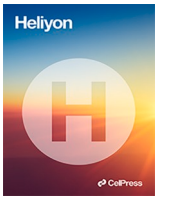

Review article

Development on inverted perovskite solar cells: A review

Emmanuel A. Nyiekaa [a,d,*], Timothy A. Aika [a], Patience E. Orukpe [a], Christopher E. Akhabue [b], Eli Danladi [c]

[a] Department of Electrical and Electronics Engineering, University of Benin, Benin City, Nigeria
[b] Department of Chemical Engineering, University of Benin, Benin City, Nigeria
[c] Department of Physics, Federal University of Health Sciences, Otukpo, Nigeria
[d] Department of Electrical and Electronics Engineering, Joseph Sarwuan Tarka University Makurdi, Nigeria

ARTICLE INFO

Keywords:
Inverted perovskite solar cells
Photovoltaic parameters
Transport layers
Fabrication methods
Additive and interface engineering

ABSTRACT

Recently, inverted perovskite solar cells (IPSCs) have received note-worthy consideration in the photovoltaic domain because of its dependable operating stability, minimal hysteresis, and low-temperature manufacture technique in the quest to satisfy global energy demand through renewable means. In a decade transition, perovskite solar cells in general have exceeded 25 % efficiency as a result of superior perovskite nanocrystalline films obtained via low temperature synthesis methods along with good interface and electrode materials management. This review paper presents detail processes of refining the stability and power conversion efficiencies in IPSCs. The latest development in the power conversion efficiency, including structural configurations, prospect of tandem solar cells, mixed cations and halides, films' fabrication methods, charge transport material alterations, effects of contact electrode materials, additive and interface engineering materials used in IPSCs are extensively discussed. Additionally, insights on the state of the art and IPSCs' continued development towards commercialization are provided.

1. Introduction

The rate of energy consumption is on the rise daily as a result of high energy demand due to increase in global population. About 80 % of energy consumed globally is supplied by fossil fuel which causes environmental issues which necessitated the advancement of renewable energy usage [1]. The solar energy is considered as the most prominent and significant because of its abundant, clean and inexhaustible nature which makes it the most promising candidate among all sources of renewable energy. The use of solar energy is cheap and environmentally friendly [2]. Three generations of solar cells have been identified: wafer-based for the first generation, thin-film-based for the second generation, and inorganic-organic materials called perovskite for the third generation. Several kinds of solar cells, including monocrystalline and polycrystalline silicon solar cells [3,4], copper indium gallium selenide (CIGS) solar cells [5,6] cadmium telluride (CdTe)-based solar cells [7,8] quantum dot sensitized solar cells [9] organic photovoltaic [10] and perovskite solar cells [11] have also been explored by researchers.

Perovskite Solar Cells (PSCs) have gained much research consideration in modern eras as a result of their improved efficiencies, low processing temperatures and cost of fabrications. Many researches have been carried out on PSCs led to improved energy power conversion efficiencies (PCEs) from 3.8 % in 2009 to over 25 % after a decade [12]. Regular mesoporous structure, regular planar

* Corresponding author. Department of Electrical and Electronics Engineering, University of Benin, Benin City, Nigeria.
E-mail address: emmanuel.nyiekaa@eng.uniben.edu (E.A. Nyiekaa).

https://doi.org/10.1016/j.heliyon.2024.e24689
Received 4 September 2023; Received in revised form 22 December 2023; Accepted 12 January 2024
Available online 14 January 2024

structure, and inverted planar structure are all possible configurations for perovskite solar cells as shown in Fig. 1a-c respectively.

The front electron transport material (ETM) in conventional perovskite devices is often an n-type mesoporous TiO_2, which needs to be thermally processed at high temperatures. The device experiences hysteresis issues when the mesoporous layer's thickness is decreased [14,15]. The aforementioned difficulties make it expensive to manufacture traditional devices and further limit their ability to produce satisfactory results. With increased electron mobility and stability under UV radiation, low-temperature processed SnO_2 has been adopted as an ETM, improving the efficiency of power conversion of regular devices [16,17]. On the other hand, the device configuration and charge transport direction are reversed in inverted PSCs (IPSCs).

Despite tremendous research advances in PCSs, inverted planar PSCs have received less attention, hence few studies have been carried out in this area of study. Therefore, intense research is required in this field of study in order to improve and maximize their performances as their conventional counterparts' structures. In this review paper, inverted perovskite solar cells is of attention for reasons that it requires simple fabrication process, minimal hysteresis, tunable bandgap, low temperature solution preparation, good stability and its suitability for flexible solar cells fabrications [18].

3.9 % efficiency was attained using the first IPSC with the configuration of ITO/PEDOT:PSS/$CH_3NH_3PbI_3$/PCBM/BCP/Al, which was proposed in 2013 [19]. Two years later, 15 % PCE with over 1000 h of light stability was produced in an inverted structure using PSCs with validated efficiencies of over 1 cm^2 [20]. The verified PCE of inverted PSCs surpassed 22 % in 2020 for the first time after several years of research [21]. After that, in 2022, the certified PCE of inverted PSCs exceeded 23 %, 24 %, and 25 % [22–25]. Additionally, inverted perovskite mini-modules with an area of 50 cm^2 in 2021 and 12.84 cm^2 in 2022 achieved verified PCEs of 19.2 % and 21.07 %, respectively [26,27], which is closer to regular mini-modules' record efficiency [28]. It should be noted that under the recently specified damp heat test condition stated by IEC 61215:2016, inverted PSCs could retain 95 % of their initial efficiency for more than 1000 h [24,29]. The aforementioned development clearly demonstrates that inverted PSCs have greater benefits in the manufacturing of PSC modules in both small and large areas that are stable and effective, meaning that inverted PSCs have greater industrialization potential. Table 1 and Fig. 19 summarizes the specific performance parameters of selected inverted PSCs.

The current developments in high PCE of IPSCs are discussed in this paper. The present status of inverted PSC research, such as the formation of perovskite arrangements, manufacturing techniques, charge transport alteration and back electrode materials (BEMs) are outlined, to enhance progress in stability and efficiency of these devices. We specifically draw attention to the advancements in materials that transport charge carriers and the impact of additive and interfacial engineering on the functionality of inverted PSCs. In order to lower material costs to achieve commercialization, improve stability and efficiency of inverted PSCs, we conclude with some remarks and future research outlook.

2. Advances in perovskite configurations

$MAPbI_3$ is known as most popular perovskite used in the earlier inverted PSCs. But because of its inherent and thermal instability [30], as a result of its reversible/irreversible breakdown reactions even at low temperatures [31], $MAPbI_3$ is not suited for usage in real-world applications. Because the FA cation forms a stronger hydrogen connection with the PbX_6 octahedra than the MA cation, it displays superior thermal stability. FA cation starts a reversible breakdown reaction below 85 °C [32,33], and over time, it has progressively taken over as the primary cation in nearly all excellent performing IPSCs. Scientists discovered that replacement of MA^+ with FA^+ in perovskites for IPSCs might boost short circuit current (J_{SC}) for the reason that FA^+ could lower the bandgap and ensured that absorption spectrum of perovskite films are widen [34,35]. Partly replacement of MA^+ with FA^+ to achieve $FA_{0.85}MA_{0.15}Pb(I_{0.85}Br_{0.15})_3$ as the light harvester by Huang et al., the J_{SC} of the resulting PSC of about 1 mA cm^{-2} much more than that of the $MAPbI_3$-based PSC was achieved [36], thus enhancing device performance. Furthermore, Zhu et al. evaluated the impacts of various perovskite configurations on device behaviour and discovered that the J_{SC} of PSCs made from FA^+ was considerably greater than that of PSCs made from MA^+ (25.38 against 23.26 mA cm^{-2}) [24]. In addition, partial substitution of Cs^+ for MA^+ improved the quality of the perovskite film by effectively controlling the rate of crystallization by increasing the entropy of crystallization [37]. Furthermore, the disparity in size between FA^+ and Cs^+ was shown to generate lattice strain and chemical pressure, which strengthened the hydrogen bond between I^- and FA^+ and octahedral tilting. These effects reduced intensity of vibration and enhanced the thermal stability of the perovskite structure [38,39].

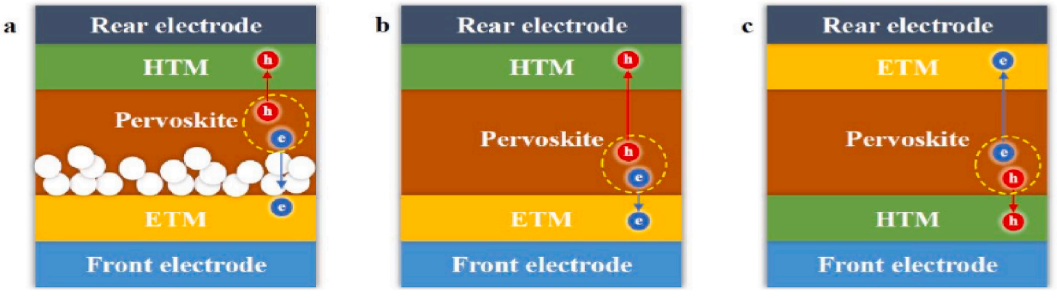

Fig. 1. Configurations for devices using perovskite solar cells. (a) Regular mesoporous structure, (b) Regular planar structure, (c) Inverted planar structure [13].

Furthermore, in order to handle the 1.34 eV ideal bandgap based on the S-Q limit, the configurations of the widely used perovskite have changed from the original $MAPbI_3$ to FAMA or FACs, CsMAFA, and CsFAMA-guanidinium (GUA)-based perovskites [25,40]. The band gap of pure $FAPbI_3$ is optimally narrow. The largest organic cation that works well with three-dimensional (3D) perovskite crystal formations is FA^+. These structures are commonly used absorbers in conventional PSCs with improved performance. FA^+ has been used successfully in standard PSCs [41,42]. However, because α-$FAPbI_3$ is hard to crystallize and pure $FAPbI_3$ has low phase stability by nature, it is not frequently used in inverted PSCs as a photoactive layer. Consequently, a number of successful methods for maintaining the black phase of $FAPbI_3$ and enhancing the shape and perovskite films' crystallinity have been documented [43,44]. Methylammonium chloride (MACl), which has been effectively employed to improve the performance of conventional device structures, is the popular additive used to ensure superior black phase $FAPbI_3$ crystallization through the production of a transitional stage [45–47].

Nevertheless, it has been noted that the appropriate $FAPbI_3$ annealing temperature in widely used hole-transport materials for IPSCs is 150 °C, which is not the optimal temperature for $FAPbI_3$. Furthermore, residual additive can create a radiative-free recombination epicenter in the ultimate $FAPbI_3$ film and destabilize the film [48,49]. In as much as the self-assembled monolayer (SAM)-based inverted PSC efficiency using $FAPbI_3$ barely surpassed 22 % [48], the perovskite active layer with PCE greater than 25 % of inverted PSCs with quadruple or triple cations still outperforms it [24,25]. As a result, $FAPbI_3$ is not as competitive as double or triple cations light absorbers due to difficulties in creating perovskite layers and the decreased stability and efficiency of the finished product.

2.1. Inverted perovskite solar cell configurations

Transparent conductive oxide (TCO), HTL, light absorbing layer, ETL, and back electrode layer are the typical components of an IPSC. Other subcategories of IPSCs include planar, mesoporous, bulk heterojunction (BHJ), and graded heterojunction (GHJ). Planar heterojunction with a donor-acceptor interface was employed in the first inverted device, eliminating the need for the mesoporous TiO_2 layer to undergo a high thermal treatment and significantly streamlining the production process [19]. Some research groups have used NiO_X-based mesoporous nanoparticles at the interface of compact $NiO_X/MAPbI_3$ to improve the hole-extraction capacity of HTMs. Then, with the help of Indium tin oxide (ITO), dense NiO_X, NiO_X nanoparticles, $MAPbI_3$, PCBM, BCP, and Al created the first mesoporous IPSCs, achieving a PCE of 9.15 % [50].

Nevertheless, mesoporous NiO_X hinders further device performance enhancement due to its increased internal coefficient of light absorption and poorer hole mobility. In the tiny $NiO_X/MAPbI_3$ interface, a very transparent Al_2O_3 inert scaffold has been introduced, successfully filling the ultrathin NiO_X pinholes without affecting light absorption and blocking potential shunt channels in between PCBM and NiO_X. By effectively preventing holes flowing backwards from FTO to perovskite, which lowers non-radiative recombination and increases the fill factor (FF) with a PCE of above 13 % from 62 % to 73 %, the band alignment of the materials found that the −4.7 eV E_F of FTO is much deeper than the HOMO of Al_2O_3 [51].

To minimize the inequity in $MAPbI_3$'s hole and electron mobility and to lessen the photocurrent hysteresis of the device, the first inverted BHJ device was reported by adding PCBM to the perovskite [52]. It is apparent that increase in the mobility of charge carrier and a healthy stability between the hole and electron mobility are the causes of the decreased photocurrent hysteresis. The V_{OC} and FF of the device were finally lowered as a result of the substantial non-radiative recombination caused by a further increase in Phenyl-C_{61}-butyric acid methyl (PCBM) concentration in the perovskite. The heterogeneous nucleation of the perovskite was regulated by

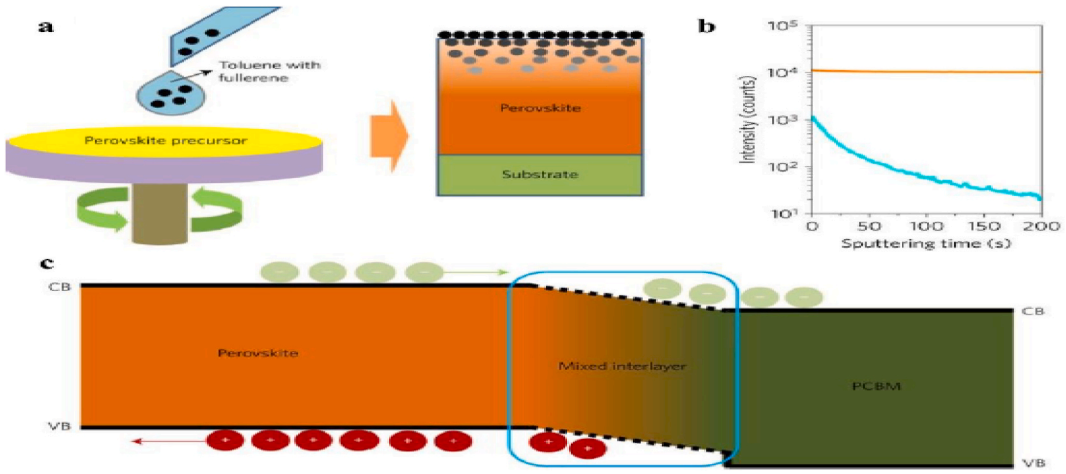

Fig. 2. The schematics and the GHJ plan. (a) Diagrammatic illustration procedure of the one-step dripping, (b) The GHJ film's ToF-SIMS profile made using the dripping technique, exhibiting S (cyan) and I (orange) and components for PCBM and perovskite respectively, from the front to the back, (c) Schematic illustration of perovskite and PCBM band shift in the structure of GHJ [13]. (For interpretation of the references to colour in this figure legend, the reader is referred to the Web version of this article.)

adding ZnO, an inorganic n-type semiconductor, as a nucleate site to a precursor. The FF and V_{OC} of a BHJ ZnO-perovskite with improved crystallinity of perovskites were synthesized [53].

It has been predicted that a halide lead perovskite based on formamidinium (FA) with a narrower badgap, which has a broader spectrum of absorption than methylammonium (MA), may further enhance the device's short-circuit current (J_{SC}) [54]. However, the FA-based perovskite film's carrier transport has a lower electron transport capacity than that of holes, and the needed distance for electron diffusion in IPSCs is significantly greater than that for holes. As an antisolvent, a PCBM solution in toluene was used, and a GHJ method and schematic procedure have been developed, as illustrated in Fig. 2a [55]. The perovskite was further penetrated by molecular PCBM with further annealing, creating a GHJ PCBM-perovskite with a manageable distributed composition. Based on the profiles obtained using secondary ion mass spectrometry time-of-flight, the amount of sulfur (S) found in the ETM demonstrated a steady and consistent decline from the back to the GHJ's film front, overlaps $FAPbI_3$ with the iodine (I) signal as shown in Fig. 2b. This indicates formation of perovskite-PCBM GHJ. As seen in Fig. 2c, which provided 18.21 % PCE containing an aperture region greater than 1 cm^2, the gradient distribution of PCBM increased the electron extraction in IPSCs based on $FAPbI_3$ by creating gradient of energy level on the mixed-perovskite/PCBM interface. According to the authors' hypothesis, which was supported by earlier research [56], the carbonyl groups and cyano on the Isodicentric (IDIC) molecule's lone pair electrons can successfully passivate the unsaturated Pb ions' dangling bond defects on the perovskite's surface. Symmetry in IDIC's molecular structure also contributed to the non-polarity, which boosted the heterojunction's hydrophobicity.

3. Tandem solar cells with IPSCs

In general, tandem solar cells, whether two or four terminal offer a viable technique to get above the efficiency thresholds. However, due to fewer electrodes and window layers of four-terminal tandem solar cells, two-terminal tandem solar cells exhibit characteristics that are suitable for industrial use. Due to its sharp optical absorption edge, constant variable bandgap range of 1.48–2.23 eV, acceptable V_{OC} of around 1.15 V, and dependability on the constituents of halide anions, perovskite is an appealing material for use with Cu(In,Ga)Se_2 and silicon photocells [57]. As a result of their parasitic absorption and operational stability compared to ordinary IPSCs, transparent and stable IPSCs treated at low temperatures are believed to be superior candidates for Cu(In, Ga)Se_2/perovskite, silicon/perovskite, and tandem all-PSCs [58]. An effective 1.67 eV bandgap in a triple-halide (Cl, Br, I) perovskite top cell that is well matched was created for use with silicon solar cells, and it attained 16.83 % PCE for semitransparent IPSCs with top lighting of 1 cm^2 aperture area. A top cell, two-terminal tandem device and silicon cell integration achieved a PCE of 27 % [59]. A hybrid 2D–3D perovskite with a broad bandgap of 1.68 eV for silicon/perovskite tandem solar cell with two terminals has been produced, and a PCE of 26.7 % was attained [60]. This was done without changing the perovskite components. By improving the linking layer's optical transparency and electrical connectivity, a 22.43 % PCE for Cu(In,Ga)Se_2/perovskite tandem two-terminal solar cells has been attained [61]. Vertical surface roughness of bottom cells was successfully decreased to 40 nm from 250 nm via sputtering of ITO, chemical, and ZnO/Cu(In,Ga)Se_2 that has been mechanically polished, making it possible to deposit 300–600 nm perovskite and attained a PCE of 24.2 % [62]. The use of transport materials that are metal oxide charge-based made up of hydroxyl groups apparently caused the oxidation of Sn^{2+}, which is restricted by the Pb–Sn perovskites' narrow bandgaps. In tandem solar cells made entirely of perovskite, the inverted structure employing organic charge transport carriers like PEDOT:PSS is therefore preferred. In a reaction of proportionation, metallic tin was employed to convert Sn^{4+} to Sn^{2+}, yielding a PCE of 22.1 % in all tandem-based perovskite solar cells [63]. Further research was conducted by this team of researchers, which resulted to the development of a triple-junction PSC with a PCE greater than 20 % [64]. However, IPSCs increase the potential for combining PSCs with either Cu(In,Ga)Se_2 or silicon for solar energy applications to produce tandem solar cells of over 40 % efficiency [65].

4. Advances in perovskite fabrication techniques

To reduce current leakage caused by unwanted connection between the electron transport materials (ETMs) and the hole transport materials (HTMs) and to enable effective generation and collection of charges, a compacted, homogeneous, and superior perovskite layer is essential. Device performance and film quality can be impacted by fabrication techniques. Choosing appropriate film manufacturing technique is essential to producing PSCs with good efficiency. For inverted PSCs, a wide range of film fabrication techniques have been applied. Four popular manufacturing techniques for highly efficient inverted PSCs are explained in the subsections that follows.

4.1. Vacuum deposition

The thermally evaporated precursor materials react to create films of perovskite on a substrate during vacuum deposition. The production of uniform, dense, and conformal perovskite films is guaranteed by the vacuum deposition technique, even in cases when the substrate surface is not wettable [66]. Another significant benefit of vacuum deposition, when compared to the benefits of the solution approach, is the ability to regulate film shape and thickness needed to achieve homogeneity of spatial performance, especially for significant PSC units. For instance, Bolink et al. methodically investigated how the thickness of the perovskite film affected the IPSCs' performance and used 500 nm-thick $MAPbI_3$ layers to reach an efficiency of 16.5 % without hysteresis [67]. Furthermore, the multisource vacuum deposition technique was reported by Stranks et al. which allowed them to regulate the addition of PbI_2 via vacuum deposition, and their inverted PSCs attain a consistent power output efficiency of 18.2 %. This technique produced high-quality and favorable film morphology and photoelectric characteristics in perovskite films of $FA_{0.7}Cs_{0.3}Pb(I_{0.9}Br_{0.1})_3$ [68]. Park

et al. used vacuum deposition to create perovskite films as well as to deposit an n-butylammonium bromide (BABr)-based passivation layer at the interface between the perovskite and PCBM. They obtained a remarkable 21.4 % efficiency for the fabricated inverted PSCs [69].

Vacuum deposition has been effectively used in industrial processes, but its widespread application is limited by a number of issues, including excessive cost, complexity, energy usage, and low use of basic materials. Furthermore, vacuum-deposited perovskite films still lack sufficient crystalline quality. The one and two-step solution techniques have merits over vacuum deposition, including low cost and direct fabrication process.

4.2. Two-step solution method

For typical PSCs, the two-step solution approach has been thoroughly researched since it provides for more flexible means of control of crystallization process of perovskite when compared to the one-step method. Singular component growth in the perovskite precursor is simpler than controlling the growth of several components [70]. PbI_2 tends to create a dense layer when a planar structure is fabricated using the two-step solution procedure. The PbI_2 film is difficult to penetrate by the ensuing organic cation solution, which often only reacts with the film's surface, leaving leftover PbI_2 in the final perovskite film. In normal PSCs, high PbI_2 positively reduces interfacial charge recombination. However, recent research has also shown that excess PbI_2 is harmful to PSCs' long-term stability. Moreover, under light irradiation, the photolytic excess of PbI_2 into Pb and I_2 metallic raises the transfer resistance of charges in inverted PSCs. Thus, the primary difficulty with the "two-step" approach for inverted PSCs is realizing the thorough transformation of PbI_2 to perovskite. By spin coating methyleammonium iodide (MAI) solution on top of the PbI_2 layer to create stacked films, Huang et al. enhanced the conventional two-step process for IPSCs in order to address this issue. The heat hardening process created $MAPbI_3$ as a result of MAI diffusing into and reacting with PbI_2. PbI_2 was completely transformed to perovskite by carefully regulating the layer thickness. This process yielded improved perovskite films' quality with bigger grain sizes with the aid of solvent annealing. With a high FF of 77.5 %, the resultant PSCs had a great efficiency of 15.6 %. Within the same time, Wu et al. discovered that PbI_2/dimethylformamide (DMF) solution containing 2 wt percent water (denoted as PbI_2-2) could be formed into smooth, continuous, improved films quality with complete coverage by adding a modest amount of H_2O [71]. The two-step approach produced PbI_2-2-based perovskite films that were smooth, compact, and free of pinholes. As a result, the equivalent best cell had an astounding FF of 85 % and an amazing PCE of 18 %. The improved films' quality of the perovskite with huge sizes of grains were produced using post-treatment of the DMF vapor during the perovskite hardening procedure. This increased the shunt-resistance and inhibit interfacial recombination of carriers, leading to high J_{SC} and V_{OC} values. As a result, the matching best inverted PSC demonstrated an exceptionally high efficiency of 20.1 % [71]. Presently, the recorded PCE for inverted PSCs using the two-step approach is 22.5 % [72], which is still inferior to the reported PCE for inverted PSCs using the one-step approach that achieved a PCE of 25.37 % [25].

The use of one-step approach to creating perovskite films has replaced the two-step method as the most popular way to create high-efficiency inverted PSCs. This could be due to (i) the two-step method's conversion of PbI_2 into perovskite is inefficient, particularly when controlling the ambient air's humidity [73], and (ii) the roughness of the perovskite films produced using the two-step process is typically on the order of tens of nanometers. A thin coating of PCBM or C_{60}, around 30 nm thick, cannot effectively cover such films, in as much as 200 nm spiro-OMeTAD is non-responsive to such a considerable irregularity. A significant factor influencing the photo-based performance of IPSCs is the thickness of the PCBM or C_{60} layer. When PCBM or C_{60} thickness increases, the FF of a PSC drops significantly, suggesting that a small ETL thickness is essential for lowering series resistance and facilitating extraction of charges [74–76]. Therefore, in order to achieve a small ETL thickness for an improved efficiency in IPSCs, a thin perovskite surface is essential. This need is satisfied by the one-step approach, which is discussed in the sub-section that follows.

4.3. One-step solution method

One-step solution method is a popular approach for inverted PSCs used for deposition of perovskites, just like for conventional PSCs. Using this technique, the substrate is immediately coated with precursor solution of the perovskite composed of organic ammonium salt, metal halide, and the appropriate solution. For high-efficiency PSCs, the spin coating-based one-step solution approach typically calls for an antisolvent extraction step. Antisolvent extraction, to put it briefly, is a fabrication procedure in which a rotating precursor solution of perovskite is created using the one-step approach and treated with an antisolvent to quickly remove the solvent. This allows the perovskites to grow immediately without the emergence of any intermediary species [77]. The antisolvent's primary job is to swiftly eliminate surplus solvents and produce a large quantity of crystal nuclei to generate the ammonium halide-PbI_2-perovskite solvent phase, resulting in uniform and smooth perovskite's films [78]. Note that antisolvent is a solvent, like ethyl acetate (EA), chlorobenzene (CB), and toluene (TL), that has poor solubility for the perovskite but suitable with the precursor solvent of the perovskite. Choosing the right antisolvent is essential to producing high-quality perovskite films. Wu and colleagues conducted a thorough investigation of the impact of several antisolvents, such as isopropyl alcohol (IPA), dichlorobenzene (DCB), TL, CB, and chloroform (CF), on the perovskite films' morphology [79]. The reason for the improved form and large grains in the perovskite film treated with TL was toluene's low dielectric constant, which pushed the precursor of the perovskite into the metastable state instead of the super saturation state (CF, CB, DCB, or IPA) during dropwise addition [79]. The perovskite layer's colours were either light brown or brown, however, after applying different antisolvents (CF, CB, or DCB) to the perovskite precursors, smaller grain sizes resulted from it, since it demonstrated greater nucleation rates when compared to the growth rates of crystals after treatment with antisolvent.

Apart from the choice of solvent, the length of time (Δt) that an antisolvent is applied has a substantial effect on the perovskite films's shape [80]. Vaynzof et al. created perovskite films with 14 distinct antisolvents by altering the pace at which the antisolvent

was applied in order to examine the effects of extrusion rates and antisolvent application time. They discovered how organic iodides dissolve in the antisolvent and the antisolvent's miscibility with perovskite host fluids determine how quickly or slowly an antisolvent is applied. When they are applied fast, the host solvent did not have enough time to permeate into the antisolvent across the liquid-liquid contact, resulting in rough films. High-performance inverted PSCs with PCEs above 21 % and superior perovskite films were achieved by controlling the application rate of each antisolvent and observing how the aforementioned antisolvents affected the device's performance. Applying the one-step solution technique to antisolvents, the IPSCs' PCE has attained an astounding value of over 25 % thus far [25], decreasing the disparity in performance among different configurations of PSCs. High-quality perovskite films have also been produced using vacuum flash-assisted and gas-assisted techniques, in addition to the antisolvent method. These techniques are based on comparable perovskite growth processes and nucleation [81,82].

4.4. Other methods

The aforementioned techniques for manufacturing have proven effective when used for PSCs with small area size, which are typically spin-coated. However, because of the centre-pulled force needed to quickly eliminate the solvents like dimethylsulfoxide (DMSO) or dimethylformamide (DMF) when the substrate is rotating quickly and the challenges associated with the antisolvent dropping process, this technology might not be appropriate for scale-up and commercialization [83], as it will typically results in large-area perovskite films of low quality with pinholes and rough surfaces. Since the dehydrating procedure is anticipated to be the step that determines the rate at which the perovskite phase crystallizes, the solvents' characteristics are therefore very important [84]. Therefore, the fabrication of improved large surface area perovskite films hinge on the improvement of precursor solvents and novel construction methods. Scalable manufacturing techniques, like slot-die and blade coating, have been popular in this regard and are mostly utilized for inverted PSCs and modules [85,86].

Regulating the pace of perovskite crystal nucleation and growth is one challenge these large-area perovskite film production techniques encounter [65,84]. PSC stability and efficiency are typically harmed by rapid crystallization at low temperatures, which produces poorly crystalline, highly defect-filled, and small-grained perovskite films. Typically, a slower and higher temperature technique is used to manufacture perovskite films with large grain sizes and high crystallinity [85]. Therefore, for PSCs that are robust and highly efficient, a compromise amid the poor crystallinity brought on by fast deposition and the requirement for large grains and high crystallinity is crucial. In order to do this, Huang et al. used acetonitrile (ACN) and the extremely volatile 2-methoxyethanol (2-ME) as DMF's replacement. In order to create a mixture that served as the perovskite precursor's solvent for coating blades, they combined them in a specific ratio with the low volatility-coordinating DMSO solvent as demonstrated in Fig. 3a [85].

Being that DMSO disappears significantly into air gently when compared to other solvents, the solution/solid mixture's capacity to

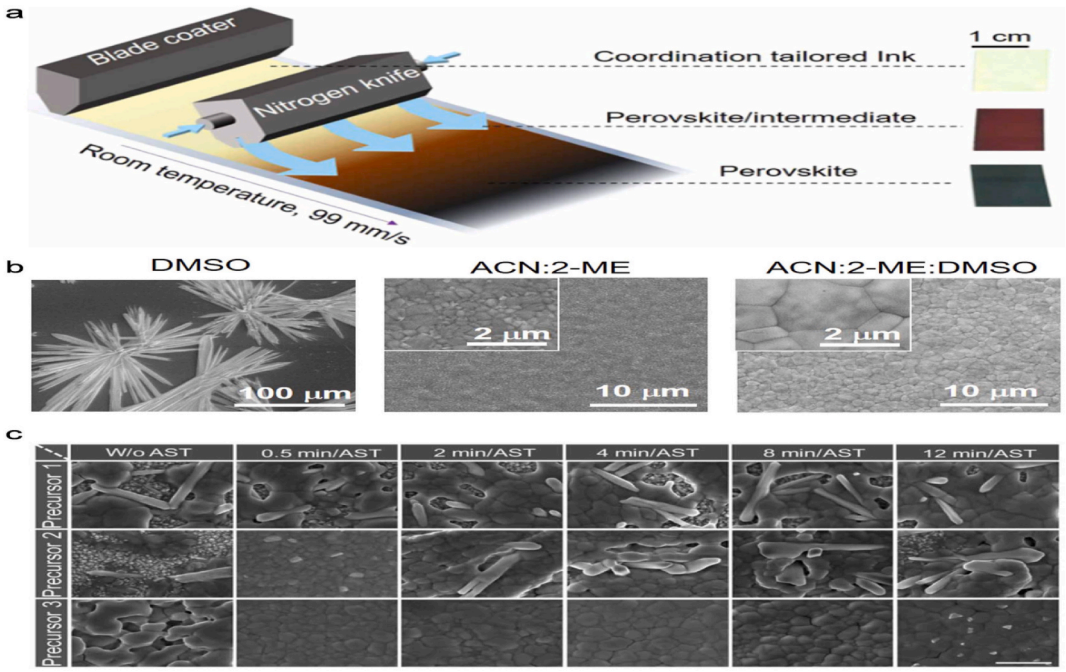

Fig. 3. Typical production techniques for large-scale perovskite solar panels. (a) Diagram showing the production of perovskite films utilizing coordination-tuned perovskite ink and a room temperature N_2-knife-assisted blade coating moving at 99 mm/s, (b) SEM pictures of perovskite films made by blade coating in various solvent systems, (c) Morphology evolution of the perovskite films manufactured via annealing at 150 °C for 30 min after slot-die coating with or without treatment using antisolvent for varied periods of time using DMF, DMF-NMP, and DMF-NMP-DPSO as precursor solvent 1, 2, and 3 respectively [87].

coordinate with DMSO is enhanced until the DMSO disappeared from the films that were still coated. Large grain sizes are produced while quickly drying perovskite films at ambient temperature because the speed rate at which the solvent evaporates influences the compact film generation and the crystallization processes of perovskite in blade coating (Fig. 3b). Large-area, homogenous perovskite films were successfully produced using this method at ambient temperature with an ultrafast speed of 99 mms^{-1}. Using this technique, an IPSC module with an area of more than 60 cm^2 produced a 16 % boost in efficiency. In their subsequent study, blade coating achieved 19.2 % steady-state certified efficiency with a 50.0 cm^2 aperture area for perovskite modules [26].

Similar to blade coating, excellent quality mass area $MAPbI_3$ perovskite films are also frequently formed using slot-die coating [88] for perovskite solar panels that exhibit remarkable device functionality [89]. Nevertheless, the device's long-term stability is limited by its volatile characteristics and heat breakdown [30]. Because of their superior thermal stability, it is therefore preferable to design modules using field aligned currents (FACs) perovskites in order to satisfy commercialization requirements. Unfortunately, slot-die coated FACs-based perovskite modules are hardly documented due to the nucleation and complex nature of the crystal formation process caused by soluble nature of Cs^+ precursors in the presence of halogen ions [90]. In order to do this, Chen et al. used diphenyl sulfoxide (DPSO), an inert Lewis base additive to produce perovskite ink including FACs from DMF-N-methyl-2-pyrrolidinone (NMP)-DPSO. During the process of slot-die coating, DPSO was utilized to successfully delay the natural perovskite nucleation and increase the nucleation energy barrier in order to produce moist films with a high coverage. The damp films were submerged in n-hexane, a less hazardous antisolvent for extraction purpose. As a result, in just 8 min, the DMF-NMP-DPSO precursor generated uniformly sized and compact perovskite films (Fig. 3c). With a stabilized 16.63 % quasi efficiency and a 20.77 cm^2 active area, the resulting inverted perovskite solar modules generated this result. These developments demonstrate that choosing the right solvent is essential to producing improved perovskite modules. In order to create improved perovskite films of large surface area (>50 cm^2) for industrialization, it is necessary to grow solutions that could control the nucleation and crystallization of perovskite films.

5. Fabrication of $MAPbX_3$ perovskite films for IPSCs applications

When compared to traditional γ-butyrolactone (GBL), N, N-dimethylformamide (DMF) was utilized as the perovskite precursor's solvent and resulted in an enhanced distribution of $MAPbI_3$ film on the PEDOT:PSS substrate, with fine granules [19]. According to the authors, DMF is more flammable and promotes the creation of extra $MAPbI_3$ fine grains since its boiling point is lower than that of γ-GBL, which is 205 °C. Furthermore, the steadiness of the perovskite crystal is enhanced by the greater surface free energy brought on by tiny grains. After that, the perovskite film's production was optimized by a mixture of γ-GBL and DMF with a modest boiling point, which eliminated the microscopic pinholes between the grains [91]. However, there were numerous defects in the produced perovskite film, such as granular bounds, which led to low J_{SC} and V_{OC} values of 10 mA cm^{-2} and 0.7 V respectively. The thick $MAPbI_3$ film with improved coverage was then prepared using the vacuum deposition technique. A greater than 16 mA cm^{-2} in the J_{SC} was attained after the application of a 285-nm-thick $MAPbI_3$ [92]. Additionally, an IPSC device structure fabricated by enhanced vacuum deposition made $MAPbI_3$ layer of 500 nm-thick produced a J_{SC} that is greater than 20 mA cm^{-2} and a 15.8 % PCE [93]. The quality of the crystal film created remained subpar, which is an indication that the selected vacuum deposition process significantly improved uniform $MAPbI_3$ thick film. In comparison with vacuum deposition approach, the solution technique also showed clear merits which include ease of manufacturing and cheap rate. The treatment of the ITO/NiO_X substrate with ultraviolet ozone enhanced the perovskite precursor's wettability. After spin-coating PbI_2 film's layer onto the substrate of ITO/NiO_X, the authors submerged it in an IPA solution of MAI that is warm to create the photo-harvester as depicted in Fig. 3c [94]. The device's J_{SC}, however, remained low (13.1 mA cm^{-2}), probably because of the MAI's inability to fully change PbI_2 into $MAPbI_3$ inside the thick PbI_2 film and the film's increased roughness

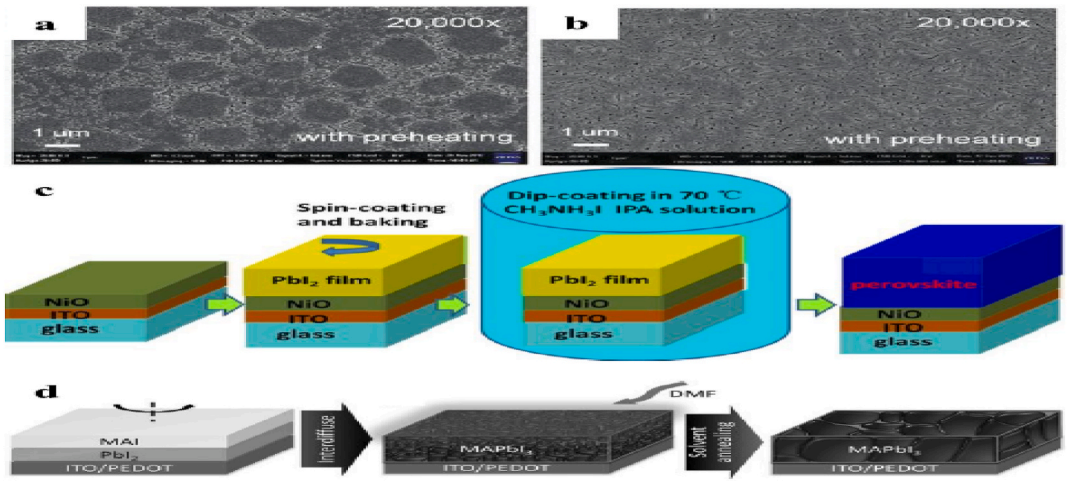

Fig. 4. Spin-cast of $MAPbI_3$ perovskite films. (a) Solution of DMF (b) γ-GBL on the heated substrate shown as scanning electron microscopy (SEM) images, (c) The successive deposition of $MAPbI_3$ onto a planar NiO_X layer shown schematically, (d) Diagrammatic representation of the solvent and process of inter-diffusion annealing [13].

as a result of $MAPbI_3$'s quick crystallization during the dip casting process.

A flat, 280-nm-hick PbI_3 with 19.6 mA cm^{-2} J_{SC} was created by MAI inter-diffusion while annealing using the first inter-diffusion approach that has been proposed, in which the ITO/PEDOT:PSS substrate was coated with a DMF solution of PbI_2 and then with an IPA solution of MAI using spin method [95]. Although $MAPbI_3$ was produced using this method for a carrier diffusion length between 100 and 130 nm, which made it difficult to extract photo-induced carriers from the perovskite and led to insignificant improvement in J_{SC} as film thickness grew. The wet environment that was required and the precursor ions and molecule long-distance diffusion were promoted by the solvent annealing, which outperformed the conventional annealing processes. Due to this, the grain size and perovskite's carrier diffusion length were significantly increased, and a PCE of 15.6 % and a J_{SC} of over 21 $mAcm^{-2}$ were obtained. After that, the one-step preparation of $MAPbI_3$ (Cl) film using IPA/DMF mixed solvent annealing was successful, prevented the excessive dissolving of DMF in perovskite and enhanced the film's crystal quality, which increased the device's PCE and J_{SC} to 18.9 % and 22.23 $mAcm^{-2}$ respectively [96]. Perovskite film quality can be improved by additive engineering, which has been shown to be successful [97]. The spin-cast of $MAPbI_3$ perovskite films is demonstrated as DMF's solution (Fig. 4a) and γ-GBL on the heated substrate as scanning electron microscopy (SEM) image (Fig. 4b). The successive deposition of $MAPbI_3$ onto a planar NiO_X layer is schematically shown as Fig. 4c while the diagrammatic representation of the solvent and process of inter-diffusion annealing as Fig. 4d. The immersion of the fine-grained perovskite sheet in the IPA-NH_4SCN solution is necessary to ensure that the SCN, a perovskite component dissolves into a continuous intermediate rod form due to a strong contact, which eliminates a significant amount of grain borders, in order to improve the grain size and the perovskite film's crystallinity after being produced using an antisolvent fast-crystallization technique. The intermediary film is then hardened to create a perovskite film with larger grains and fewer defects with improved PCE, as illustrated in Fig. 5 [98]. There is no doubt that moisture speeds up the destruction of the perovskite layer due to the breakdown of perovskite into PbI_2 and volatile MAI. The dissolution of PbI_2 in a DMF solvent, however, has been shown to be significantly improved by drop amounts of H_2O, leading to the formation of an improved crystallinity and homogeneity in PbI_2 film, which aided in the development of top-notch light harvesters and further enhanced the electrical connection between PEDOT:PSS and $MAPbI_3$ [99]. The ideal device had a PCE of 18 % and a high FF of 85 %. It also had a 0.5 vol% H_2O additive. The perovskite crystalline quality was then increased, and the authors were able to produce a PCE of above 20 % by adding controlled H_2O to the IPA solution of MAI [100].

To produce excellent $MAPbI_3$ film utilizing a single-step approach procedure, a two-fold additive approach using the ionized solvent molecules of MAAc (methyl ammonium acetate) and TSC (thio-semicarbazide) compounds that resemble thiourea has been proposed as shown in Fig. 6a [101]. The authors showed how the TSC and MAAc persist in film that has been spun-coated and aid in homogenous perovskite grain development and nucleation, which can be completely eliminated after the annealing procedure as seen in Fig. 6b. Fig. 6c, however, depicts perovskite with MAAc as the only additive. Perovskite's crystallization is slowed down by the potent interface between Pb^{2+} and TSC, the perovskite's grain size drastically enhanced, as seen in Fig. 6d. The MAAc TSC dual additives perovskite film had more diffraction peaks than the sample based purely on MAAc, which suggests that the $MAPbI_3$ film has enhanced crystalline and preferred orientation, as shown in Fig. 6e. In IPSCs at the time, the device with a 1.025 cm^2 aperture managed to attain a PCE of 19.19 %. The device demonstrated remarkable thermal stability because of its high crystalline quality after 500 h at 85 °C aging, maintaining 80 % of its initial efficiency. According to other researchers, perovskite precursor received additives to influence the process of crystallization and nucleation, including Poly(trimethylolpropane triacrylate), rhodanine derivatives, HI, MAI, and $Pb(Ac)_2$ [102–104].

6. Fabrication of $FAPbX_3$ perovskite films for IPSCs applications

$FAPbI_3$ outperforms $MAPbI_3$ in terms of thermal stability and has a wider absorption spectrum. Researchers have suggested a gradual annealing technique to enhance $FAPbI_3$'s crystal quality and an IPSC of ITO/PEDOT:PSS/$FAPbI_3$/PCBM/BCP/Ag configuration was made [105]. For 20 min, the precursor film for perovskite was successively heated to 100, 120, and 140° Celsius, as opposed to the one-step strengthening approach (140 °C/20 min). In order to prevent component volatilization, the distance at which precursor

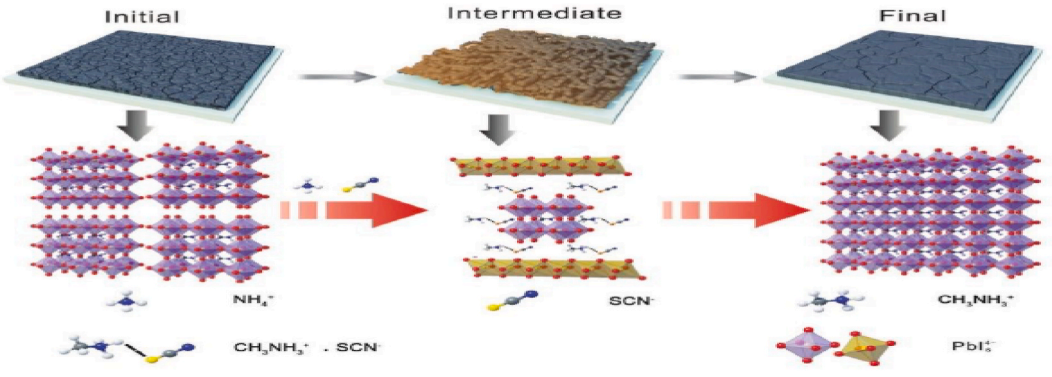

Fig. 5. The schematic picture of the $MAPbI_3$ films' recrystallization process [13].

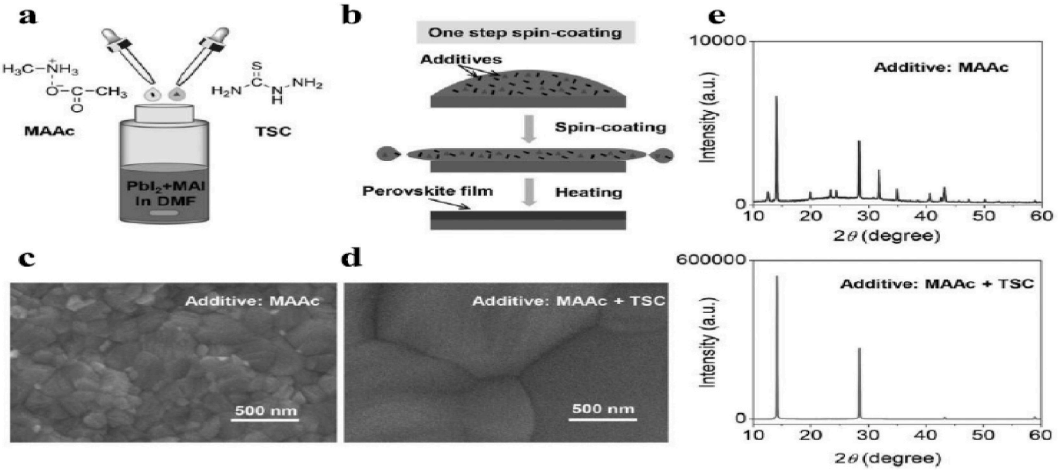

Fig. 6. Ionized solvent molecules of MAAc (methylammonium acetate) and the thio-semicarbazide molecule that resembles thiourea used in a dual additive method. (a) Additive engineering using stoichiometric DMF-solvent PbI_2-MAI precursor solution to combine molecular additive of TSC and an ionic additive of MAAc, (b) Diagrammatic representation of the additively one-step assisted deposition approach for films perovskite, excluding the use of vacuum or any auxiliary processes, (c) SEM pictures of $MAPbI_3$ films made with MAAc additions, (d) SEM pictures of $MAPbI_3$ films made using MAAc and TSC as precursor solution additives, (e) The pattern of X-ray diffraction [13].

molecules and ions' diffusion rate was increased. This minimized the defects and $FAPbI_3$'s grain boundaries and improved the J_{SC} for the best devices ranged between 14.73 mA cm^{-2} and 21.48 mA cm^{-2}, with a 13.56 % PCE.

Additionally, it has been shown that incomplete replacement of FA cations by partial MA in $FAPbI_3$ significantly enhances the perovskite's crystal quality. This is most likely because the precursor's increased configuration entropy successfully retarded the crystallization of the photo-harvester. However, excessive MA replacement will threaten $FAPbI_3$'s broad spectrum absorption, which has an impact on J_{SC} improvement. After antisolvent treatment, the IPA solution of volatile MACl was spin coated onto the yellow phase (δ-$FAPbI_3$) in order to increase crystallinity without compromising perovskite purity [106]. During the following annealing

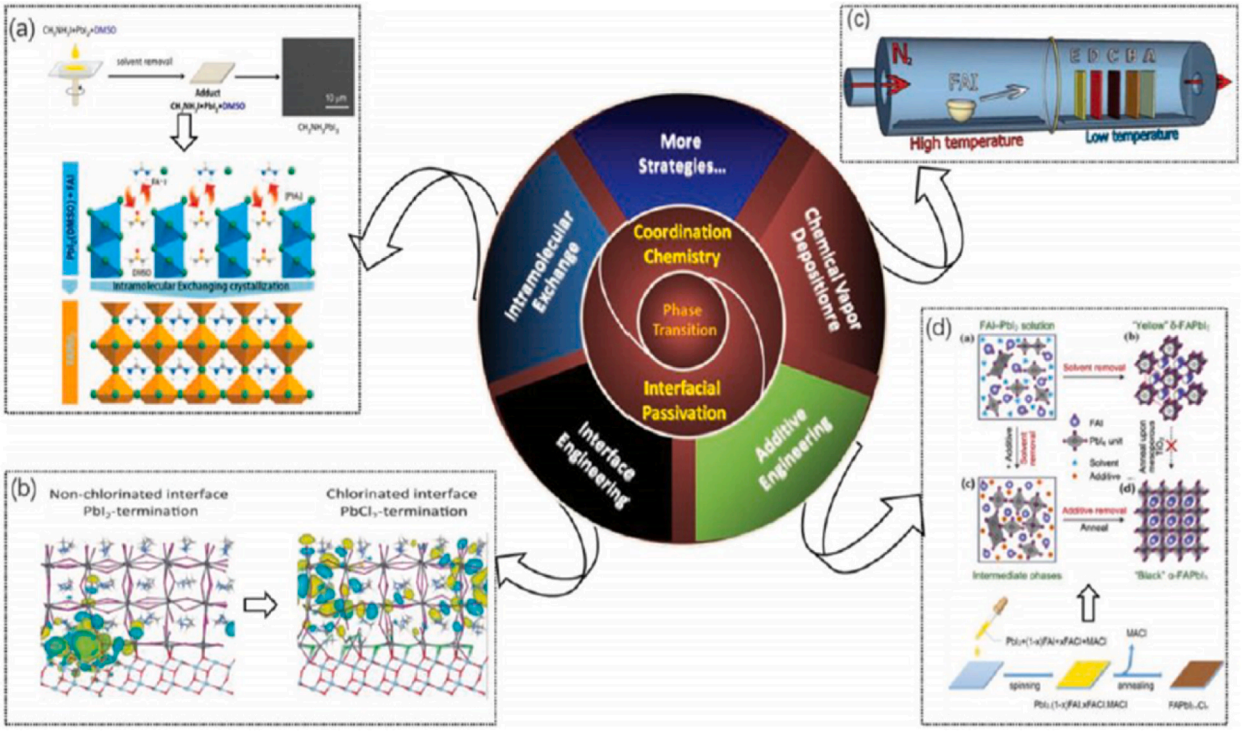

Fig. 7. An illustration of common approaches to address phase-transition issues in the production of superior FA-based perovskite films. (a) Intramolecular exchange, (b) Interface engineering, (c) Chemical vapor deposition, (d) Additive engineering [107].

procedure, the penetration of MACl successfully accelerated the switching to the active black phase (α-$FAPbI_3$) from the dominant yellow phase (δ-$FAPbI_3$). Additionally, MACl caused the active black phase, $FAPbI_3$, to vertically crystallized, which enhanced photon separation of the photo-generated carrier and absorption. As a consequence, inverted $FAPbI_3$-based devices attained outstanding stability using a 500-h light exposure period and thermal ageing, achieved a PCE of 20.65 % and a J_{SC} that is higher than 23 mA cm^{-2}. The obtained results point to $FAPbI_3$'s capacity in IPSCs, where additional optimization through additive and interface engineering is needed as discussed in section 13.1 and 13.2 respectively.

There are few researches on the use of $FAPbI_3$ as a photo-harvester in inverted structure devices. This is perhaps because it does not crystallize completely on NiO_X HTMs and normal poly[bis(4-phenyl)(2,4,6-trimethylphenyl)amine (PTAA)]. In order to create high-performance PSCs from improved FA-based perovskite films, various techniques have been employed for regular device configurations which incorporate intramolecular exchange, interface engineering, chemical vapor deposition (CVD) and additive engineering as demonstrated in Fig. 7a-d respectively.

7. Mixed-cation lead perovskite films

In order to stabilize the crystalline structure of $FAPbI_3$, MA^+/FA^+ mixed-cation perovskite can change the perovskite tolerance level to fall between 0.9 and 1.0 [108]. The entropy increase effect, when used to dope inorganic cations like Cesium (Cs^+), has proven to be an effective way to regulate the rate at which perovskite crystallizes, hence enhancing the film's quality [109]. Researchers have shown that the incompatibility of the ion sizes of organic monovalent cations with Cs^+ can lead to both lattice strain and chemical pressure, which lowers perovskite's intensity of vibration and increases the thermal stability of the devices and light harvester [110, 111]. In general, creating homogeneous perovskite films with numerous cations is challenging, although optimization of the fabrication process for additive engineering can help with this. A drop of an additive for semiconductor containing a group of rhodamine and a chlorobenzene (CB) antisolvent, for instance, was tested on intermediary films made of $(FAPbI_3)_{0.8}(MAPbBr_3)_{0.2}$ [112]. The tertiary amine group's strong Lewis acid-base interaction with the precursor of the perovskite caused the SA-treated perovskite's grain size to rise to the micrometer scale. As a result, the distribution of semiconductor additive with high conductivity at the grain boundaries facilitated the transit of photo generated carriers. With a PCE of 20.3 % and a V_{OC} of 1.13 V, the inverted device's J_{SC} was increased from 20.4 $mAcm^{-2}$ to 22.4 mA cm^{-2}. Similar to this, perovskite with mixed-cations (FA, MA, Cs)Pb(I, $Br)_3$ carrier transport was enhanced by using the poly (bithiophene imide) (PBTI), the n-type conductive additive solution as an anti-solvent in CB [113]. The electron's lone pair of an atom on the PBTI have successfully passivated the hanging bonds at the perovskite grain borders of the unsaturated Pb ion, essentially maintaining the perovskite film's ability to resist non-radiative recombination.

For the preparation using dual precursors, perovskite films with mixed cations (FA,MA)PbI_3 produced in a single step method was also developed [114]. For a mixed-cation perovskite precursor film to be made, researchers uniformly combined the PbI_2/FAI and Pb $(Ac)_2$/MAI solutions in DMF after which the substrate was spin coated with the mixture. With 20.15 % PCE and a consistent 20 % output power at the tracking maximum power point, the device's J_{SC} was increased to 23.09 mA cm^{-2} from 19.57 mA cm^{-2}. An antisolvent containing guanidinium bromide was dripped over the surface of a perovskite based on (FA, MA)Pb(I,$Br)_3$ meant to reduce the grain and lead halide boundaries considering the fact that the major challenge of IPSCs is the low V_{OC} [115]. Furthermore,

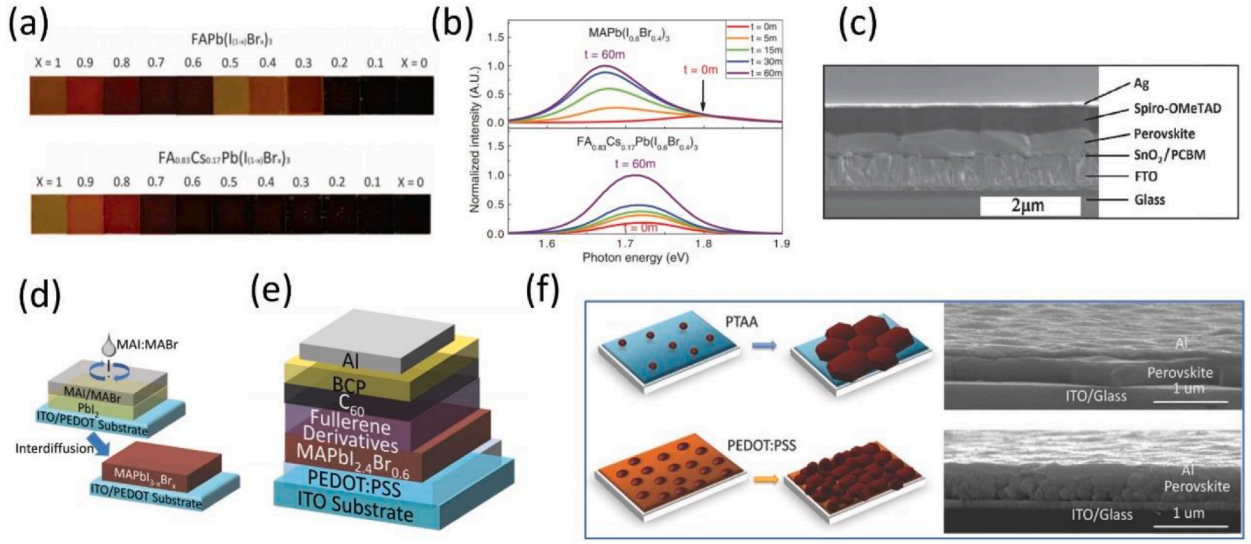

Fig. 8. Progress of wide-bandgap perovskite solar cells. (a) Images of the films $FA_{0.83}Cs_{0.17}Pb(I_{1-x}Br_x)_3$ and $FAPb(I_{1-x}Br_x)_3$, (b) PL spectra of the films $FA_{0.83}Cs_{0.17}Pb(I_{0.6}Br_{0.4})_3$ and $MAPb(I_{0.6}Br_{0.4})_3$ following exposure to light, (c) Scanning electron microscopy (SEM) picture of a wide-Eg PSC with n-i-p structure in cross-section, (d) The technique of sequential deposition, (e) A p-i-n configuration of PSC device structure (f) Diagrams and SEM cross-sectional pictures of PEDOT:PSS and PTAA deposited on ITO substrates [117].

according to other researchers, the PCE have been raised from 16.75 % to 20.05 % using the tiny Lewis base 2-acetylpyridine to successfully passivate Lewis acid defects at the perovskite IPSC top interface [116]. The alkylamine ligands (AALs) that attach the surface of long-chain olamines (OAm) were added to the perovskite precursor $Cs_{0.05}(FA_{0.92}MA_{0.08})_{0.95}Pb(I_{0.92}Br_{0.08})_3$. During the production of the light harvester's film, long-chain AALs were dispersed at the perovskite intermediate's grain boundaries. Due to the strong interaction between the amino groups and the perovskite grains, a film with orientation-dominant structure produced has fewer defects per unit than a film that is orientated randomly. The ITO/PTAA/perovskite/C_{60}/BCP/Ag configuration of inverted device was able to achieve confirmed V_{OC} of 1.14 V and certified PCE of 22.3 % [21]. Modern IPSCs are mostly built using lead perovskite materials with mixed cations. Additionally, hybrid halides like Cl–I and Br–I are frequently used to change the bandgap, tolerance factor, and crystallization in those perovskites.

7.1. Wide bandgap perovskite solar cells

Low-bandgap PSCs, CIGS, and Si in tandem applications are best suited for wide-bandgap PSCs having bandgaps of 1.7–1.9 eV. In iodide-based perovskites, this bandgap range is usually achieved by partially replacing I with Br; a larger bandgap is produced by a higher Br content [117]. Eperon et al. (2013) began studying the tunability of bandgap of $MAPb(I_{1-x}Br_x)_3$ [118] and $FAPb(I_{1-x}Br_x)_3$ [119], respectively, which marked the beginning of the investigation of perovskite solar cells with wide energy bands. Although the tunability of bandgap ranging from 1.5 to 2.3 eV is highly appealing for tandem-based solar cell applications, but the inherent photo-instability of the materials has caused the development of wide-bangap PSCs to lag far behind that of medium-bandgap (~1.6 eV) PSCs [120]. Although a lot of work has been done on how to mitigate mixed I–Br perovskites' instability, but substantial advancements were not made until late 2015 and early 2016. The discovery was achieved by Snaith and colleagues, who showed a number of effective wide-bandgap PSCs using perovskites based on FA/Cs, which are much phase stable than perovskites based on MA under thermal and optical stressors [121]. A comparison of a series of films with varying Br concentrations is shown in Fig. 8a. The "yellow phase" for x range from 0.3 to 0.6 is seen in $FAPb(I_{1-x}Br_x)_3$ films as a result of the phase change from a hexagon-shaped non-phase perovskite to a phase perovskite [122]. The second set of films exhibit a continuous color change as the Br concentration is raised. More significantly, as shown by the PL spectra in Fig. 8b, mixed-cation perovskites of FA/Cs showed superior stability in structure compared to perovskites made from MA following prolonged exposure to light. The J_{SC} of 19.4 mA cm^{-2}, PCE of 17.1 %, FF of 75.1 %, and V_{OC} of 1.2 V were obtained from the improved device, which had 1.74 eV in the n-i-p structure (Fig. 8c). One of the most

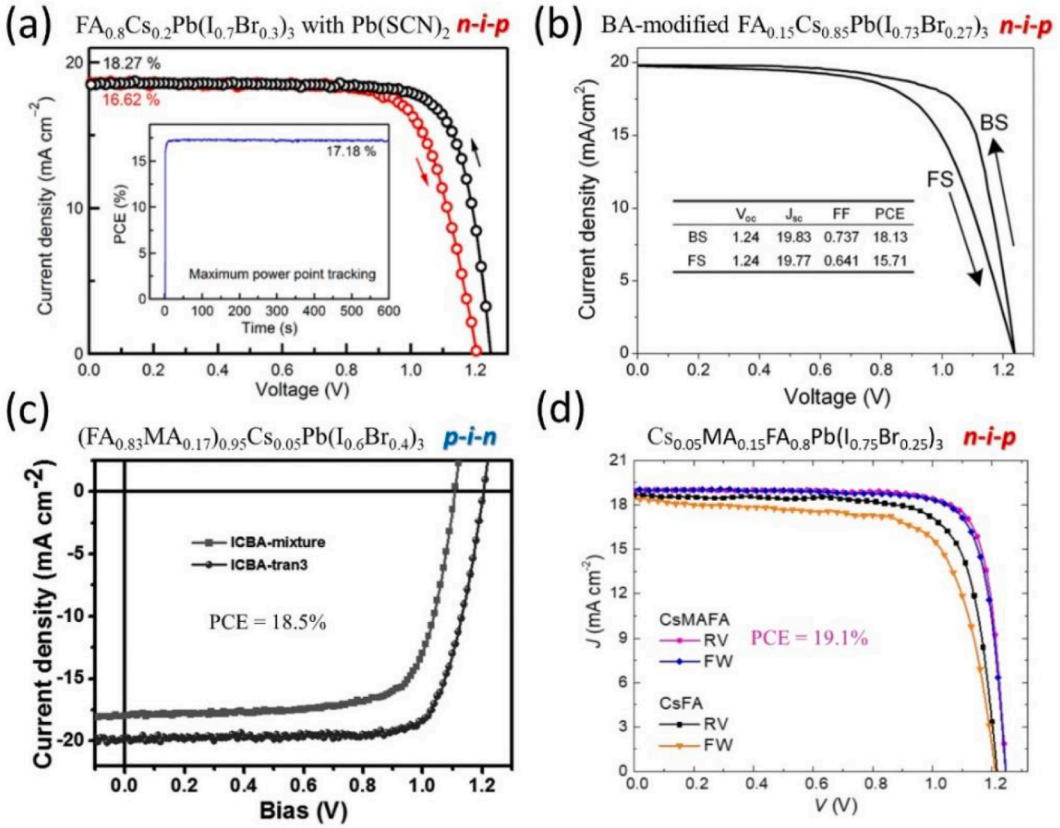

Fig. 9. J–V curves of the prominent bandgap PSCs of; (a) n-i-p $FA_{0.8}Cs_{0.2}Pb(I_{0.7}Br_{0.3})_3$, (b) n-i-p BA-$FA_{0.15}Cs_{0.85}Pb(I_{0.73}Br_{0.27})_3$, (c) p-i-n $(FA_{0.83}MA_{0.17})_{0.95}Cs_{0.05}Pb(I_{0.6}Br_{0.4})_3$, and (d) n-i-p $Cs_{0.05}MA_{0.15}FA_{0.8}Pb(I_{0.75}Br_{0.25})_3$ [117].

widely used options for the wide-band gap PSCs known is $Cs_yFA_{1-y}Pb(I_{1-x}Br_x)_3$ compositions.

The Huang group made another important contribution by using a low-temperature sequential deposition technique to create films of $MAPbBrxI_{3-x}$ with a bandgap between 1.7 and 1.75 eV [123,124]. According to Fig. 8d of the approach, an ITO/HSL substrate was first spin-coated with a PbI_2 layer, and then MAI/MABr was spin-coated with an isopropanol solution and annealed. Utilizing PTAA and PEDOT:PSS as the hole selective layer (HSL) respectively, PCEs for p-i-n wide-bandgap PSCs were demonstrated to reach 13.1 % and 16.6 % as shown in Fig. 8e [123,124]. Notably, the perovskite precursor solution's non-wettability due to PTAA encourages the formation of high-aspect-ratio crystalline grains, resulting in a large-sized flat surface (Fig. 3f), which is advantageous for lowering recombination and enhancing V_{OC} [125]. Consequently, PSCs with PTAA HSLs, a PCE of 14.9 % and 1.21 V V_{OC} were obtained using 1.75 eV $MAPb(Br_{0.27}I_{0.73})_3$ perovskite absorber layers.

Following that, a variety of processing techniques have been used to enhance performance of the device, such as the addition of additives and post-deposition annealing, with the goal of enhancing the wide-bandgap perovskite films' electrical quality. Duong et al. were able to produce 1.73 eV n-i-p type PSCs with a 17.4 % PCE with an inadequate V_{OC} of ~1.15 V when RbI was added to the $FA_{0.75}MA_{0.15}Cs_{0.1}Pb(I_{0.67}Br_{0.33})_3$ perovskite [126]. Yu et al. used the synergistic effects of solvent annealing and additive of $Pb(SCN)_2$ to improve the grain size of the perovskite films; this approach produced wide-bandgap PSCs of the n-i-p type with a 17.18 % stabilized efficiency and an improved 1.25 V open circuit voltage (Fig. 9a) [127]. Zhou et al. applied the appropriate amount of $Pb(SCN)_2$ to $FA_{0.8}Cs_{0.2}Pb(I_{0.73}Br_{0.27})_3$ and obtained a PCE of 18.6 % with a high V_{OC} of 1.244 V, thereby confirming the effect of adding $Pb(SCN)_2$ [128].

Modifying the interface is a crucial tactic for improving PSC stability and efficiency. Recombination of photoexcited charge carriers is caused by the surface and grain border ionic defects of perovskite films, which lowers the photovoltaic cell's output. Defect passivation and surface modification have enabled PCE increase in wide-Eg PSCs. Zhou et al. treated the 1.72 eV wide-bandgap $FA_{0.15}Cs_{0.85}Pb(I_{0.73}Br_{0.27})_3$ surface with benzylamine (BA). Grain boundaries are passed through three perovskite sheets. Under the forward scans, the modified BA-based devices with regular configuration showed a considerable J-V hysteresis but a PCE of 18.1 % and a V_{OC} of 1.24 V (Fig. 9b) [129]. In order to coat perovskite absorber's surface with quaternary ammonium halides so as to passivate grain boundaries and surface ionic defects, Huang and colleagues (2017) established a method to improve the wide-bandgap PSCs's performance [130]. Defect passivation raised PCEs to 17.2 % and reduced the wide-bandgap $FA_{0.83}MA_{0.17}Pb(I_{0.6}Br_{0.4})_3$ cells with the p-i-n structure's V_{OC} deficit to 0.57 V at 1.72 eV. The combination of ESL, PTAA HSL, and $(FA_{0.83}MA_{0.17})_{0.95}Cs_{0.05}Pb(I_{0.6}Br_{0.4})_3$ absorber created 1.71 eV wide-bandgap PSCs in the follow-up work [131]. Compared to standard ICBA, ICBA-trans3 offers enhanced alignment of energy levels using wide-bandgap perovskites, which increased PCE from 14.6 % to 18.5 % (Fig. 9c).

According to the Sargent group, adding a formamide co-solvent causes the black phase perovskite to reduce defect density by avoiding the intermediate phase's formation [132]. A V_{OC} of 1.23 V and 17.8 % PCE were shown for wide-bandgap PSCs using this technique. They also came up with a way to fix the severe wide-bandgap perovskites traps by mixing FA/Cs and MA perovskites [133]. They obtained a high V_{OC} of 1.22 V and PCE of 20.7 % for 1.65 eV PSCs based on $Cs_{0.05}MA_{0.15}FA_{0.8}Pb(I_{0.75}Br_{0.25})_3$ absorbers. According to Fig. 9d–a PCE of 19.1 % and a V_{OC} of 1.25 V for 1.74 eV of $Cs_{0.12}MA_{0.05}FA_{0.83}Pb(I_{0.6}Br_{0.4})_3$, were generated. This is one of the greatest PCE known for the n-i-p structure and wide-bandgap PSCs that have been documented in the literature thus far. Although, it is among the finest V_{OC} deficits documented in the works, the V_{OC} shortfall of under 0.5 V is still smaller than that of its counterparts with lower bandgaps.

However, in typical perovskite films with wide-band-gap, the defects brought on by ion migration result in a significant open-circuit voltage (V_{OC}) deficit. Perovskite-based tandem solar cells have lately been shown to be viable options for the upcoming generation of solar energy systems, according to Jian et al. The authors used a novel technique called "green-solvent strategy," for the deposition of the perovskite layer with a bandgap of 2.0 eV using isopropanol and nontoxic acetic acid as solvents in the ambient atmosphere. Perovskite films' inherent defects were stabilized by the *in situ* generated acetate anions. These characteristics significantly increased phase stability of 2.0 eV $Cs_{0.2}FA_{0.8}PbI_{0.9}Br_{2.1}$ perovskite and produced the equivalent power conversion efficiency of 10.62 % and the open circuit voltage of 1.325 V as shown in Fig. 10 [134].

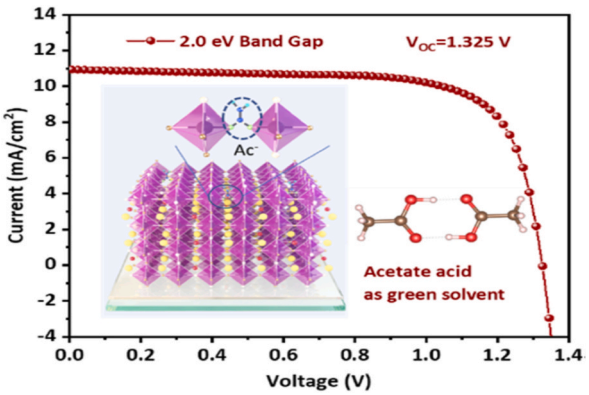

Fig. 10. Plot of J_{SC} Vs V_{OC} using $Cs_{0.2}FA_{0.8}PbI_{0.9}Br_{2.1}$ as perovskite film [134].

7.1.1. Problems and difficulties of perovskite solar cells with wide-bandgap

The V_{OC} and PCE values of prominent wide-bandgap PSCs that have been published in recent years is presented in Fig. 11. As previously mentioned, wide-bandgap PSCs have made remarkable progress, but their V_{OC} deficits remain significantly bigger than those of their counterparts with lower bandgaps (<1.6 eV), which usually have V_{OC} deficits of less than 0.4 V (Fig. 11a). As the perovskite bandgap increases, there is a bottleneck that prevents the delivery of a greater V_{OC} at the ideal bandgaps for tandem solar cells (1.7–1.9 eV). As seen in Fig. 11b, PCE of wide-bandgap PSCs diminishes with an increasing bandgap. Regarding PSCs with broad bandgap (~1.7–1.9 eV) perovskites based on mixed halide (I–Br), these substantial V_{OC} deficits (~0.5 V) are now the most severe constraints, surpassing even the latest medium-bandap PSCs (<0.3 eV) [135]. A significant obstacle that must be cleared in order to realize the potential of tandem PSCs with high efficiency is the V_{OC} constraint.

Mixed I–Br perovskites normally undergo intrinsic photo-induced phase segregation, which splits them into domains of I-rich and Br-rich, when subjected to light and electrical bias [136–139]. Hoke et al. [120] documented first the formation of photo-induced trap states in $MAPb(I_{1-x}Br_x)_3$ perovskites. The authors noticed that the original photo-luminescent points of the perovskites' I–Br mixture vanished after a brief exposure to light and were replaced by red-shifted peaks. Despite being reversible after dark storage, the phase segregation effect will negatively impact the V_{OC} of volatile organic compounds of wide-bandgap PSCs. This is because the domains of the I-rich will capture charge carriers that are photoexcited, reduced Fermi energy and hence the photo generated voltage in the mixed halide (I–Br) perovskites. Furthermore, it has been suggested that phase separation and halide transition under electrically biased conditions are the cause of the decreased device performance. Research on the processes of photo-induced halide segregation is still ongoing [140–145].

There is an immediate need for solutions to lessen phase separation in hybrid I–Br wide-Eg perovskite solar cells. Several strategies have been tried in an attempt to suppress or inhibit the segregation of halide phases. These strategies include additive engineering (e.g., by adding Cs^+ [146] and Sn^{2+} [147]), passivating grain boundaries with potassium (K^+) addition [148], surface treatment after deposition [149], increasing the grain sizes and crystallinity in perovskite films [124], synthesizing using calibrated nanocrystals in size [150], and alloy formation of 2D/3D perovskites [151–153]. Stoddard et al. showed improved guanidinium (GA) alloying for 1.84 eV phase stability of wide-Eg perovskite films, specifically in the low-dimensional perovskites alloying process [151]. In order to stop halide redistribution, Xiao et al. employed n-butylammonium iodide (BAI) inclusion to build an auto-assembled capping sheet [152]. To get around the V_{OC} plateau problem in wide-bandgap perovskite solar cells, henylethylammonium (PEA) was introduced in trace amounts to $MAPb(I_{0.6}Br_{0.4})$ perovskite by Rajagopal et al. resulting in PCEs of up to 12.2 % and V_{OC} values of 1.30–1.35 V [153]. These illustrations provide potential methods for keeping wide-bandgap mixed I–Br perovskite compounds from experiencing phase segregation. It is obvious that a much larger stoichiometric space has to be thoroughly investigated. Finding more effective and stable PSCs could be sped up with the use of machine learning [154] and autonomous high-volume robotic systems [155] to create and assess the stability of innovative wide-bandgap perovskite configurations.

8. The impact of substrate on the crystallization of perovskite

It is impossible to overstate the impact of substrate on perovskite film quality [156,157]. Systematic studies have revealed that, in comparison to hydrophobic substrates, hydrophilic substrates for perovskite applications typically exhibit higher grain sizes [158]. This is due to the fact that a greater number of tiny droplets, which serve as the first nucleation sites, are present in the hydrophilic substrate with the perovskite precursor sheet as opposed to the hydrophobic substrate. Polar solvents like DMF and IPA are commonly used to dissolve perovskite precursors, therefore it is not surprising that they have a great preference for surfaces that are hydrophilic. Because of inadequate wetting (surface energy mismatch), hydrophobic substrates like a perovskite layer that is not continuous may be produced via PTAA, (poly-TPD), and metal oxides result in the creation of pinholes [159]. This suggests that further adjusting the

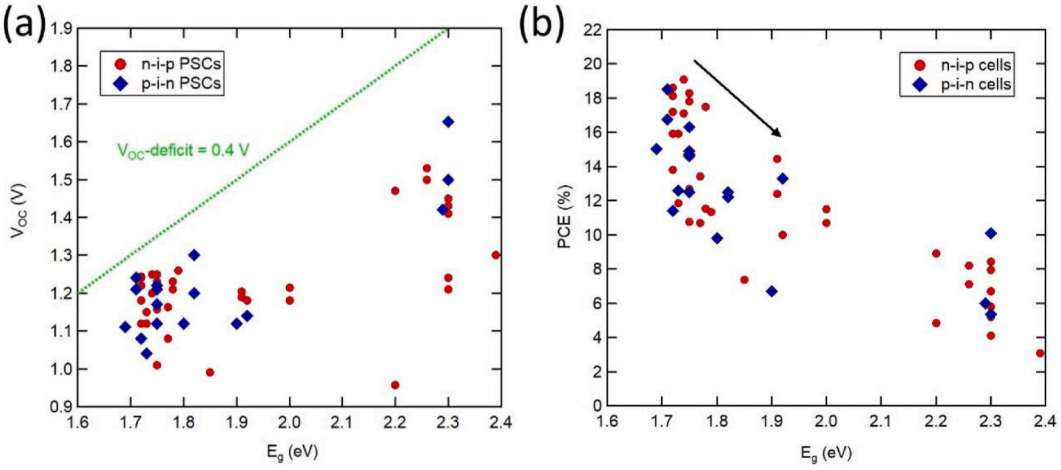

Fig. 11. Curves of (a) V_{OC} and (b) PCE versus bandgap of wide-bandgap PSCs reported in the literature [117].

substrates' hydrophobicity can significantly improve the perovskite thin films' quality for IPSCs. This holds true for IPSCs' metal oxides, such as NiO_X. Regular equivalents of TiO_2 and SnO_2 substrates also require pretreatments to modify the precursor's wettability, such as UV-ozone treatment [160,161].

As evidence of the excellent possibility of PTAA in IPSCs as an HTM, the majority of IPSCs with high certified efficiencies in recent times are based on PTAA HTMs [99,115]. Investigating the film formation on hydrophobic PTAA is important in order to enhance perovskite quality and device performance [135,162]. Similar to PFN, a semiconductor MPS6-TMA conjugated polyelectrolyte was created; it had tertramethylammonium (TMA^+) counterions and a backbone made of an amphiphilic conjugated polymer. The compatibility between the polar perovskite precursors and the hydrophobic PTAA was enhanced by the amphiphilic backbone. TMA^+ ions have the ability to substitute monovalent cations and serve as the perovskite's nucleation sites. These benefits improved the wettability and passivation of interfacial trap states that instantaneously improved all of the PTAA-based IPSCs' performance metrics and led to a PCE of 18.36 % with a 1 cm^2 aperture area [163]. Similar to this, Lee et al. used N,N′-bis(4-butylphenyl)-N,N'bis(phenyl) benzidine, an amphiphilic polymer, which possessed groups that are both hydrophilic and hydrophobic and allowed the formation of a bridge between perovskite and poly-TPD, to enhance the wettability of perovskite precursor on poly-TPD. As a result, the perovskite film's coverage was substantially enhanced [164].

The subsequent crystallization of perovskite layer is influenced by both the wettability and the HTM's crystal lattice. Perovskite has been shown to form orientated crystals when halide of inorganic alkali is incorporated into PEDOT:PSS [165,166]. Additionally, the addition of NaCl further decreased the E_F of PEDOT:PSS from 5.0 eV to 5.2 eV, improving the Ohmic contact at the interface of HTM/perovskite [167]. The device's FF increased as a result, from 75.5 % to 81.9 %. The poor crystallization of perovskite also affected inorganic NiO_X-HTM-based IPSCs. The lattice mismatch discovered by molecular dynamic simulations was the root cause of the interface defects of $NiO_X/MAPbI_3$, which subsequently led to undesired carrier recombination. By partially substituting MA in the perovskite lattice with dimethylamine (DMA), the authors were able to mitigate the interfacial defects. This improved stability of the perovskite's structure and decreased mismatch of lattice, which in turn suppressed the development of defects. The MAXDMA1-XP-bI_3-based optimized IPSCs showed a V_{OC} of 1.116 V, PCE of 21.6 %, FF of 82 % and J_{SC} of 23.5 mA cm^{-2} [58].

Mesoporous structures may cause monovalent cations to be randomly ordered and affect the orientation of perovskite grains, according to IPSC research. Perovskite infiltrating into the structure of the mesoporous configuration would have a shorter diffusion length than perovskite put on flat surfaces. For conventional devices, mesoporous TiO_2 layer exhibits the same phenomena. Additionally, mesoporous scaffold provides significantly more locations for perovskite layer capping nucleation, increasing coverage film while decreasing perovskite granular shape size [159].

9. Charge transport materials (CTM)

The efficient dissociation and conveyance of PSCs' carriers depends on the nature of materials for which the charge transport is made from. The primary goal of ETMs or HTMs is to build an electron or hole-preference contact in order to increase how effectively photogenerated electrons or holes can be extracted. PSCs may effectively separate carriers with appropriate CTMs and perovskite energy band alignment by utilizing the inbuilt electric field at dual surfaces. This can reduce V_{OC} thermal loss and non-radiative recombination. Controlling the parameters of CTMs can lower hysteresis and increase device's long-term stability, provides balanced charge carrier transportation and unwanted buildup of charges will be minimized [168]. Section 10 and 11 explains in detail the two major components of charge transport materials introduced in section 9.

10. Hole transport materials (HTM)

The influence of HTM on the stability and efficiency of inverted PSCs is significant. Typically, HTMs according to [87] have the following characteristics: (i) high optical transmittance to avoid photon energy loss in hybrid thermodynamic modules (ii) appropriate energy level configurations are necessary to reduce interfacial nonradiative recombination; specifically, the valence band maximum (VBM) of perovskite and HTM's HOMO energy level must line up (iii) increased hole mobility, which has a substantial influence on the device performance by lowering the transport resistance of inverted PSCs (iv) compatibility with perovskite precursors, meaning they are not soluble in the perovskite precursors' solvent nor able to interact with their constituent parts and (v) appropriate film-forming qualities that support the creation of thin films of superior quality. There are two broad categories of HTMs found in inverted PSCs: inorganic and organic HTMs. The organic and inorganic hole transport materials are explained in detail in section 10.1 and 10.2 respectively.

10.1. Organic hole transport materials

Polymer HTMs (P-HTMs) are excellent for processing IPSCs with solutions at low temperatures and are simple to construct. Additionally, P-HTMs can withstand polar solvents better than small-molecule HTMs because of their larger molecular weight. Therefore, as reported in Refs. [169–171], P-HTMs have undergone substantial study in terms of their molecular structures, namely their lowest occupied and highest occupied molecular orbitals (LUMO and HOMO, respectively).

In IPSCs, a p-type conductive polymer popularly known as PEDOT:PSS, is a frequently utilized HTM because of its many benefits, including its low temperature solution processing and superior light transmission. However, the solar device's stability is significantly hampered by the acidic PEDOT:PSS, and the low LUMO of this material reduces its effectiveness as an electron blocker. More significantly, there was considerable non-radiative recombination due to energy mismatch between perovskite and PEDOT:PSS. Early

research indicated that the PSS content had a significant impact on the PEDOT:PSS's Fermi level (E_F) [172,173]. In order to improve the HTM/perovskite's energy level alignment, PEDOT:PSS was mixed with sodium polystyrene sulfonate (PSS–Na) as a filler to partly substitute PSS. This caused the modified PEDOT:PSS' HOMO to shift to 5.2 eV from 4.9 eV [174]. The modified device with 15.56 % PCE as a result produced an increased V_{OC} to 1.11 V from 0.96 V. To enhance the effectiveness of inverted devices, F4TCNQ-doped PEDOT:PSS was added [175]. The HTM/perovskite interface's thermodynamic potential loss was further reduced by F4TCNQ doping, which raised the PEDOT:PSS's E_F to 5.18 eV from 5.08 eV. Additionally, the F4TCNQ molecule's N atom's single pair of electrons was able to successfully passivate the dangling bonds of the unsaturated Pb ion, raising the PCE to 17.22 % from 13.30 %. Remarkably, polar perovskite precursor solvents are soluble in tiny molecular dopants like F4TCNQ. The above problem was avoided by copolymerizing dopamine with a greater ability to donate electrons on PEDOT:PSS. By respectively boosting the device's V_{OC} and FF to 1.08 V and 77.5 % with a PCE of 18.5 %, considerably changed the E_F of HTM to 5.33 eV from 5.1 eV [176].

In as much as additives can significantly enhance the PEDOT:PSS's electrical characteristics, the long-term durability of devices is adversely affected by the severely corroded device brought on by moisture absorption and extreme acidity. Due to HTMs' corrosiveness, PEDOT:PSS and alkaline imidazole were mixed to increase the device's stability [177]. The PEDOT:PSS phase separation as the perovskite nucleus was further induced by the imidazole molecule's encapsulation. Contrary to strong bases like KOH and NaOH [178], the weak imidazole further increased the transmittance of HTMs while having no impact on the conductivity of HTMs. After aging for two weeks in 20 % relative humidity, the PEDOT:PSS-based inverted devices were able to raise V_{OC} by 180 mV and maintain 95 % of their initial efficiency. Due to its superior electrical characteristics and chemical neutrality, PTAA has grown to be the most often utilized P-HTM in inverted devices. Hydrophobic PTAA has the band energy structure that is suitable with the extremely effective

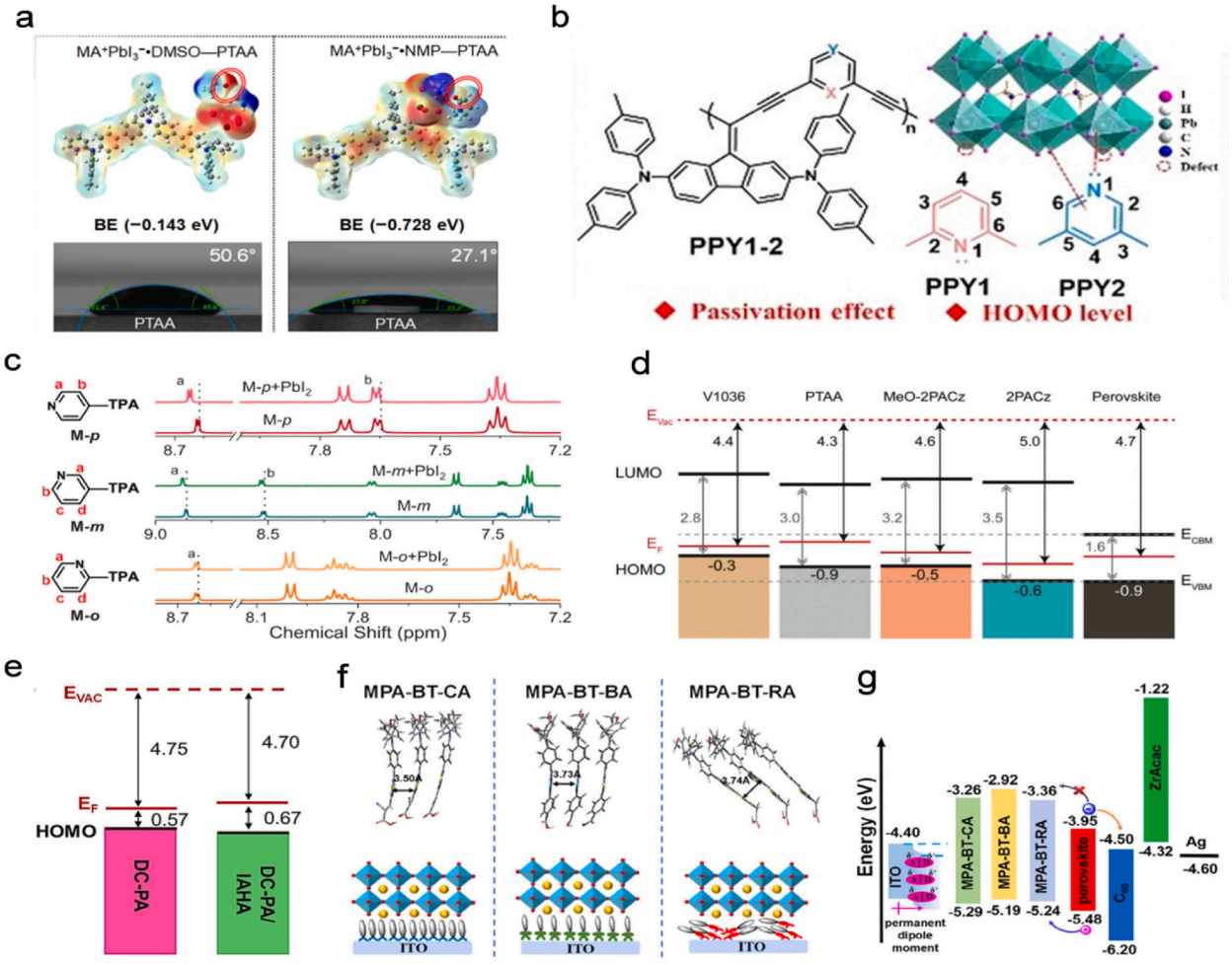

Fig. 12. Typical organic HTMs for inverted PSCs. (a) Schematic representation of the binding energy and electrostatic potential of MA^+PbI^{3-}•DMF-PTAA and MA^+PbI^{3-}•DMSO-PTAA and contacts angle readings for matching solvent precursor solutions on a PTAA surface, (b) Ideas for molecular designs of PPYs, (c) Pyridine-based monomer 1H NMR pattern, either mixed with or without PbI_2 added, (d) Diagram illustrating the energy alignment of the studied HTMs with perovskite, (e) Diagrammatic representation of DC-PA and DC-PA/IAHA energy level alignment, (f) Diagram showing the best stacking configuration and potential behavior of molecular architecture for three SAMs on an ITO substrate, (g) Diagrammatic representation of the inverted devices' energy levels using three self-assembled monolayers (SAMs) [87].

mixed-cation perovskite and can considerably enhance the grain size of perovskite. The loss of the HTM/perovskite interface's thermodynamic potential energy is anticipated to be further reduced via PTAA's energy band engineering [179]. In order to enhance the electrical characteristics of PTAA, the inorganic Copper (I) thiocyanate (CuSCN) has been employed as an additive [180].

The hydrophobic nature of PTAA's surface makes it challenging to produce compact, and continuous perovskite films [125]. Pre-wetting with DMF/DMSO solvents is another helpful technique for resolving issues brought on by the PTAA surface's non-wettability [36]. However, due to the fact that most DMF/DMSO solvents swiftly disappear during the speedy process of spin-coating, leaving PTAA with only an irregular thin DMF/DMSO layer, the benefit of this approach on enhancing wettability is not immediately apparent [181]. To do this, Wolf et al. improved perovskite precursor inks' wettability on PTAA by substituting NMP for DMSO in a DMF/NMP co-solvent solution [181]. The contact angle dropped significantly (27.1° against 50.6°) and the addition of $MAPbI_3$-NMP with PTAA had a greater binding energy (−0.728 eV) compared to $MAPbI_3$-DMSO (−0.174 eV). The ink of perovskite precursor enhanced wettability on PTAA may prevent the development of Nano-scale and micro pinholes, allowing for the creation of homogeneous, and over sizable compact films' surfaces. As a result, the inverted devices based on DMF/NMP ink achieved significant PCEs of 21.5 % (0.1 cm^2) and 19.8 % (6.8 cm^2) in turn as presented in Fig. 12a. Furthermore, adding an interlayer is a useful technique for raising PTAA's wettability [182,183]. For example, Gong et al. used ozone-treated PMMA-coated PTAA to introduce HGGBL on dry PTAA for perovskite production. This raised the perovskite precursor solution's affinity for PTAA and decreased its surface potential [183]. Moreover, the C═O bond served as a Lewis base site to securely attach PTAA to the crystals of perovskites. These enhancements increased IPSC's PCE to 20.75 % from 17.42 %.

Other specialty polymer-HTMs are employed to build PSCs in addition to regular polymer HTMs [184]. Zhu et al. established a new polymer HTM based on pyridine (PPY2) that is HTM-free [185] as it aligned more closely with perovskites' energy level and enhanced hole mobility. Moreover, pyridine successfully passivates iodide and awkward Pb^{2+} defects (Fig. 12b). These advantages led to the favorable PCE of up to 22.41 % and a high V_{OC} of 1.16 V for inverted PSCs with PPY2 as the HTM. Wu and colleagues introduced PTAA-based polymer HTMs that were produced using molecular engineering. These polymers were made by substituting multi-functional pyridine units for alkyl groups [186]. The proton-a signal's clear downfield shift to 8.62 from 8.58 ppm for M-*p* measurements in 1H NMR indicated that the coordination of N–Pb was strongly associated with pyridine-nitrogen's single-electron pair exposure (Fig. 12c), which was advantageous for successfully passivating the states of the interfacial trap. Finally, a very high PCE of more than 22 % (0.105 cm^2) and a similar PCE of more than 20 % (1 cm^2) were obtained with the ideal p-PY HTM.

The use and commercialization of PSCs are limited by the high cost of production and polymer hydrophobicity, which hinders the perovskite's wet chemical deposition in as much as inverted PSCs made from polymer HTMs have attained excellent PCEs [187,188].

Conversely, tiny molecule HTMs have become popular because of their distinct molecular mass, structure, and photophysical characteristics [189]. Because of their low cost, straightforward synthesis and comparatively simple modification, self-assembled monolayers (SAMs) in particular offer options for constructing HTMs for inverted PSCs that are inexpensive, scalable and stable, showing their excellent prospects for employment in tandem solar cells and inverted PSCs [23,190,191]. For instance, Getautis et al. created V1036 as the SAM-HTM of inverted PSCs by merely submerging the substrate in a mixture of V1036 and butylphosphonic acid, which attaches to the phosphonic acid anchoring group on the ITO's surface. This allowed them to achieve a PCE of 17.8 % and an average FF of nearly 80 % [192]. A fresh generation of SAMs was designed in their follow-up investigation in which [2-(3,6-dimethoxy-9Hcarbazol-9-yl) ethyl] phosphonic acid (MeO-2PACz) and [2-(9H-carbazol-9-yl)ethyl] phosphonic acid (2PACz) were used [193]. These SAM-based molecules aligned their energy levels more closely to the perovskite VBM (Fig. 12d) than V1036. This drastically enhanced interfacial carrier transport and considerably decreased defects at interface. Additionally, because carbazole and perovskite are chemically compatible, an excellent passivation interface was produced, which suppressed nonradiative recombination. Consequently, self-assembled monolayers (SAMs)-based inverted PSCs had a good PCE of more than 21 % and a maximum V_{OC} of 1.19 V. Then, building on earlier studies, they created a new kind of SAM, [4- (3,6-dimethyl-9H-carbazol-9-yl)butyl] phosphonic acid (Me-4PACz), and produced a tandem solar cells made of silicon and perovskites with a verified PCE of more than 29 % [194]. Phosphonic acid (DC-PA) was synthesized recently by Jen et al. using ((2,7-dimethoxy-9H-carbazol-9-yl) methyl), a novel SAM based on MeO-2PACz having favorable dipole values and matched energy levels [195]. To create co-SAM, IAHA, the DC-PA solution was supplemented with an alkyl ammonium salt. −5.37 eV was the HOMO energy level of the co-SAM (Fig. 12e), reducing the energy offset since it closely matches the energy levels of the perovskite. The co-SAM-based perovskite film's extended photoluminescence lifetime implied inhibited interfacial nonradiative recombination. These benefits led to the realization of an improved inverted PSC with enhanced device stability and an outstanding PCE of 23.59 %.

As HTMs for inverted PSCs, several donor-acceptor (D-A)-type SAMs, such as MPA-BT-CA, MPA-BT-BA, and MPA-BT-RA, were synthesized by Guo et al. [196]. MPA-BTCA retained closer intermolecular stacking (3.50 Å) than the other two SAMs, allowing for the production of improved perovskite films on the substrates of ITO/MPA-BT-CA. This was helpful for the self-assembly process to generate a denser and smoother monolayer coating (Fig. 12f). Furthermore, as seen in Fig. 12g, more closely aligned energy levels of the perovskites are the HOMO energy levels of MPABT-CA, improving charge extraction and the interior electrical field. As a result, the IPSCs using MPA-BT-CA obtained an astounding PCE of 21.81 % and a noteworthy FF of 82 %.

Small organic compounds have also been employed as superior HTMs in place of SAMs [188,197,198]. However, SAM-HTMs are more widely utilized among small-organic-molecule HTMs, hence SAMs provide level of interfacial energy tailoring and inhibition of interface recombination, which significantly increases device stability and efficiency. Specifically, SAMs are used as the most efficient HTMs for inverted PSCs and silicon tandem or perovskite devices [25,194]. PTAA is frequently utilized in high-efficiency inverted PSCs for mainstream polymer HTMs [21,24,199]. Its expensive price and nonwettable surface, however, severely restrict its commercial use. Small organic compounds with similar properties are easy to synthesize and inexpensive when compared to PTAA. Furthermore, SAMs perform exceptionally well in tandem solar cells, which could be the primary upcoming improvement path for perovskite

photovoltaics. Therefore, SAMs must be improved further in order to make inverted PSCs as efficient as conventional PSCs [41]. To put it briefly, the rapid advancement of organic HTMs has significantly increased the stability and effectiveness of IPSCs.

10.2. Inorganic hole transport materials

Considering numerous benefits such as long-term stability, inorganic HTMs have received a lot of attention. Examples include p-type semiconductors based on NiO_X and compounds based on copper such as CuI, CuSCN, CuO_X, $CuAlO_2$, $CuCrO_2$, and $CuCaO_2$ as well as oxides of metals like CoO_X, WO_X, MoS_2, Co_2N, and VO_X [113,200–202].

Inverted PSCs with organic HTMs also encounter difficulties because of their hydrophobicity, high raw material costs, and probable

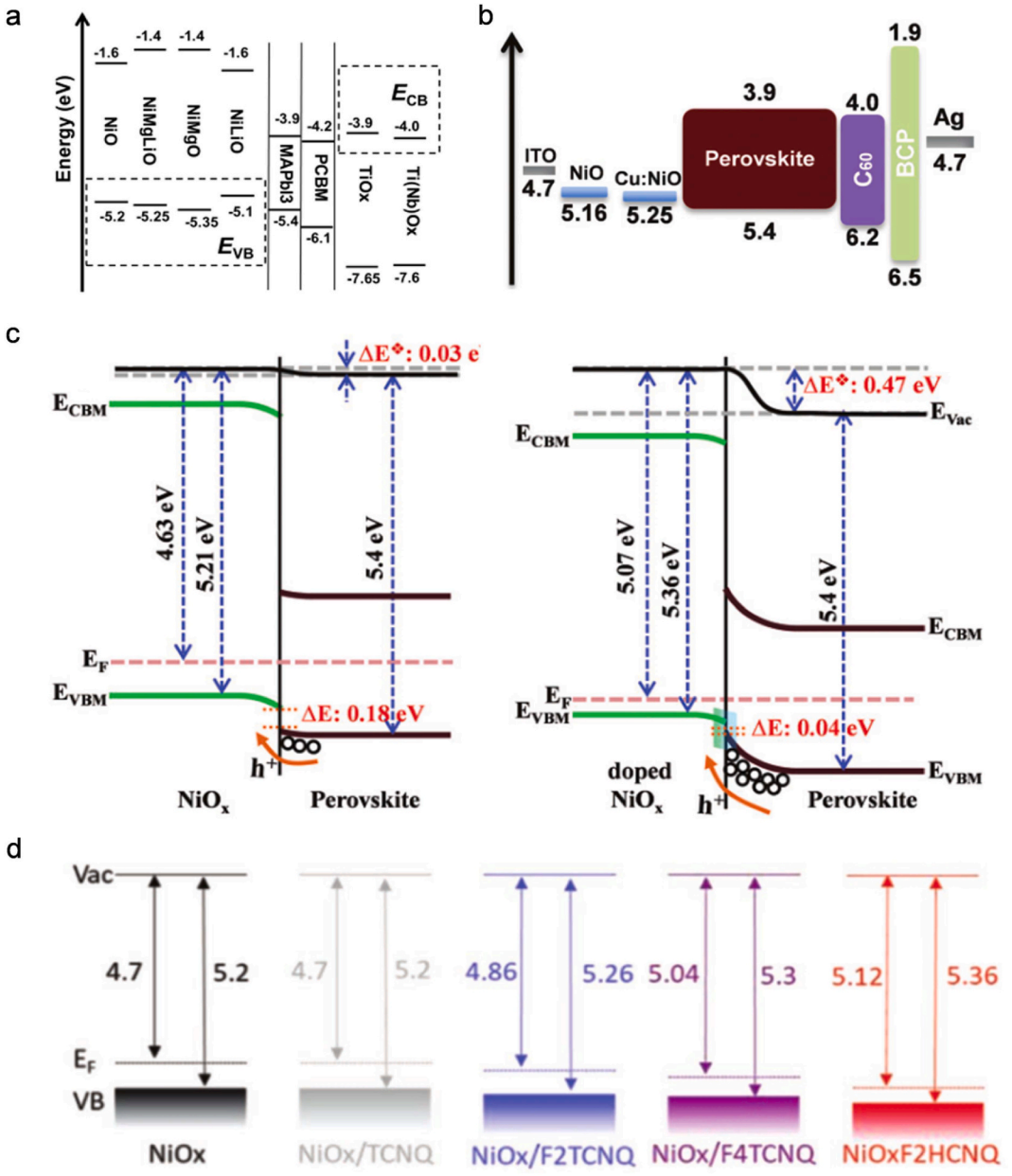

Fig. 13. Important advancements in the understanding of inverted PSC efficiency centered on enhancing the characteristics of NiOx. (a) Diagram showing the predicted CTMs's band edge positions under investigation in relation to PCBM and $MAPbI_3$, (b) Diagrammatic representation of the energy levels of an inverted Cu:NiOx device, (c) Diagrammatic representation of how the molecular doping of F6TCNNQ affects the band bending at the interface between a p-type doped NiOx and a perovskite, (d) NiOx film energy level diagrams with and without TCNQ, F2TCNQ, F4TCNQ, and F2HCNQ [87].

degradation, which restricts the use and commercialization of inverted PSCs. In contrast, due to their outstanding thermal and long-term stability, inorganic HTMs have received a lot of interest [203–205]. In inverted PSCs, metal oxides based on nickel oxide (NiOx) are the most efficient among inorganic HTMs, and they have been extensively studied because of their good stability, easy synthesis, deposition, and alignment of the favorable energy level with the majority of perovskite absorbers [206]. Since stoichiometric NiO is typically insulating, inherent nickel vacancies, or nickel^{3+} self-doping, play a significant part in the conductivity of NiOx. As a result, devices' series resistance rises and necessitates careful thickness adjustment. Nevertheless, the undoped NiOx hole charge density is low due to the high ionization energy of Ni vacancies is significantly impacted, leading to relatively low conductivity. To do this, NiOx was doped with various molecules and metal cations such as Ag^+, Au^+, Cu^{2+}, Cs^+, and K^+, to increase conductivity and modify the concentration of Ni vacancies to alter the energy level [207–211]. A strongly p-doped (p+) Ni_XMgyLi_{1-X}-yO codoping technique was developed by Han et al. to compensate the undesirable positive shift in its VBM caused by doping Li^+ into the NiOx lattice. Specifically, 15 mol% Mg^{2+} was doped in 5 mol% Li^+-doped NiOx (Fig. 13a) [212]. In light of this, the conductivity of the $Li_{0.05}Mg_{0.15}Ni_{0.8}O$ film was 2.32×10^{-3} S cm^{-1}, which in comparison to the undoped sample, was almost 12 times greater. This indicates a significant rise in the shunt resistance and a drop in the series resistance, both of which are beneficial for creating large-area PSCs (>1 cm^2). This led to the creation of a PSC with a large area (>1 cm^2) and a high certified PCE of 15 %, setting a record for large-area (>1 cm^2) PSC

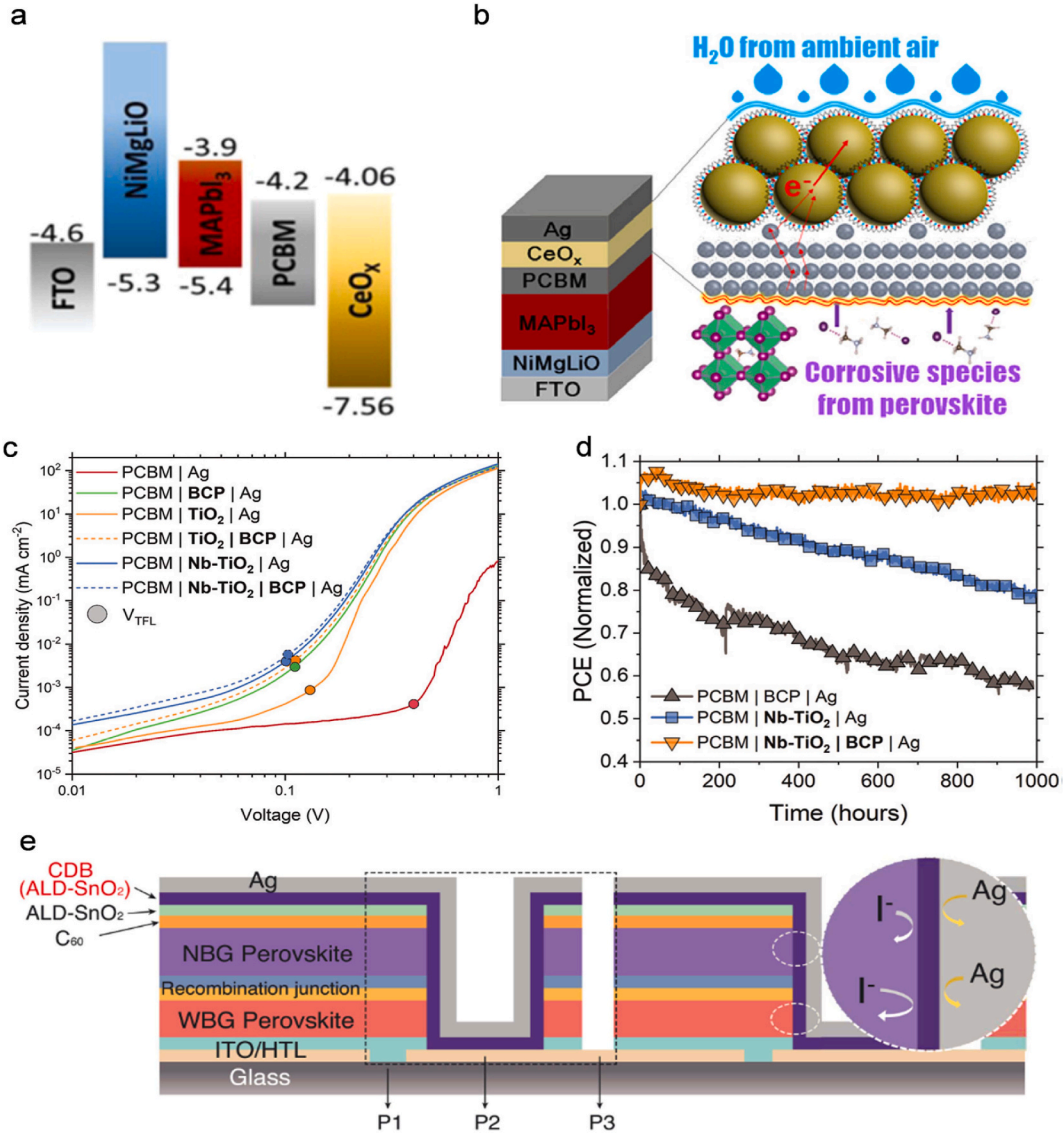

Fig. 14. Methods for adjusting ETMs. (a) Diagram showing the different components' energy levels in the associated inverted PSCs, (b) Diagram showing how CeOx enhances device stability, (c) Electron-only device typical dark J-V curves with various PCBM/Ag contact interfacial layers, (d) Best perovskite devices' operational stability interfacial bilayers both with and without, (e) Diagram showing how tandem-based perovskite module with CDB is configured in series [87].

efficiency at the time. He et al. later created room temperature (RT) copper-doped NiOx (Cu:NiO) nanoparticle inks without additional processing [209].

Cu:NiO film showed both Cu^{+} and Cu^{2+} states. Cu^{+} was substituted for Ni^{2+}, which increased hole mobility and improved the NiOx layer's conductivity. Furthermore, a favorable negative shift in the Cu:NiO film's VBM was observed (Fig. 13b), which enhanced interfacial charge extraction and transfer. Therefore, for the equivalent inverted PSCs, a PCE of up to 20.15 % was obtained. In a similar vein, He and associates suggested a molecule-doped NiOx consisting of F6TCNNQ, a low LUMO (−5.37 eV) strong electron acceptor [213]. Significantly improving hole extraction and lowering interfacial nonradiative recombination, the doped NiOx's E_F grew to −5.07 eV from −4.63 eV, while the offset energy level between the perovskite absorber and NiOx's VBM decreased from 0.18 to 0.04 eV (Fig. 13c). Consequently, the optimal PCE of inverted PSCs utilizing NiOx reached a maximum of 20.86 %. Motivated by this approach, Chen et al. methodically examined the impact of doping many compounds with high electron affinity comparable to that of F6TCNNQ, such as 2,5-difluoro-TCNQ (F2TCNQ), F4TCNQ, TCNQ, and F2HCNQ, into NiOx [214]. The greatest electron affinity (EA) was shown by F2HCNQ, which improved the transfer of charges from the NiOx VBM to the molecules of LUMO. At the NiOx/perovskite interfaces, the higher WF and VB brought about by the elevated EA led to more appropriate energy level alignment (Fig. 13d), which made interfacial hole extraction faster and less energy-intensive. As a result, the efficiency of inverted PSCs based on F2HCNQ-NiOx produced at low-temperature surpassed 22 % for the first time.

Despite their excellent performance, inverted PSCs based on NiOx nevertheless have record lower PCEs than those of PSCs based on SAM or PTAA because of significant energy offset at the junction between perovskite and NiOx [206], caused by (i) large surface imperfections and mismatch in energy levels, which makes interfacial carrier recombination much worse and hinders charge carrier extraction (ii) PbI_2-xBrx, which is formed at the NiOx/perovskite interface [215] due to high-oxidative-state Ni^{3+} reacting with A-site cation salts, can result in A-site defects and PbI_2-xBrx-rich perovskite, creating noncapacitive hysteresis and a hole extraction barrier; and (iii) the creation of shallow-level defects and significant ion movement are caused by light-induced deprotonation at the NiOx/perovskite interface, which also results in interfacial voids and vacancies, resulting in lower efficiency [216,217]. Excellent results have been generated by NiOx-based IPSCs as the most promising inorganic HTM, with a certified PCE of 23.91 % [23].

11. Electron transport materials (ETM)

To attain high efficiency IPSCs, electron-transfer materials (ETMs) are one of the prerequisite requirements. Well-known ETMs are fullerenes and their derivatives (PCBM and C_{60}) which have been widely used in inverted PSCs due to their high electron mobility and low processing temperature [23–25]. Because inorganic alternatives to double-layer ETMs have better inherent stability and can increase PCE and stability at a cheaper cost, investigation of ETMs has therefore primarily fixated on identifying these alternatives to raise the inverted PSCs' stability and effectiveness [218,219]. Accordingly, inexpensive cerium oxide (CeOx) nanocrystals were used by Chen et al. as an inorganic ETM [220], showing encouragingly improved electron mobility (103 $cm^2\ kV^{-1}\ s^{-1}$) and appropriate energy match for effective extraction of charges (Fig. 14a). Therefore, IPSCs with the NiMgLiO/$MAPbI_3$/PCBM/CeOx combination had improved PCE of 18.7 %. Because of the unique impact of PCBM/CeOx bilayer ETL's chemical shielding, the resultant PSCs also demonstrated exceptional stability, holding up to 91 % of their original PCEs during continuous light immersion in air with regulated humidity (about 30 %). By doing this, it may be possible to prevent both ambient moisture and corrosion of Ag electrode by perovskites (Fig. 14b). The resistive reaction of the analogous device with PCBM-Nb-TiO_2-batocuproine (BCP)–Ag structure was much improved by Troughton et al. using PCBM/Nb-doped TiO_2 as a multilayer ETM, as evidenced by the significantly lower VTFL (Fig. 14c) [221], thus raising the reference ETM's electron mobility. As a result of atmospheric nitrogen with constant light immersion, the PCE of inverted PSCs grew to 20.7 % from 18.7 % with 83 % FF without deterioration for a minimum of 1000 h (Fig. 14d). The effectiveness of the most efficient inverted PSCs based on selective electron connections only (inorganic ETMs) or fullerene/inorganic ETMs, nevertheless falls short of PSCs based on organic ETMs, despite their remarkable achievements.

Furthermore, the growing popularity of perovskite tandem devices has brought increased attention to atomic-layer-deposited SnO_2 (ALD-SnO_2) [,194,222,223]. In this sense, SnO_2 is typically placed as a buffer layer on the ETM. For instance, in perovskite/silicon tandem systems, SnO_2 is frequently employed as a buffer layer to lessen the damage that sputtering ITO causes to the perovskite [194]. ALD-SnO_2 is typically utilized in perovskite tandem solar cells to shield the front cells from PEDOT:PSS's corrosion [222]. For inverted tandem modules (Fig. 14e), Tan et al. recently developed a thin ALD-SnO_2 conformal diffusion barrier (CDB) [223], which was deposited following P_2 scribing. In this case, halide-metal inter-diffusion was overcomed by the electrically conductive CDB, which also served as a lateral diffusion barrier between connecting sub-cells, preventing an interaction between the metal electrodes and perovskites. These advantages allowed the achieved 21.7 % certified PCE with all-perovskite tandem solar modules with an aperture area of 20.25 cm^2. Additionally, these cells proved exceptional stability, maintaining 75 % initial PCE even after 500 h of nonstop use under artificial one-sun lighting.

In general, PCBM or C_{60} ETMs are still utilized in high-performing inverted PSCs. To increase IPSCs' stability, inorganic layers based on fullerene/inorganic metal oxide can be used as double-layer ETMs. However, the commercialization of fullerene derivatives (PCBM and C_{60}) is limited due to their high costs. Thus, extra investigation is required to produce superior ETMs in order to improve the inverted PSCs' stability and efficiency.

Comparatively, inorganic ETMs are more chemically stable than organic ETMs. However, it is difficult to achieve extreme performance in terms of efficiency for IPSC devices made of inorganic ETMs due to the lower conductivity and band-alignment. Therefore, in order to attain both continuing stability and great efficiency of inverted devices, researchers have employed Fullerene-based inorganic metal oxide multilayer ETMs [224]. For instance, in a device with the following structural components: FTO/-NiO_X/$MAPbI_3$/C_{60}/SnO_2 nanoparticles/Ag, nanoparticles of SnO_2 generated by hydrothermal technique were mixed with C_{60} and Ag

[225]. The inverted device significantly improved moisture stability while maintaining efficiency because of the SnO_2's suitable energy band and high crystal structure. After being stored for 30 days in air under 70–80 % relative humidity, the devices upheld over 80 % of their early PCE of 18.8 %. A denser SnO_X layer (ALD-SnO_X) was then created using atomic layer deposition technology (ALD) [226]. It prevents the deterioration of perovskite and iodide ion corrosion on BEMs by blocking the transport of internal and external moisture and breakdown components. This increases thermal and moisture stability for longer periods more than 1000 and 350 h respectively. The moisture stability of inverted devices was achieved and maintained at 86.7 % PCE for 500 h, 85 °C. The HTM and ETM were made from the aluminum-doped zinc oxide (AZO) and NiO_X generated by ALD, respectively [227].

12. Back electrode materials

Back electrode materials (BEMs) are also known as rear electrode materials (REMs). The characteristics of BEMs have a big impact

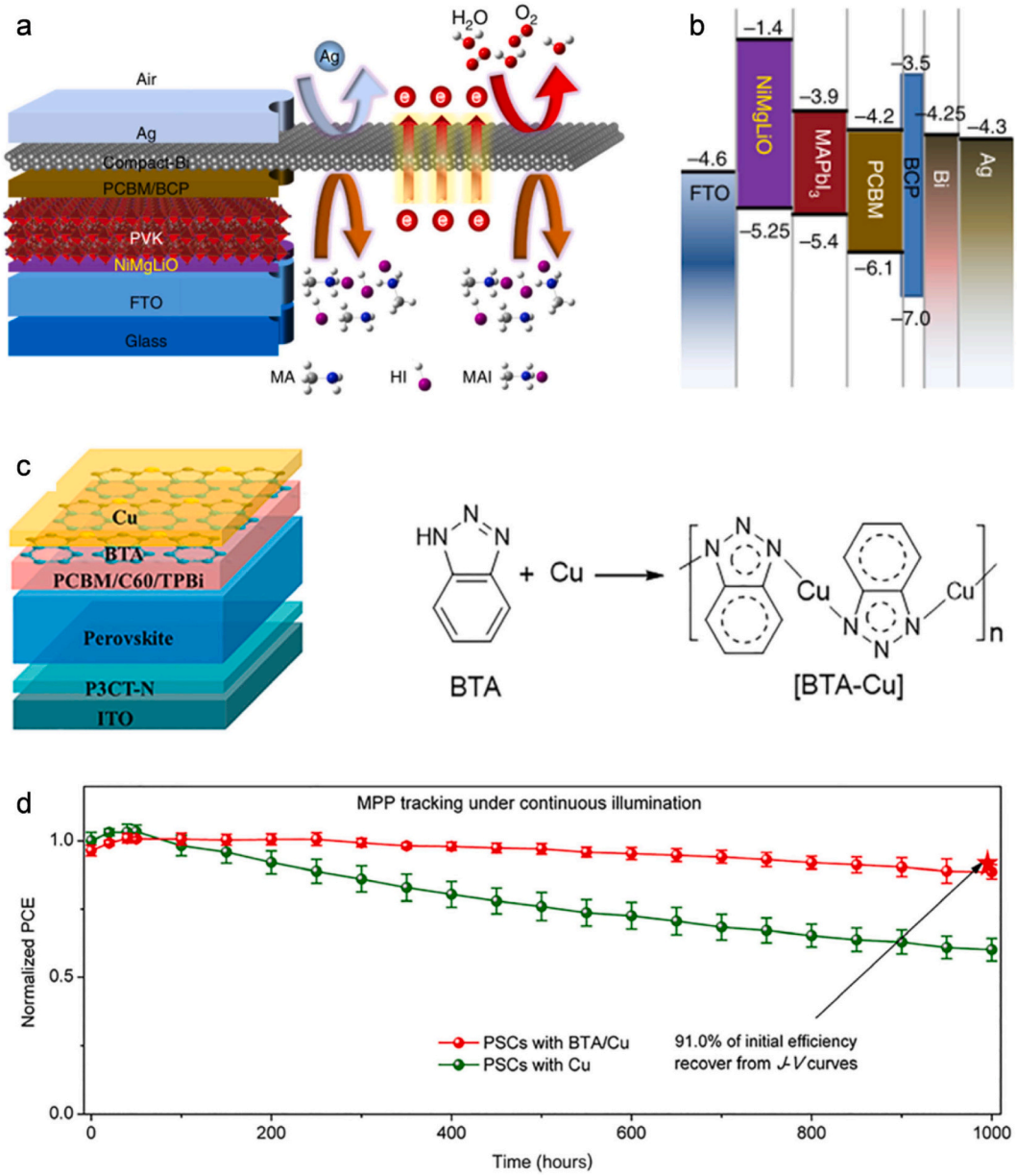

Fig. 15. Stoppage metal counter electrodes from corroding. (a) The bismuth electrode's schematic diagram and device layout prevent both external and internal infiltration, (b) The corresponding device energy level diagram, (c) The device structure and schematic design depict BTA molecules producing polymeric layer [BTA-Cu] that is insoluble through chemical coordination with a Cu electrode, (d) Long-term MPPT under constant illumination of devices with and without BTA [87].

on how well perovskite devices work. The two primary purpose of BEMs is to deliver power to the external circuit and also serve as back reflectors, which reflect incident light. The effectiveness and the processing conditions for preparation, conductivity, stability, and work function of BEMs have a substantial impact on the IPSCs's long-term stability. For instance, the stability of the overall device is meaningfully affected by the breakdown of BEMs brought on by ion movement and external elements like oxygen and moisture. Additionally, a Schottky barrier that prevents carrier transport may be formed at the interface because of the Fermi level (E_F) difference between ETM and BEM.

Additionally, the hydrophobic BCP can stop ion diffusion-related corrosive issues [228] and erosion by outside moisture [229], enhancing the stability of the associated devices. Regretfully, there is general agreement that with aging, the metal electrodes (Cu, Ag, and Al) frequently utilized in IPSCs experience decomposition reactions with the breakdown of perovskites [228–230]. Moreover, active metal counter electrode corrosion is brought on by ion migration due to degradation elements (moisture, heat, and light), which significantly reduces PSC stability and efficiency. Furthermore, there is a significant build-up of interface charges and an impact on charge transfer and collection due to the disparity in E_F between ETMs and BEMs.

For this reason, Chen et al. created inverted PSCs with the following structures: perovskite, BCP, Bi, Ag, and fluorine-doped tin

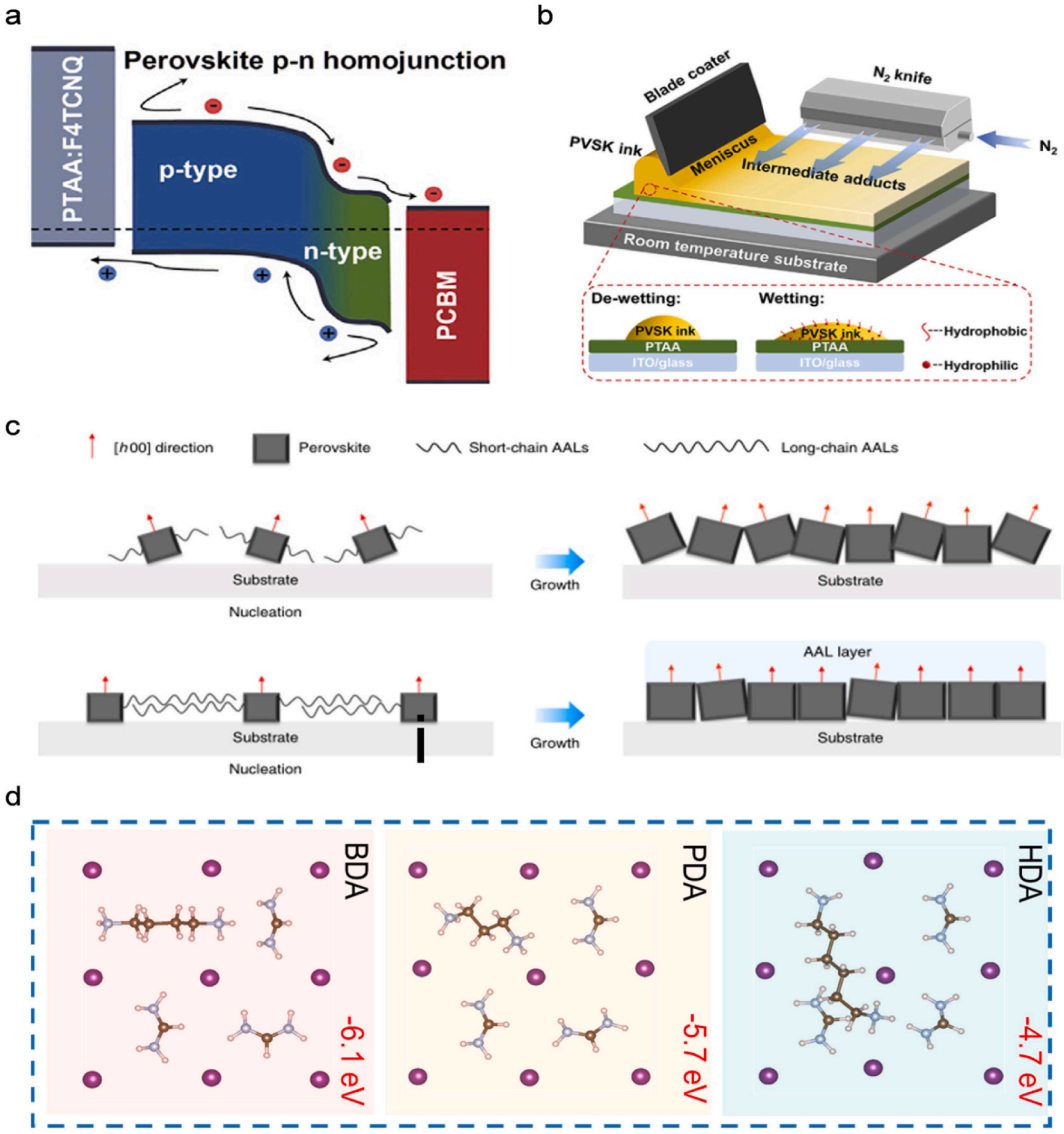

Fig. 16. Improved photovoltaic performance of inverted PSCs using additive engineering. (a) Diagram demonstrating the energy level bending of a capsaicin-containing perovskite in relation to CTMs, (b) Diagrammatic representation of TAH enhancing perovskite ink's adherence to the hydrophobic PTAA below during room temperature meniscus coating, (c) Diagrammatic representation of how long and short-chain AALs affect crystallization during the formation of perovskites, (d) Three alkyldiammonium ligands (HDA, PDA, and BDA) are theoretically modeled as adhering to VFA on the perovskite surface [87].

oxide (FTO/NiMgLiO/PCBM) and added an interlayer of chemically inert bismuth (Bi) [230]. In their systems, Bi acted as a stalling layer to prevent iodine erosion of the Ag electrode and efficiently safeguard the perovskite from unwanted exterior dampness incursion (Fig. 15a). Additionally, the Bi interlayer with the ideal thickness showed good conductivity and an energy level that matched, which had no impact on the electrons' movement or accumulation in the associated devices (Fig. 15b). Consequently, these Bi-interlayer-based devices remained 88 % efficient in ambient air without encapsulation for over 6000 h in the dark, and after 500 h of thermal aging in a nitrogen environment at 85 °C, their initial efficiency decreased by only 5 %. Furthermore, Fang and colleagues suggested a chemical anti-corrosion method that involves the insertion of an organic benzotriazole (BTA) preservative prior to the deposition of Cu electrodes [231]. Instead of acting as a physical barrier layer as Bi indicated earlier, the BTA layer in this technique interacted chemically with the Cu electrode to produce a polymeric, insoluble layer of [BTA-Cu] (Fig. 15c). The interlayer of BTA served as a diffusion barrier and efficiently prevent diffusion of Cu or I into PSCs film at 85 °C in a glove box and confirmed effective when compared to the reference. Gaining from the aforementioned benefits, the stability of the device was much enhanced. PSCs with BTA aged for 1100 h at 85 °C while maintaining approximately 90 % of their initial efficiency. Furthermore, PSCs with BTA demonstrated exceptional operating stability, retaining under MPPT for 1000 h 91 % of their initial efficiency (Fig. 15d).

Therefore, strong interfacial barriers thereby prevent both the migration of metallic ions in the direction of the absorber layer and the corrosion of metal electrodes due to the movement of ions, which is required to achieve high efficiency and stable IPSCs.

For this reason, customizing the top electrode is just as important as choosing the right metal electrode in order to produce reliable devices. As barriers positioned between metal electrodes and CTMs, a variety of inorganic and organic materials have been used thus far. These materials include poly(methyl methacrylate) (PMMA) [232], amine-mediated metal oxide (AM-TiOx) [233], metal acetylacetonate (ZrAcac) [234], and naphthalene diimide derivative (NDI-BN) [235]. Additionally, for semitransparent or tandem solar cells, transparent electrodes with high optical transmittance such as silver nanowires (AgNWs) [227], indium zinc oxide (IZO) [236], and ITO [237] are often employed. Although the TCO counter electrode is usually sputter-deposited, a buffer layer (MoOx, etc.) is usually needed to shield the perovskite or HTM/ETM layer from damage. Several inorganic ETL barriers have also been deposited on top of PCBM/BCP ETLs/buffer layers to improve the perovskite layer's protection against damage [238–240]. Generally, in order to generate effective and stable inverted PSCs, further work is needed to establish an appropriate counter electrode technique.

13. Strategies for preparation of high quality perovskite solar cells

With the significant advancements in charge transport and perovskite crystallization management, radiation-free recombination, which was first caused by defects and an imbalance in the interface energy level is now one of the key problems that restricts device performance. The non-radiative recombination will significantly reduce device V_{OC} and FF and result in severe thermal potential loss [99,225,241]. Numerous techniques for lowering defects, inhibiting nonradiative recombination, and improving device stability and efficiency have recently been developed by researchers. Among these, interface engineering and additive engineering techniques for perovskites have garnered a lot of interest and are particularly well-liked for highly effective inverted PSCs. This section gives a summary of the most recent developments in additive and interface engineering for highly efficient inverted PSCs.

13.1. Additive engineering

In order to improve the devices' stability, decrease defects, and enhance the excellence of the perovskite films, additives are mostly added to the perovskite layers during fabrication process [242,243]. During defect passivation, Bao et al. fully converted a $MAPbI_3$ surface area from p-type to n-type using the natural additive capsaicin [244]. When the E_F of the VBM moved positively to 1.03 eV from 0.55 eV, the surface of the perovskite experienced absolute transition from p-type to n-type. Reducing interfacial carrier recombination, this energy transition increased interfacial charge transfer between the PCBM and perovskite (Fig. 16a). Thus, with the equivalent inverted PSCs, good stability, a remarkable FF of 83.81 %, and an exceptional efficiency of 21.88 % were realized. The multifunctional TAH was added to $MAPbI_3$ almost simultaneously to create a large-scale coating [245]. This coating enhanced the perovskite ink's adherence to the hydrophobic PTAA layer underneath and precisely adjusted the perovskite crystallization kinetics (Fig. 16b). These benefits allowed for the development of a smoother, denser, and more crystallinity of perovskite coating on the PTAA substrate. Furthermore, charged defects at the perovskite surface and grain borders may be passivated by the hydrophobic surface that is formed on the upper surface of the perovskite by the functionalized zwitterionic groups of TAH. As a result, blade coating raised the TAH-based inverted PSCs' efficiency, which increased from 19.34 % to 22.07 % with an active area of 0.04 cm^2. Additionally, the resultant PSC demonstrated exceptional moisture stability, retaining 96.7% of its original PCE in room temperature at 25 ± 5° Celsius and 20 ± 5% relative humidity (RH) for 1200 h.

Additionally, a lot of work has been done using organic ammonium (-$NH3^+$) cations as passivating layers to raise the stability and efficiency of IPSCs [23]. As an illustration, Sargent et al. added numerous Alkylammonium ligands (AALs) that anchor to the surface with varying chain lengths to perovskite precursors in order to act as passivating agents [21]. After AALs were fixed to the perovskite matrix through van der Waals interactions between the alkyl ligands' organic moieties, alkyl ligands arranged closely together formed up the perovskite surface. The alkyl chain's length strengthened these interactions (Fig. 16c). Since the holes between the perovskite and C_{60} interfaces might be efficiently blocked by the long-chain AAL layer, it was able to regulate the crystal growth direction and reduce nonradiative recombination, which in turn raised the perovskite films' crystallinity. The resultant PSCs with AALs (OAm) demonstrated good stability under MPPT and simulated AM1.5 G illumination after 1000 h with no efficiency degradation. They also attained a high PCE of 23.0 %, J_{SC} of 24.1 mA cm^{-2}, V_{OC} of 1.17 V, FF of 81.6 % with a verified stable PCE of 22.3 %. Combining the perovskite precursor with large organic cations, such as guanidinium (GUA), n-butylammonium (BA), ethylammonium (EA), or

dimethylammonium (DMA), can spontaneously create a two-dimensional (2D) passivation layer at the buried interface, as suggested by Ref. [40].

At the perovskite/NiOx interface, the 2D phase could not form with EA, DMA, or BA. Due to abundance of $–NH_2$ groups and symmetric structure, only GUA could form the 2D $GUA2PbI_4$ phase at the buried contact. The uncoordinated oxygen in NiO_X and the $–NH_2$ groups in GUA formed a hydrogen bond that is responsible for the formation of the 2D phase, which served as nuclei for development and protection of the NiO_X surface is sometimes lacking in Ni. Thus, decreasing the buried interface defects and inhibiting nonradiative recombination at the interface, this strategy record 22.9 % PCE of NiOx-based inverted PSCs. Unfortunately, the stability of the device was complicated by the tendency of these organic monoammonium ligands to create preferential 2D structures that are not in-plane [246,247]. Consequently, 1,3-propanediamine dihydriodide ($PDAI_2$), 1, 6-hexamethylenediamine dihydriodide ($HDAI_2$), and 1,4-butanediamine dihydriodide ($BDAI_2$) are the three examples of alkyldiammonium salts that Chen et al. added to perovskite precursors [248]. Because of the interaction of the BDA ligand's bicephalous ammonium groups with the two VFA sites, density functional theory (DFT) studies showed that it had the largest energy absorption for VFA when compared to two other ligands (Fig. 16d). This helped to improve the level of the energy structure of the perovskite's upper surface and reduce the defect density. As a result, a high PCE of 23.1 % and 20.9 % were respectively achieved by the inverted PSCs with $BDAI_2$ using flexible substrates under MPPT with 92 % of the starting efficiency during a 1000-h period.

Inverted PSCs frequently include polymer additives in addition to the compounds discussed above [249,250]. Nevertheless, certain changes have multiple functions and there are insufficient experimental techniques. It is still not possible to fully comprehend the concept of additive engineering and passivation mechanisms. In order to enhance the stability and effectiveness of inverted PSCs,

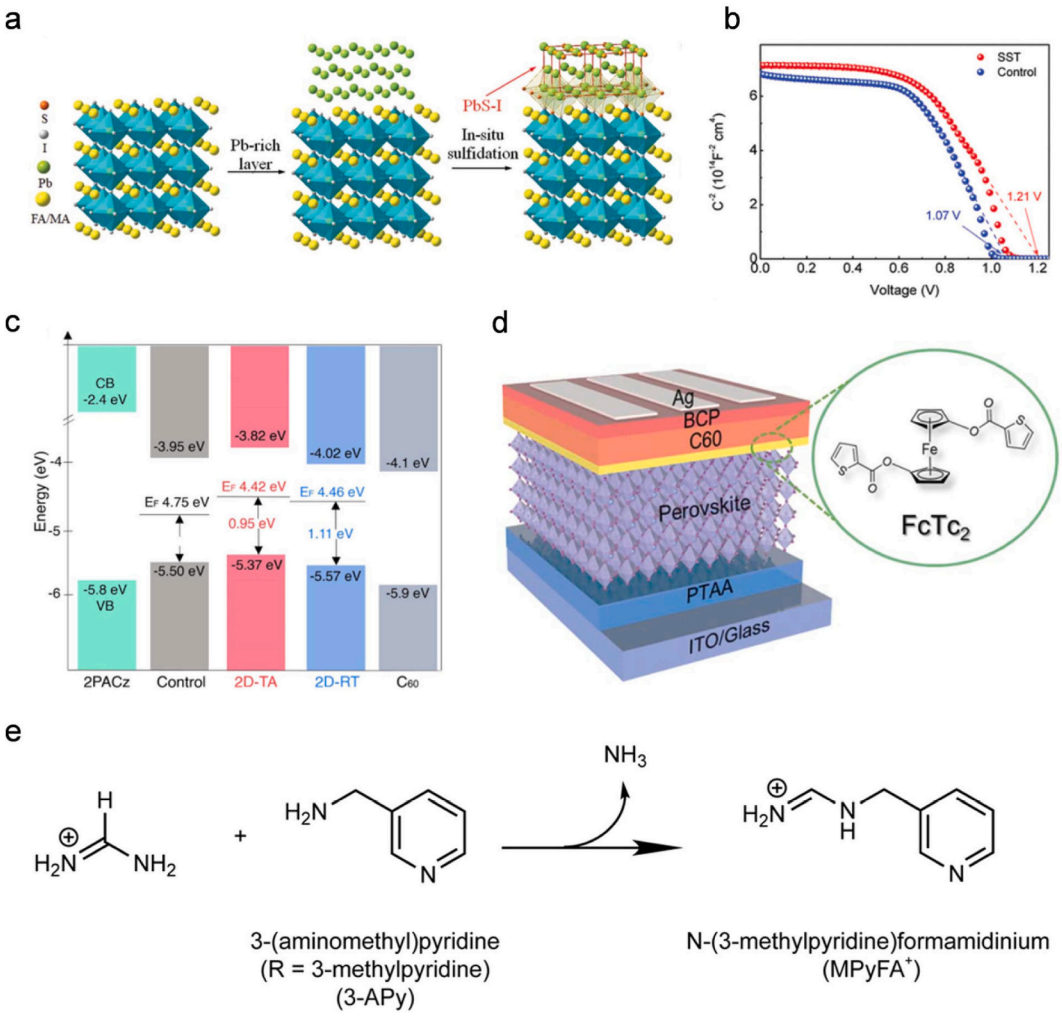

Fig. 17. Perovskite/ETM interface engineering. (a) An SST schematic diagram, (b) Devices with and without SST are represented by Mott-Schottky plots, (c) Diagram of energy levels for 2D-TA and 2D-RT perovskite films that have been treated with OLAI in relation to CTMs, (d) An inverted PSC's device configuration using $FcTc_2$ as the functionalization material between the surfaces, (e) The reaction of condensation between 3-APy and FA^+ is shown schematically [87].

understanding of the additive and passivation mechanism is necessary.

13.2. Interface engineering

Despite the numerous benefits of inverted PSCs, it is important to acknowledge that there remains a significant efficiency gap between them and standard PSCs, potentially endangering the endeavor to implement the p-i-n architecture. The last ten years have seen a substantial advancement in perovskite bulk material optimization, and interfacial engineering have become the primary techniques for maximizing performance of PSCs. As Fig. 19 illustrates, remarkable progress has been achieved in interface engineering to enhance the efficiency of PSCs that are inverted. Consequently, improving the performance of PSCs requires low charge recombination at interfaces. One possible explanation for the interaction between the selective top ETM and the perovskite layer in these PSCs may be the cause of the frequent decreased efficiency in IPSCs when compared to regular PSCs, resulting to more recombination at the interface than typical perovskite/spiro-OMeTAD PSCs [251,252]. In order to avoid interfacial losses, numerous research have been carried out to enhance the C_{60}/perovskite interaction characteristics. Interface engineering techniques have proven to be an efficient means of fine-tuning interface features without compromising the characteristics of bulk layers.

To minimize nonradiative recombination and lessen the discrepancy in efficiency between inverted and conventional PSCs at the perovskite/ETM contact, Fang et al. recommended surface sulfidation. Perovskite sheets high in lead (Pb) were sulfidated to treat inverted PSCs (SST) [22]. Pyridine-2-carboxylic lead ($PbPyA_2$) was spin-coated onto the perovskite layer in order to produce a Pb-rich perovskite surface. After that, solid-phase $PbPyA_2$ was used to spin-coat the top layer of hexamethyldisilathiane (TMS) (Fig. 17a). SST generated an increase in n-type on the surface of the perovskite, which bent the band of the energy surface and produced an additional rear-surface field. This field encouraged carrier transport and raised the device's Vbi (Fig. 17b). Furthermore, the Pb–S bonds were proven to be more resilient than Pb–I bonds due to the robust interactions among Pb ions and S^{2-} anions on the perovskite surface. Inverted PSCs have verified efficiencies higher than 23 % for the first time. After 2200 h at 85 °C for thermal aging, the resultant devices exhibited exceptional thermal stability and 91.8 % of their initial efficiency were maintained. Similarly, Wolf et al. used oleylammonium iodide (OLAI) to create tailored dimensionality dual-layer and tri-layer heterojunctions at room temperature. By

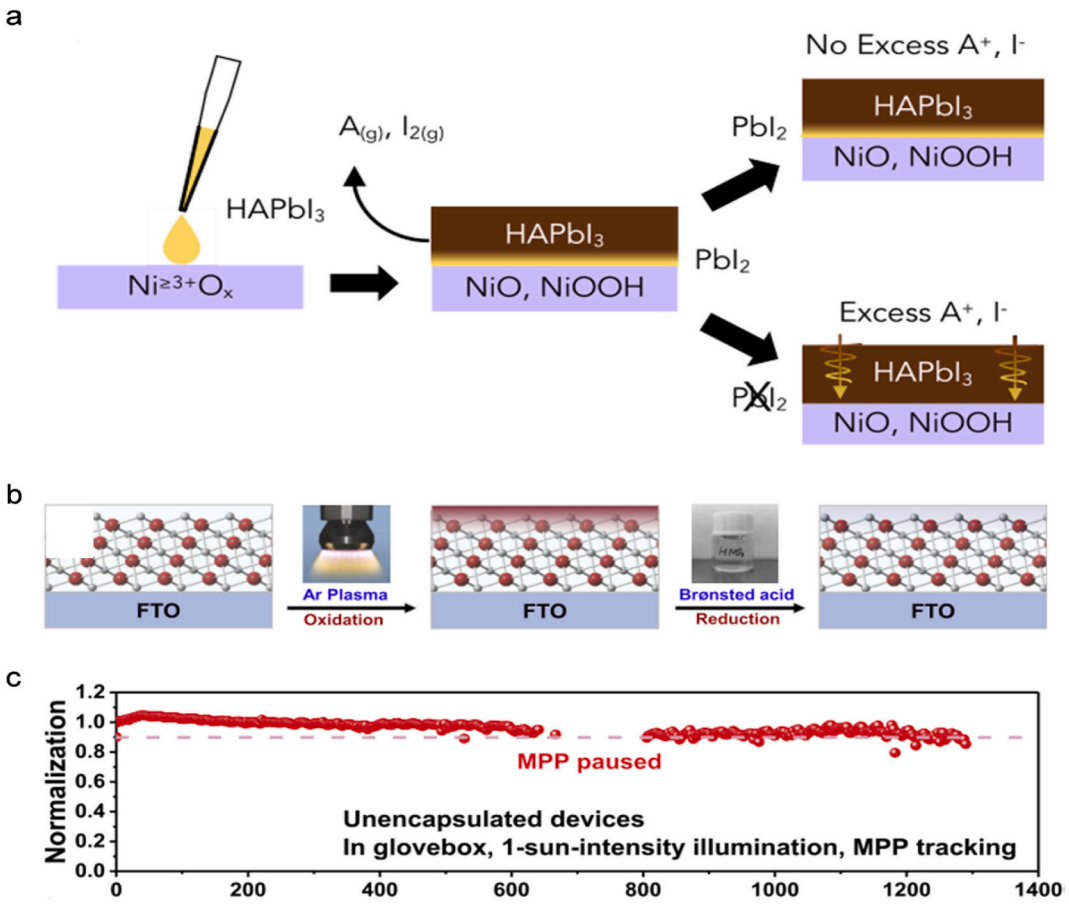

Fig. 18. Perovskite/NiOx interface engineering. (a) Diagram showing the extra titration-reactive A-sites at the NiOx surface that stop $PbI_{2-x}Br_x$ from forming at the interface, (b) Diagrammatic representation of the SRE procedure, (c) Long-term MPPT of SRE-treated devices measured in a glove box with illumination equivalent to one sun [87].

changing the temperature throughout the annealing process from lower to higher, they were able to change the dimension of the 2D perovskite pieces at the inverted PSCs' perovskite/C_{60} interface. These circumstances are critical for 2D perovskite passivation layers for efficient top-contact passivation. Following OLAI post treatment at room temperature, it was noticed that the top 3D-perovskite layers displayed a highly orientated lateral orientation and the low-dimension perovskite layers became significant. This improved the match in energy level between C_{60} and perovskite, and encouraged transport of electrons by moving the VBM of 2D-RT films closer to the CBM of C_{60} (Fig. 17c) [29]. Consequently, in damp-heat test conditions for almost a thousand hours, the passivated 2D inverted PSCs kept over 95 % of their initial efficiency, and they demonstrated a high efficiency of 24.3 %. Zhu et al. suggested $FcTc_2$ as a functionalized material for the interface of perovskite/C_{60} in order to further close the efficiency gap (Fig. 17d) [24].

This compound enhanced electron transport between the ferrocene units that are both electron-rich and electron delocalizing while also reducing surface traps through strong chemical Pb–O binding. These advantages allowed inverted PSCs with $FcTc_2$ passivation to achieve an incredible certified PCE of 24.3 %, V_{OC} of 1.179 V, J_{SC} = 25.59 mA cm^{-2}, and FF = 80.60 %. The resultant PSCs demonstrated exceptional stability as well, passing the damp-heat test (85 °C and 85 % RH) and meeting international requirements (IEC61215:2016). To maximize the efficiency of inverted PSCs, a reactive surface engineering technique based on the simple post-treatment of 3-APy on the perovskite films' top was recently presented by Zhu et al. The 3-APy molecule may react with surface FA^+ alone, as depicted in Fig. 17e [25], lowering the surface roughness of the perovskite. Furthermore, the reduced charged iodine

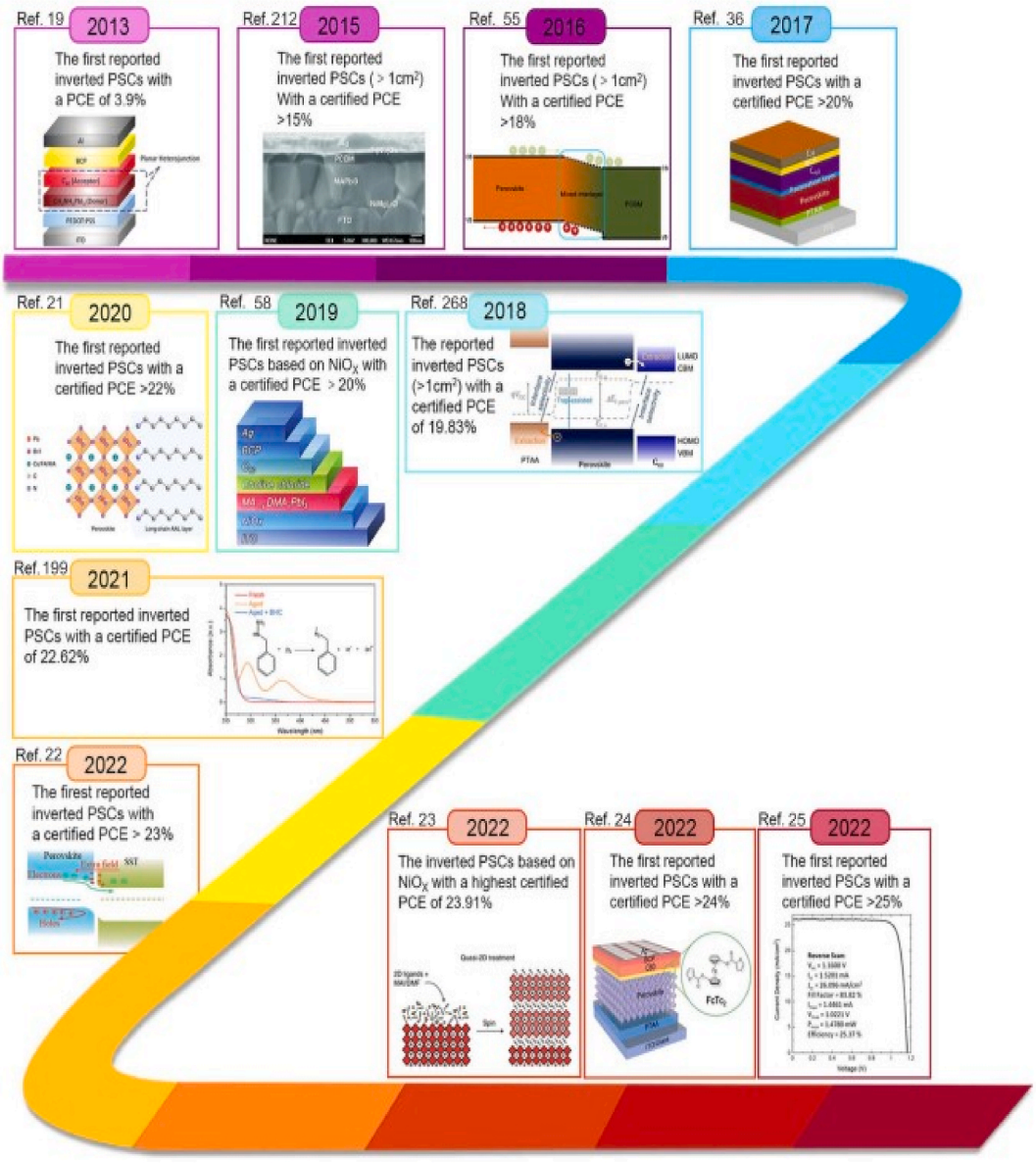

Fig. 19. Efficiency evolution of inverted PSCs reported in representative works [87].

vacancy energy formation on the perovskite surface brought about by the reaction product also increased the n-type of the perovskite surface area, which benefited electron transport. In light of these benefits, the J-V characteristics assessed by NREL showed that the inverted PSC attained the maximum certified PCE of 25.37 %. Additionally, the resultant PSCs showed outstanding operational stability, holding onto 87 % of their early PCE after more than 2400 h of one-sun illumination at an air temperature of roughly 55 °C.

The defect passivation at NiOx/perovskite interface in particular, and the choice of appropriate hole contact layer between it and the interface of the perovskite [206,214], is an efficient way to fabricate stable and effective IPSCs, in furtherance to improving the perovskite/ETM interface properties. As previously indicated, numerous challenging problems arise at the NiOx/perovskite interface due to the intricate surface chemical characteristics of NiO_X, which restrict the advancement of NiO_X-based inverted PSCs. Because these sites can deprotonate cationic amines and oxidize species of iodine in perovskite films, they specifically cause the formation of PbI_2-xBrx at the NiOx/perovskite interface, increasing recombination and acting as a hole extraction barrier and reducing device performance. These sites are found on the surface of NiOx and are identified as Lewis electron acceptors and Brønsted proton acceptors. McGehee et al. (Fig. 18a) [214] offered a straightforward method for modifying the stoichiometry of the perovskite precursor by adding extra FAI, enabling it to react with the $Ni^{\geq 3+}$ cation sites. Based on a NiOx-HTM and a $Cs_{0.25}FA_{0.75}Pb(Br_{0.2}I_{0.8})_3$ perovskite layer, the resulting PSCs had a high PCE of 19.66 % and a high V_{OC} of 1.14 V. Furthermore, the surface wettability of vacuum-treated NiOx films is low, which reduces the adherence of perovskite ink and makes large-area perovskite film deposition difficult. The surface-resident high-oxidative-state $Ni^{\geq 3+}$ species react with the perovskite as well, creating extraction barriers with holes and seriously impairing the chemical reaction at the NiOx/perovskite contact. To produce vacuum-deposited NiO_X appropriate for slot-die-coated perovskite films, Liu et al. developed surface redox engineering (SRE). The SRE method, in short, entailed continuously exposing the NiOx films to a reduction process mediated by Brønsted acid (HNO_3) and an oxidation process initiated by Argon (Ar)

Table 1
The typical performance of some selected IPSCs device structures.

Device Structure	Nature of Investigation	J_{SC} (mA cm^{-2})	V_{OC} (V)	FF (%)	PCE (%)	Ref.
CaF_2/ITO/Spiro-OMeTAD/ZnO/Graphene	Simulation	28.72	1.62	86.39	29.26	[255]
CaF_2/ITO/Cu_2O/ZnO/Graphene	Simulation	27.53	1.62	86.39	28.06	[255]
ITO/PEDOT:PSS/$MAPbI_3$/C_{60}/LiF/Ag	Experimental	20.20	0.96	81.00	16.40	[256]
PETUG/PEDOT:PSS/NPB/$MAPbI_3$/PCBM/BCP/Ag	Experimental	20.49	1.00	70.30	14.39	[257]
ITO/PTAA/$MAPbI_3$/PCBM/Ag	Experimental	12.73	0.78	64.00	6.37	[258]
FTO/$Cu_yCr_zO_2$/$MAPbI_3$/PCBM/Ag	Experimental	20.08	1.07	70.00	15.30	[259]
FTO/Cu:C_rO_x/$MAPbI_3$/PCBM/Ag	Experimental	16.02	0.98	70.00	10.99	[260]
ITO/PEDOT:PSS/$MAPbI_{3-x}Cl_x$/C_{60}/Bphen/Ca/Ag	Experimental	20.90	1.02	72.20	15.4	[261]
ITO/PTAA/$FA_{0.4}MA_{0.6}PbI_3$/C_{60}/Cu	Experimental	23.00	1.03	77.00	18.30	[262]
FTO/$CH_3NH_3SnI_3$/C_{60}/Au	Simulation	32.45	0.85	73.72	20.54	[263]
ITO/NiO/$CH_3NH_3SnI_3$/PCBM/Al	Simulation	33.45	0.97	70.33	22.95	[264]
FTO/NiO/$CH_3NH_3PbI_3$/ZnO/Al	Simulation	22.17	1.05	76.78	17.84	[265]
ITO/NiO/$CH_3NH_3PbI_3$/ZnO/Al	Simulation	21.00	0.99	76.10	15.80	[266]
ITO/Cu_2O/$CH_3NH_3PbI_3$/PCBM/Al	Simulation	22.40	1.30	85.50	25.00	[267]
ITO/CuSCN/$CH_3NH_3PbI_3$/PCBM/Al	Simulation	21.60	1.30	89.10	25.30	[267]
ITO/CuI/$CH_3NH_3PbI_3$/PCBM/Al	Simulation	22.30	1.30	90.40	26.30	[267]
ITO/PEDOT:PSS/$MAPbI_3$/PCBM/Ca/Al	Experimental	23.51	1.30	83.00	20.10	[100]
ITO/PTAA/SSG-$(FAPbI_3)_{0.85}(MAPbBr_3)_{0.15}$/PCBM/$C_{60}$/BCP/Cu	Experimental	21.86	1.17	81.00	20.90	[268]
ITO/Cu-NiOX/$MAPbI_{3-x}Cl_x$/PCBM/ZrAcac/Ag	Experimental	23.07	1.12	77.00	20.50	[269]
ITO/CuO_X/$MAPbI_{3-X}Cl_X$/PCBM/C_{60}/BCP/Ag	Experimental	22.50	1.11	75.80	19.00	[270]
ITO/CuSCN/$MAPbI_3$/PCBM/Bis-C_{60}/Ag	Experimental	19.60	1.07	74.00	16.00	[271]
ITO/rGO/PTAA/$MAPbI_3$/PCBM/BCP/Ag	Experimental	20.30	1.07	77.70	17.20	[272]
FTO/NiO_X/SP3 passivated $MAPbI_3$/PCBM/BCP/Ag	Experimental	22.69	1.12	78.60	20.43	[273]
ITO/PTAA/$(FA_{0.83}MA_{0.17})_{0.95}Cs_{0.05}Pb(I_{0.6}Br_{0.4})_3$/ICBA/$C_{60}$/BCP/Cu	Experimental	19.70	1.20	77.50	18.30	[274]
FTO/NiO_X/$FA_{1-X}MA_XPbI_3$/PCBM/TiO_X/Ag	Experimental	23.09	1.10	81.40	20.65	[275]
ITO/NiO_X/$MAPbI_3$/ZnO/Al	Experimental	21.00	1.01	76.00	16.10	[276]
ITO/PEDOT:PSS/$MAPbI_{3-X}Cl_X$/$PC_{70}BM$/AZO/Al	Experimental	18.50	0.90	80.00	13.30	[277]
ITO/NiO/$MAPbI_3$/C_{60}/SnO_2 nanoparticles/Ag	Experimental	21.80	1.12	77.00	18.80	[278]
ITO/PEDOT:PSS/$MAPbI_3$/C_{60}/BCP/Al	Experimental	10.32	0.6	58	3.9	[19]
FTO/NiMgLiO/$MAPbI_3$/PCBM/Ti(Nb)O_X/Ag	Experimental	20.62	1.072	74.8	16.2	[212]
FTO/NiMgLiO/$MAPbI_3$:PCBM/PCBM/Ti(Nb)O_X/Ag	Experimental	21.98	1.08	79	18.75	[55]
ITO/PTAA/$FA_{0.85}MA_{0.15}Pb(I_{0.85}Br_{0.15})_3$/Choline chloride/$C_{60}$/BCP/Cu	Experimental	23.7	1.14	78	21.0	[36]
ITO/PTAA/PFN-P2/$(CsPbI_3)_{0.05}$[$(FAPbI_3)_{0.83}(MAPbBr_3)_{0.17}]_{0.95}$/LiF/$C_{60}$/BCP/Cu	Experimental	22.24	1.132	80.5	20.3	[268]
ITO/NiO_X/$MA_{0.89}DMA_{0.11}PbI_3$/Choline chloride/C_{60}/BCP/Ag	Experimental	23.5	1.116	82	21.6	[269]
ITO/PTAA/$Cs_{0.05}(FA_{0.92}MA_{0.08})_{0.95}Pb(I_{0.92}Br_{0.08})_3$/$C_{60}$/BCP/Cu	Experimental	24.1	1.17	81.6	23.0	[21]
TO/PTAA/$Cs_{0.05}(FA_{0.95}MA_{0.05})_{0.95}Pb(I_{0.95}Br_{0.05})_3$/$C_{60}$/BCP/Ag	Experimental	23.9	1.17	83.6	23.4	[199]
ITO/P3CT-N/$(FAPbI_3)_{0.95}(MAPbBr_3)_{0.05}$/PCBM/$C_{60}$/TPBi/Cu	Experimental	24.8	1.19	82.9	24.3	[22]
ITO/NiOx/$Cs_{0.05}FA_{0.85}MA_{0.1}PbI_3$/3F-PEAI/PCBM/BCP/Ag	Experimental	24.9	1.15	83.46	23.91	[23]
ITO/PTAA/$Cs_{0.05}(FA_{0.98}MA_{0.02})_{0.95}Pb(I_{0.98}Br_{0.02})_3$/$FcTc_2$/$C_{60}$/BCP/Ag	Experimental	25.68	1.184	82.32	25.0	[24]
ITO/MeO-2PACZ/$Rb_{0.05}Cs_{0.05}MA_{0.05}FA_{0.85}Pb(I_{0.95}Br_{0.05})_3$/3-APy/LiF/$C_{60}$/BCP/Ag	Experimental	26.10	1.161	83.82	25.37	[25]

plasma (Fig. 18b) [253]. At the NiO_X/perovskite contact, this enhanced the energy-band alignment and prevented unfavorable chemical reactions and to enhancing the perovskite ink's wetting ability on the vacuum-deposited NiO_X surface. Consequently, the flexible and stiff devices' inverted PSCs with NiOx as the HTM, respectively, produced outstanding PCEs of 23.4 % and 21.3 %. Additionally, in a glovebox with MPPT and continuous one-sun illumination for more than 1300 h, the un-encapsulated SREPSCs demonstrated improved stable operations, retaining 90 % of their original effectiveness (Fig. 18c). Additionally, the 156 × 156 mm^2 perovskite sub-modules with a superior perovskite layer that was created by slot-die coating demonstrated an impressive PCE of 18.6 %. In addition, Qi et al. recently discovered that, under one-sun illumination, the iodide's oxidation and the generation of free protons at the contact between NiOx and perovskite led to undesirable multistep photochemical processes that ultimately culminated in the NiOx-based photo degradation of inverted PSCs [216]. To prevent this photo degradation, they suggested putting in a buffer layer of trimethylsulfonium bromide (TMSBr) at the NiOx/perovskite contact. Because of its special qualities, aprotic TMS^+ can decrease the trap density, preserve lattice coherence, and stop the contact reaction between perovskite and NiOx. After operating continuously for 2000 h under AM1.5 G light irradiation, the resulting PSCs that are inverted and have the TMSBr buffer layer demonstrated enhancement and sustained 82.8 % of their original PCE and achieved long-term operational stability.

The conversation above suggests that interface engineering is crucial to the creation of highly effective inverted PSCs. Carrier recombination brought on by dangling bonds and defect states is responsible for the excessive amount of nonradiative recombination at the interface which is a key justification for interface engineering [254]. It is important to keep the following in mind when designing interface for inverted PSCs: (i) In order to reduce the interface's carrier recombination, the p-n junction at the interface generates a built-in electric field (Vbi), which is primarily dictated by the carrier separation speed. Vbi is strongly related to the device's V_{OC}. Given that charge separation is the driving force behind Vbi, interface engineering should be a useful strategy (electrons and holes flowing toward two opposed interfaces). (ii) The second important factor in efficient charge extraction is carrier extraction, which is meant to occur quickly and is based on the perovskite/CTM interface's energy level alignment. In summary, the perovskite layer's conduction band energy level (Ec) ought to surpass the ETM's, while its valence band energy level (Ev) ought to be less than the HTMs. By effectively reducing the carrier band offset and aligning the energy levels, interface engineering has been used to prevent interfacial recombination. (iii) The interfacial charge dynamics depend equally on the high carrier mobilities of CTMs. In order to achieve favorable charge dynamics at interfaces, there should be high conductivity and functional groups in the interlayers. This will enable the use of interface dipoles to reduce carrier losses and passivate interfacial imperfections. (iv) The interlayer should enhance device stability in addition to the previously listed capabilities. An $FcTc_2$ interlayer, for instance, enhanced device stability by reducing the perovskite surface's defect states by forming strong chemical Pb–O binding and promoting carrier transport through its organic functional groups [24]. (v) Interface engineering is currently widely employed for small-area PSCs (usually with an active area of less than 1 cm^2), but it presents a hurdle when applied to large-area modules due to spin coating techniques. For large-area and high-efficiency inverted PSCs, techniques such atomic layer deposition, screen printing, and thermal evaporation need to be established to ensure deposition of homogeneous and dense interface layers.

14. Conclusion and future outlook

Recent years have seen a rapid development of inverted PSCs. Several efforts have been undertaken to raise the perovskite films' quality, create suitable CTMs, and experiment with different defect passivation techniques in order to raise the inverted PSCs' narrow aperture regions' efficiency, ranged from 3.9 % [19] to 25.37 % [25]. An inverted perovskite mini-module with a high certified PCE of 21.07 % [27] was also attained. The commercialization potential of inverted PSCs is feasible because both inverted PSCs with small area size [24,29] and mini-modules made of perovskite [273] have successfully accomplished stability tests (during moist heat at 85 °C and 85 % RH) according to international standard IEC 61215:2016. However, there is still a noticeable difference (24.05 % against 25.7 %) in the verified stability of the inverted PSCs' efficiency and conventional PSCs respectively. The efficiency progress and performance of some selected inverted perovskite solar cell devices is presented in Table 1 and the Fig. 19. The following actions are suggested in order to increase the efficiency of inverted PSCs and make them competitive with other counterpart solar cells.

i. In tandem solar cells made entirely of perovskite, the inverted structure employing organic charge transport carriers like PEDOT:PSS is therefore preferred. In a reaction of proportionation, metallic tin was employed to convert Sn^{4+} to Sn^{2+}, yielding a PCE of 22.1 % in all-perovskite tandem solar cells [63]. Further research was conducted by this team of researchers, which resulted in the development of a triple-junction perovskite solar cell with a PCE above 20 % [64,65]. This implies that, the combination of PSCs with either $Cu(In,Ga)Se_2$ or silicon or any other appropriate semiconductor will increase potential for solar energy applications to create an IPCs-based tandem solar cells of over 40 % efficiency.
ii. HTMs have a significant impact on the inverted PSCs' J_{SC}. For instance, PTAA-based PSCs typically have a higher J_{SC} than NiOx-based inverted PSCs [23,24]. Since a PSC's carrier separation and transfer are determined by the CTM, more appropriate CTMs ought to be created.
iii. With efficiencies higher than 23 %, the majority of inverted PSCs are achieved on the basis of organic HTMs such as SAMs and PTAA. Nonetheless, conditions that are humid and hot can cause the degradation of organic HTMs. Recently, under damp heat (85 °C and 85 % RH), according to the IEC61215:2016 standard, IPSCs based on PTAA or 2PACz passed the test, indicating excellent commercialization possibilities. Conversely, the cost of organic HTMs typically restricts the use of PSCs. Furthermore, when exposed to light and heat continuously, inverted PSCs with PTAA show less stability than NiOx-based devices as a result of severe bulk decomposition and interface deterioration due to the formation of voids caused by the release of I_2 gas from defective regions at grain boundaries [279]. NiOx, the most promising inorganic HTM available right now, is used in inverted

PSCs because of its outstanding thermal stability, strong environmental stability, and cheap cost of synthesis [206]. However, the low efficiency of NiOx-based inverted devices continue to be a barrier to commercialization due to their surface trap states and low intrinsic conductivity. Consequently, further work is required to improve NiOx's film quality through surface modification or doping, in order to reach a competitive efficiency of 25 % with high photoelectric characteristics similar to conventional organic HTMs.

iv. Encapsulation technology is critical to the stability of the device. Tests for operational and thermal stability typically involve encapsulated devices, suggesting that encapsulation technique plays a critical role in enhancing device stability. In this case, incorporating strong barriers like internal encapsulation technologies within PSCs is crucial for maintaining device stability. This can stop unwanted ions' transport and shield the layer of perovskite from external moisture degradation. To lessen the harmful interfacial diffusion of ions, Han et al. for example, introduced low-dimensional diffusion barriers (DBLs) to the perovskite films [273]. Consequently, successful confirmation of the industry-based damp-heat test at 85 °C and 85 % RH was achieved by the perovskite solar modules. Furthermore, because of the fact that exterior encapsulation technology is inexpensive and can effectively prevents moisture and oxygen infiltration, it is also frequently employed in the PSC industry [209]. The durability of the related IPSCs with a T80 lifetime of 1000 h was greatly enhanced when Lidzey et al. sandwiched a PSC and epoxy-coated encapsulated glass slide between a solution polymer interlayer known as polyvinylpyrrolidone (PVP) [280]. A limited number of papers have substantiated that PSCs do not only successfully pass industry-relevant damp-heat tests (85 °C and 85 % RH) but also passed stability tests conducted by third parties [24,29]. This highlights the importance of creating inverted PSC encapsulation technology, which is essential to advancing the commercialization of inverted PSCs.

v. The field of machine learning (ML) presents prospects in identifying distinct characteristics for common materials for novel scientific findings and applications [281]. This suggests the usage of ML in forecasting the suitable bandgap, electronic transport, catalytic, stability, light emitting and sensing properties of perovskite materials for photovoltaic applications to enhanced performance.

Funding

This article did not receive any funding support

Data availability statement

The data that support the findings can be made available upon reasonable request.

CRediT authorship contribution statement

Emmanuel A. Nyiekaa: Writing – review & editing, Writing – original draft, Data curation, Conceptualization. **Timothy A. Aika:** Resources, Formal analysis, Data curation. **Patience E. Orukpe:** Writing – review & editing, Supervision, Investigation. **Christopher E. Akhabue:** Writing – review & editing, Supervision, Methodology. **Eli Danladi:** Writing – review & editing, Validation, Supervision, Methodology.

Declaration of competing interest

The authors declare that they have no known competing financial interests or personal relationships that could have appeared to influence the work reported in this paper.

References

[1] E. Danladi, et al., Impact of transport material on perovskite solar cells with different metal electrode: a SCAPS-1D simulation insight, Heliyon 9 (2023), https://doi.org/10.1016/j.heliyon.2023.e16838.
[2] I. Celik, et al., Environmental Analysis of Perovskites and Other Relevant Solar Cell Technologies in a Tandem Configuration, Energy and Environmental Science10, 2017, p. 1874, https://doi.org/10.1039/C7EE01650F, 1184.
[3] C. Battaglia, et al., High-efficiency crystalline silicon solar cells: status and perspectives, Energy Environ. Sci. 9 (2016) 1552–1576, https://doi.org/10.1039/C5EE03380B.
[4] X. Ren, et al., Topology and texture controlled ZnO thin film electrodeposition for superior solar cell efficiency, Sol. Energy Mater. Sol. Cell. 134 (2015) 54–59, https://doi.org/10.1016/j.solmat.2014.11.026.
[5] J. Ramanujam, U.P. Singh, Copper indium gallium selenide based solar cells – a review, Energy Environ. Sci. 10 (2015) 1306–1319, https://doi.org/10.1039/C7EE00826K.
[6] T. Feurer, et al., Progress in thin film CIGS photovoltaics - research and development, manufacturing, and applications, Prog. Photovoltaics Res. Appl. 25 (7) (2017) 645–667, https://doi.org/10.1002/pip.2811.
[7] J.D. Major, Grain Boundaries in CdTe Thin Film Solar Cells: a Review. Semiconductor Science and Technology, 2016, https://doi.org/10.1088/0268-1242/31/9/0930001, 31.
[8] B.M. Basol, B. McCandless, Brief review of cadmium telluride-based photovoltaic technologies, J. Photon. Energy 4 (1) (2014), https://doi.org/10.1117/1.JPE.4.040996.
[9] G.H. Carey, et al., Colloidal quantum dot solar cells, Chem. Rev. 115 (23) (2015) 12732–12763, https://doi.org/10.1021/acs.chemrev.5b00063.
[10] L.Y. Lu, et al., Recent advances in bulk heterojunction polymer solar cells, Chem. Rev. 115 (23) (2015) 12666–12731, https://doi.org/10.1021/acs.chemrev.5b00098.
[11] B. Saparov, D.B. Mitzi, Organic–inorganic perovskites: structural Versatility for functional materials design, Chem. Rev. 116 (7) (2016) 4558–4596, https://doi.org/10.1021/acs.chemrev.5b00715.

[12] O.M. Durodola, C. Ugwu, E. Danladi, Highly efficient lead-free perovskite solar cell based on Magnesium-doped copper delafossite hole transport layer: a SCAPS-1D framework prospect, Emergent Materials (2023) 1–20, https://doi.org/10.1016/j.jics.2023.101001.
[13] X. Lin, et al., Efficiency progress of inverted perovskite solar cells, Energy Environ. Sci. 13 (2020) 3823–3847, https://doi.org/10.1039/D0EE02017F.
[14] K. Wojciechowski, et al., C_{60} as an efficient n-type compact layer in perovskite solar cells, J. Phys. Chem. Lett. 6 (12) (2015) 2399–2405, https://doi.org/10.1021/acs.jpclett.5b00902.
[15] G.C. Xing, et al., Interfacial electron transfer barrier at contact $TiO_2/CH_3NH_3/PbI_3$ heterojunction, Small 11 (29) (2015) 3606–3613, https://doi.org/10.1002/smll.201403719.
[16] Q. Jiang, et al., Enhanced electron extraction using SnO_2 for high-efficency planar-struture $HC(NH_2)2PbI_3$-based perovskite solar cells, Nat. Energy 2 (1) (2017) 16177, https://doi.org/10.1038/nenergy.2016.177.
[17] Q. Jiang, et al., Surface passivation of perovskite film for efficient solar cells, Nature Photonics 13 (7) (2019) 460–466, https://doi.org/10.1038/s41566-019-0398-2.
[18] L. Hao, et al., A tin-based perovskite solar cell with an inverted hole-free transport layer to achieve high energy conversion efficiency by SCAPS device simulation, Opt. Quant. Electron. 53 (2021) 524, https://doi.org/10.1007/s11082-021-03175-5.
[19] J.Y. Jeng, et al., $CH_3NH_3PbI_3$/Perovskite/Fullerene planar-heterojunction hybrid solar cells, Adv. Mater. 25 (27) (2013) 3727–3732, https://doi.org/10.1002/adma.201301327.
[20] W. Chen, et al., Efficient and stable large-area perovskite solar cells with inorganic charge extraction layers, Science 350 (6265) (2015) 944–948, https://doi.org/10.1126/science.aad1015.
[21] X.P. Zheng, et al., Managing grains and interfaces via ligand anchoring enables 22.3%-efficiency inverted perovskite solar cells, Nat. Energy 5 (2020) 131–140, https://doi.org/10.1038/s41560-019-0538-4.
[22] X. Li, et al., Constructing heterojunctions by surface sulfidation for efficient inverted perovskite solar cells, Science 375 (2022) 434–437, https://doi.org/10.1126/science.abl5676.
[23] H. Chen, et al., Quantum-size-tuned heterostructures enable efficient and stable inverted perovskite solar cells, Nat. Photonics 16 (2022) 352–358, https://doi.org/10.1038/s41566-022-00985-1.
[24] Z. Li, et al., Organometallic-functionalized interfaces for highly efficient inverted perovskite solar cells, Science 376 (2022) 416–420, https://doi.org/10.1126/science.abm8566.
[25] Q. Jiang, et al., Surface reaction for efficient and stable inverted perovskite solar cells, Nature 611 (2022) 278–283, https://doi.org/10.1038/s41586-022-05268-x.
[26] S. Chen, et al., Stabilizing perovskite-substrate interfaces for high-performance perovskite modules, Science 373 (2021) 902–907, https://doi.org/10.1126/science.abi6323.
[27] Y. Gao, et al., Can nanosecond laser achieve high-performance perovskite solar modules with aperture area efficiency over 21%? Adv. Energy Mater. 12 (2022) 2202287 https://doi.org/10.1002/aenm.202202287.
[28] M.A. Green, et al., Solar cell efficiency tables (Version 60), Progress in Photovoltaics 30 (7) (2022) 687–701, https://doi.org/10.1002/pip.3595.
[29] R. Azmi, et al., Damp heat–stable perovskite solar cells with tailored dimensionality 2D/3D heterojunctions, Science 376 (2022) 73–77, https://doi.org/10.1126/science.abm5784.
[30] S.-H. Turren-Cruz, A. Hagfeldt, M. Saliba, Methylammonium free, highperformance, and stable perovskite solar cells on a planar architecture, Science 362 (2018) 449–453, https://doi.org/10.1126/science.aat3583.
[31] J.W. Lee, et al., Formamidinium and cesium hybridization for photo-and moisture-stable perovskite solar cell, Adv. Energy Mater. 5 (2015) 1501310, https://doi.org/10.1002/aenm.201501310.
[32] B. Conings, et al., Intrinsic thermal instability of methylammonium lead trihalide perovskite, Adv. Energy Mater. 5 (2015) 1500477, https://doi.org/10.1002/aenm.201500477.
[33] E.J. Juarez-Perez, L.K. Ono, Y.B. Qi, Thermal degradation of formamidinium based lead halide perovskites into sym-triazine and hydrogen cyanide observed by coupled thermogravimetry-mass spectrometry analysis, J. Mater. Chem. A 7 (2019) 16912–16919, https://doi.org/10.1039/C9TA06058H.
[34] W.S. Yang, et al., High-performance photovoltaic perovskite layers fabricated through intramolecular exchange, Science 348 (2015) 1234–1237, https://doi.org/10.1126/science.aaa9272.
[35] Y. Zhao, K. Zhu, Organic–inorganic hybrid lead halide perovskites for optoelectronic and electronic applications, Chem. Soc. Rev. 45 (2016) 655–689, https://doi.org/10.1039/C4CS00458B.
[36] X. Zheng X, et al., Defect passivation in hybrid perovskite solar cells using quaternary ammonium halide anions and cations, Nat. Energy 2 (2017) 1–9, https://doi.org/10.1038/nenergy.2017.102.
[37] C. Yi, et al., Entropic stabilization of mixed A-cation ABX_3 metal halide perovskites for high performance perovskite solar cells, Energy Environ. Sci. 9 (2016) 656–662, https://doi.org/10.1039/C5EE03255E.
[38] G. Fisicaro, et al., Local order and rotational dynamics in mixed A-cation lead iodide perovskites, J. Phys. Chem. Lett. 11 (2020) 1068–1074, https://doi.org/10.1021/acs.jpclett.9b03763.
[39] D. Ghosh, A.R. Smith, Walker, M.S. Islam, Mixed A-cation perovskites for solar cells: atomic-scale insights into structural distortion, hydrogen bonding, and electronic properties, Chem. Mater. 30 (2018) 5194–5204, https://doi.org/10.1021/acs.chemmater.8b01851.
[40] B. Chen, et al., Passivation of the buried interface via preferential crystallization of 2D perovskite on metal oxide transport layers, Adv. Mater. 33 (2021) 2103394, https://doi.org/10.1002/adma.202103394.
[41] Y. Zhao, et al., Inactive $(PbI_2)_2RbCl$ stabilizes perovskite films for efficient solar cells, Science 377 (2022) 531–534, https://doi.org/10.1126/science.abp8873.
[42] J.J. Yoo, et al., Efficient perovskite solar cells via improved carrier management, Nature 590 (2021) 587–593, https://doi.org/10.1038/s41586-021-03285-w.
[43] S. Masi, et al., Chemi-structural stabilization of formamidinium lead iodide perovskite by using embedded quantum dots, ACS Energy Lett. 5 (2020) 418–427, https://doi.org/10.1021/acsenergylett.9b02450.
[44] Z.-A. Nan, et al., Revealing phase evolution mechanism for stabilizing formamidinium-based lead halide perovskites by a key intermediate phase, Chem 7 (2021) 2513–2526, https://doi.org/10.1016/j.chempr.2021.07.011.
[45] M. Kim, et al., Methylammonium chloride induces intermediate phase stabilization for efficient perovskite solar cells, Joule 3 (2019) 2179–2192, https://doi.org/10.1016/j.joule.2019.06.014.
[46] H. Min, et al., Efficient, stable solar cells by using inherent bandgap of α-phase formamidinium lead iodide, Science 366 (2019) 749–753, https://doi.org/10.1126/science.aay7044.
[47] Y. Zhang, et al., Propylammonium chloride additive for efficient and stable $FAPbI_3$ perovskite solar cells, Adv. Energy Mater. 11 (2021), https://doi.org/10.1002/aenm.202102538.
[48] D. Zhang, et al., Stable α-FAPbI3 in inverted perovskite solar cells with efficiency exceeding 22% via a self-passivation strategy, Adv. Funct. Mater. 32 (2022), https://doi.org/10.1002/adfm.202200174.
[49] F.X. Xie, et al., Vacuum-assisted thermal annealing of CH3NH3PbI3 for highly stable and efficient perovskite solar cells, ACS Nano 9 (2015) 639–646, https://doi.org/10.1021/nn505978r.
[50] K.C. Wang, et al., P-type mesoporous niked oxide/organometallic perovskite heterojunction solar cells, Sci. Rep. 4 (1) (2014) 4756, https://doi.org/10.1038/srep04756.
[51] W. Chen, et al., Hybrid interfacial layer leads to solid performance improvement of inverted solar cells, Energy Environ. Sci. 8 (2) (2015) 629–640, https://doi.org/10.1039/C4EE02833C.
[52] C.H. Chiang, C.G. Wu, Bulk heterojunction perovskite-PCBM solar cells with high fill factor, Nat. Photonics 10 (3) (2016) 196–200, https://doi.org/10.1038/nphoton.2016.3, 2016.

[53] Z.Y. Liu, et al., Improvement in the performance of inverted planar perovskite solar cells via the $CH_3NH_3PbI_3$-xClx: ZnO bulk heterojunction, J. Power Sources 401 (2018) 303–311, https://doi.org/10.1016/j.jpowsour.2018.09.007.

[54] H. Min, et al., Efficient , stable solar cells by using inherent bandgap of α-phase formamidinium lead iodide, Science 366 (6466) (2019) 749–753, https://doi.org/10.1126/science.aay7044.

[55] Y.Z. Wu, et al., Perovskite solar cells with 18.21% efficiency and area over $1cm^2$ fabricated by heterojunction engineering, Nat. Energy 1 (11) (2016) 1–7, https://doi.org/10.1038/nenergy.2016.148.

[56] Y. Lin, et al., π-Conjugated Lewis base: efficient trap-passivation and charge-extraction for hybrid perovskite solar cells, Adv. Mater. 29 (17) (2017) 1604545, https://doi.org/10.1002/adma.201604545.

[57] A. Ishii, A.K. Jena, T. Miyasaka, Fullycrystalline perovskite-perlene hybrid photovoltaic cell capable of 1.2 V output with a minimized voltage loss, Applied Materials 2 (2014) 091102, https://doi.org/10.1063/1.4895039.

[58] H. Chen, et al., Efficient and stable inverted perovskite solar cells incorporating secondary amines, Adv. Mater. 31 (46) (2019), https://doi.org/10.1002/adma.201903559, 2019.

[59] J.X. Xu, et al., Tripple-halid wide-bandgap perovskites with suppressed phase segregation for efficient tandems, Science 367 (6482) (2020) 1097–1104, https://doi.org/10.1126/science.aaz5074.

[60] D. Kim, et al., Efficient, stable silicon tandem cells enabled by anion-engineered wide-bandgap perovskites, Science 368 (6487) (2020) 155–160, https://doi.org/10.1126/science.aba3433, 2020.

[61] Q.F. Han, et al., High-performance perovskite/Cu(In,Ga)Se_2 monolithic tandem solar cells, Science 361 (6405) (2018) 904–908, https://doi.org/10.1126/science.aat5055.

[62] M.A. Green, et al., Solar cells efficiency tables (version 56), Prog. Photovoltaics Res. Appl. 28 (7) (2020) 629–638, https://doi.org/10.1002/pip.3303.

[63] R.X. Lin, et al., Monolithic all-perovskite tandem solar cells with 24.8% efficiency exploiting comproportionation to suppress Sn(II) oxidation in precursor ink, Nat. Energy 4 (10) (2019) 864–873, https://doi.org/10.1038/s41560-019-0466-3.

[64] K. Xiao, et al., Solution-processed monolithic all-perovskite triple-junction solar cells with efficiency exceeding 20, ACS Energy Lett. 5 (9) (2020) 2819–2826, https://doi.org/10.1021/acsenergylett.0c01184.

[65] Z.H. Yu, et al., Simplified interconnection structure based on $C_{60}/Sn)_{2-x}$ for all-perovskite tandem solar cells, Nat. Energy 5 (9) (2020) 657–665, https://doi.org/10.1038/s41560-020-0657-y.

[66] O. Malinkiewicz, et al., Perovskite solar cells employing organic chargetransport layers, Nat. Photonics 8 (2014) 128–132, https://doi.org/10.1038/nphoton.2013.341.

[67] C. Momblona, et al., Efficient vacuum deposited pin and nip perovskite solar cells employing doped charge transport layers, Energy Environ. Sci. 9 (2016) 3456–3463, https://doi.org/10.1039/C6EE02100J.

[68] Y.-H. Chiang, M. Anaya, S.D. Stranks, Multisource vacuum deposition of methylammonium-free perovskite solar cells, ACS Energy Lett. 5 (2020) 2498–2504, https://doi.org/10.1021/acsenergylett.0c00839.

[69] Y. Choi, et al., A vertically oriented two-dimensional Ruddlesden–Popper phase perovskite passivation layer for efficient and stable inverted perovskite solar cells, Energy Environ. Sci. 15 (2022) 3369–3378, https://doi.org/10.1039/D2EE00759B.

[70] J. Jeong, et al., The introduction of a perovskite seed layer for high performance perovskite solar cells, J. Mater. Chem. A 6 (2018) 20138–20144, https://doi.org/10.1039/C8TA07617K.

[71] C.-H. Chiang, et al., The synergistic effect of H2O and DMF towards stable and 20% efficiency inverted perovskite solar cells, Energy Environ. Sci. 10 (2017) 808–817, https://doi.org/10.1039/C6EE03586H.

[72] E. Gutierrez-Partida, et al., Large-grain double cation perovskites with 18 μs lifetime and high luminescence yield for efficient inverted perovskite solar cells, ACS Energy Lett. 6 (2021) 1045–1054, https://doi.org/10.1021/acsenergylett.0c02642.

[73] M. Li, et al., Comparison of processing windows and electronic properties between CH3NH3PbI_3 perovskite fabricated by one-step and two-step solution processes, Org. Electron. 63 (2018) 159–165, https://doi.org/10.1016/j.orgel.2018.09.011.

[74] W. Chen, et al., Hybrid interfacial layer leads to solid performance improvement of inverted perovskite solar cells, Energy Environ. Sci. 8 (2015) 629–640, https://doi.org/10.1039/C4EE02833C.

[75] Y. Shao, Y. Yuan, J. Huang, Correlation of energy disorder and open-circuit voltage in hybrid perovskite solar cells, Nat. Energy 1 (2016) 1–6, https://doi.org/10.1038/nenergy.2015.1.

[76] J. Seo, et al., Benefits of very thin PCBM and LiF layers for solution-processed p–i–n perovskite solar cells, Energy Environ. Sci. 7 (2014) 2642–2646, https://doi.org/10.1039/C4EE01216J.

[77] N.J. Jeon, et al., Solvent engineering for high-performance inorganic-organic hybrid perovskite solar cells, Nat. Mater. 13 (2014) 897–903, https://doi.org/10.1038/nmat4014.

[78] M. Xiao, et al., A fast deposition-crystallization procedure for highly efficient lead iodide perovskite thin-film solar cells, Angew. Chem. Int. Ed. 53 (2014) 9898–9903, https://doi.org/10.1002/anie.201405334.

[79] K.M. Lee, et al., Selection of anti-solvent and optimization of dropping volume for the preparation of large area sub-module perovskite solar cells, Sol. Energy Mater. Sol. Cells 172 (2017) 368–375, https://doi.org/10.1016/j.solmat.2017.08.010.

[80] A.D. Taylor, et al., A general approach to high-efficiency perovskite solar cells by any antisolvent, Nat. Commun. 12 (2021) 1–11, https://doi.org/10.1038/s41467-021-22049-8.

[81] F. Huang, et al., Gas-assisted preparation of lead iodide perovskite films consisting of a monolayer of single crystalline grains for high efficiency planar solar cells, Nano Energy 10 (2014) 10–18, https://doi.org/10.1016/j.nanoen.2014.08.015.

[82] X. Li, et al., A vacuum flash–assisted solution process for high-efficiency large area perovskite solar cells, Science 353 (2016) 58–62, https://doi.org/10.1126/science.aaf8060.

[83] T. Bu, et al., Dynamic antisolvent engineering for spin coating of 10 × 10 cm^2 perovskite solar module approaching 18%, Sol. RRL 4 (2020) https://doi.org/10.1002/solr.201900263.

[84] N.G. Park, K. Zhu, Scalable fabrication and coating methods for perovskite solar cells and solar modules, Nat. Rev. Mater. 5 (2020) 333–350, https://doi.org/10.1038/s41578-019-0176-2.

[85] Y. Deng, et al., Tailoring solvent coordination for high-speed, roomtemperature blading of perovskite photovoltaic films, Sci. Adv. 5 (12) (2019), https://doi.org/10.1126/sciadv.aax7537.

[86] Z. Yang, et al., Slot-die coating large-area formamidinium-cesium perovskite film for efficient and stable parallel solar module, Sci. Adv. 7 (8) (2021), https://doi.org/10.1126/sciadv.abg3749.

[87] S. Liu, V.P. Biju, Y. Qi, et al., Recent progress in the development of high-efficiency inverted perovskite solar cells, NPG Asia Mater. 15 (27) (2023), https://doi.org/10.1038/s41427-023-00474-z.

[88] I. Zimmermann, et al., Sequentially slot-die-coated perovskite for efficient and scalable solar cells, Adv. Mater. Interfac. 8 (18) (2021), https://doi.org/10.1002/admi.202100743.

[89] D.K. Lee, D.-N. Jeong, T.K. Ahn, N.G. Park, Precursor engineering for a large-area perovskite solar cell with> 19% efficiency, ACS Energy Lett. 4 (2019) 2393–2401, https://doi.org/10.1021/acsenergylett.9b01735.

[90] J.W. Lee, et al., Tuning molecular interactions for highly reproducible and efficient formamidinium perovskite solar cells via adduct approach, J. Am. Chem. Soc. 140 (2018) 6317–6324, https://doi.org/10.1021/jacs.8b01037.

[91] H.B. Kim, et al., Mixed solvents for the optimization of morphology in solution-processed, inverted-type perovskite/fullerene hybrid solar cells, Nanoscale 6 (12) (2014) 6679–6683, https://doi.org/10.1039/C4NR00130C.

[92] O. Malinkiewicz, et al., Perovskite solar cells employing organic charge-transport layers, Nat. Photonics 8 (2) (2014) 128–132, https://doi.org/10.1038/nphoton.2013.341.

[93] C. Momblona, et al., Efficent vacuum deposition pin and nip perovskite solar cells employing doped charge transport layers, Energy Environ. Sci. 9 (11) (2016) 3456–3463, https://doi.org/10.1039/C6EE02100J.

[94] L. Hu, et al., Sequential deposition of $CH_3NH_3PbI_3$ on planar on planar NiO film for efficient planar perovskite solar cells, ACS Photonics 1 (7) (2014) 547–553, https://doi.org/10.1021/ph5000067, 2014.

[95] Z.G. Xiao, Efficient, high yield perovskite photovoltaic devices grown by interdiffusion of solution-processed precursor stacking layers, Energy Environ. Sci. 7 (8) (2014) 2619–2623, https://doi.org/10.1039/C4EE01138D.

[96] X. Sun, et al., Mixed-solvent-vapour annealing of perovskite for photovoltaic device efficiency enhancement, Nano Energy 28 (2016) 417–425, https://doi.org/10.1016/j.nanoen.2016.08.055.

[97] X.P. Zheng, et al., Defect passivation in hybrid perovskite solar cells using quaternary ammonium halide anions and cations, Nat. Energy 2 (7) (2017) 1–9, https://doi.org/10.1038/nenergy.2017.102.

[98] H. Dong, et al., Pseudohalide-induced recrystallization engineering for $CH_3NH_3PbI_3$ films and its application in highly efficient inverted planar heterojunction perovskite solar cells, Adv. Funct. Mater. 28 (2) (2018), https://doi.org/10.1002/adfm.201704836.

[99] C.G. Wu, et al., High efficiency stable inverted perovskite solar cells without current hysteresis, Energy Environ. Sci. 8 (9) (2015) 2725–2733, https://doi.org/10.1039/C5EE00645G.

[100] C.H. Chiang, et al., The synergistic effect of H_2O and DMF towards stable and 20% efficiency inverted perovskite soalr cells, Energy Environ. Sci. 10 (3) (2017) 808–817, https://doi.org/10.1039/C6EE03586H.

[101] Y.Z. Wu, et al., Thermally stable $MAPbI_3$ perovskite solar cells with efficiency of 19.19% and area of over $1cm^2$ achieved by additive engineering, Adv. Mater. 29 (28) (2017), https://doi.org/10.1002/adma.201701073.

[102] D. Li X, et al., In-situ cross-linking strategy for efficient and operationally stable methylammonium lead iodide solar cells, Nat. Commun. 9 (1) (2018) 3806, https://doi.org/10.1038/s41467-018-06204-2.

[103] K.J. Liao, et al., Off-stoichiometric methylalmonium iodide passivated large-grain perovskite film in ambient air for efficient inverted solar cells, ACS Appl. Mater. Interfaces 11 (43) (2019) 39882–39889, https://doi.org/10.1021/acsami.9b12829.

[104] Z.F. Liu, et al., Open-circuit voltages exceeding 1.26 V in planar methylammonium lead iodide perovsite solar cells, ACS Energy Lett. 4 (1) (2019) 110–117, https://doi.org/10.1021/acsenergylett.8b01906.

[105] D.X. Yuan, et al., Inverted planar [NH_2CH double bond, length as m-dash] NH_2PbI_3 perovskite solar cells with 13.56% efficiency via low temperature processing, Phys. Chem. Chem. Phys. 17 (30) (2015) 19745–19750, https://doi.org/10.1039/C5CP02705E.

[106] F.X. Xie, et al., Vertical recrystallization for highly efficient and stable formamidinium-based inverted-structure perovskite solar cells, Energy Environ. Sci. 10 (9) (2017) 1942–1949, https://doi.org/10.1039/C7EE01675A.

[107] Y. Li, et al., Formamidinium-based lead halide perovskites: structure, properties, and fabrication methodologies, Small Methods 2 (7) (2018) 1700387, https://doi.org/10.1002/smtd.201700387.

[108] W.B. Yan, et al., Highly efficient and stable inverted planar solar cells from $(FAI)_x(MABr)1\text{-}_xPbI_2$ perovskites, Nano Energy 35 (2017) 62–70, https://doi.org/10.1016/j.nanoen.2017.03.001.

[109] C.Y. Yi, et al., Entropic stabilization of mixed A-cationed ABX_3 metal halide perovskites for high performance perovskite solar cells, Energy Environ. Sci. 9 (2) (2015) 656–662, https://doi.org/10.1039/C5EE03255E.

[110] G. Fisicaro, et al., Local order and rotational dynamics in mixed A-cation lead iodide perovskite, J. Phys. Chem. Lett. 11 (3) (2020) 1068–1074, https://doi.org/10.1021/acs.jpclett.9b03763.

[111] D. Ghosh, et al., Mixed A-cation perovskite for solar cells: atomic-scale insights into structural distortion, hydrogen bonding, and electronic peroperties, Chem. Mater. 30 (15) (2018) 5194–5204, https://doi.org/10.1021/acs.chemmater.8b01851.

[112] J.C. Yu, et al., Highly efficient and stable inverted perovskite solar cell obtained via treatment by semi-conducting chemical additive, Adv. Mater. 31 (6) (2019) 1805554, https://doi.org/10.1002/adma.201805554.

[113] Y. Chen, et al., Thermally stable methylammonium-free inverted perovskite solar cells with Zn^{2+} doped $CuGaO_2$ as efficient mesoporous hole-transporting layer, Nano Energy 61 (2019) 148–157, https://doi.org/10.1016/j.nanoen.2019.04.042.

[114] D.Y. Luo, et al., Dual-source precursor approach for highly efficient inverted planar heterojunction perovskite solar cells, Advanceed Materials 29 (19) (2017) 1604758, https://doi.org/10.1002/adma.201604758.

[115] D.Y. Luo, et al., Enhanced photovoltage for inverted planar heterojunction perovskite solar cells, Science 360 (6396) (2018) 1442–1446, https://doi.org/10.1126/science.aap9282.

[116] H.M. Zhu, et al., An effective surface modification strategy with high reproducibility for simultaneous improving efficiency and stability of inverted MA-free perovskite solar cells, J. Mater. Chem. A7 (37) (2019) 21476–21487, https://doi.org/10.1039/C9TA07238A.

[117] Z. Song, et al., Wide-bandgap, low-bandgap, and tandem perovskite solar cell, Semicond. Sci. Technol. 34 (9) (2019) 093001, https://doi.org/10.1088/1361-6641/ab27f7.

[118] J.H. Noh, et al., Chemical management for colorful, efficient, and stable inorganic–organic hybrid Nanostructured solar cells, Nano Lett. 13 (2013) 1764–1769, https://doi.org/10.1021/nl400349b.

[119] G.E. Eperon, et al., Formamidinium lead trihalide: a broadly tunable perovskite for efficient planar heterojunction solar cells, Energy Environ. Sci. 7 (2014) 982–988, https://doi.org/10.1039/C3EE43822H.

[120] E.T. Hoke, et al., Reversible photo-induced trap formation in mixed-halide hybrid perovskites for photovoltaics, Chem. Sci. 6 (2015) 613–617, https://doi.org/10.1039/C4SC03141E.

[121] D.P. McMeekin, et al., A mixed-cation lead mixed-halide perovskite absorber for tandem solar cells, Science 351 (2016) 151–155, https://doi.org/10.1126/science.aad5845.

[122] C.C. Stoumpos, et al., Semiconducting tin and lead iodide perovskites with organic cations: phase transitions, high mobilities, and near-infrared photoluminescent properties, Inorg. Chem. 52 (2013) 9019–9038, https://doi.org/10.1021/ic401215x.

[123] C. Bi, et al., Low-temperature fabrication of efficient wide-bandgap organolead trihalide perovskite solar cells, Adv. Energy Mater. 5 (2015) 1401616, https://doi.org/10.1002/aenm.201401616.

[124] M. Hu, et al., Stabilized wide bandgap MAPbBrxI3–x perovskite by enhanced grain size and improved crystallinity, Adv. Sci. 3 (2016) 1500301, https://doi.org/10.1002/advs.201500301.

[125] C. Bi, et al., Non-wetting surface-driven high-aspect-ratio crystalline grain growth for efficient hybrid perovskite solar cells, Nat. Commun. 6 (2015) 7747, https://doi.org/10.1038/ncomms8747.

[126] T. Duong, et al., Rubidium multication perovskite with optimized bandgap for perovskite-silicon tandem with over 26% efficiency, Adv. Energy Mater. 7 (2017) 1700228, https://doi.org/10.1002/aenm.201700228.

[127] Y. Yu, et al., Synergistic effects of lead thiocyanate additive and solvent annealing on the performance of wide-bandgap perovskite solar cells, ACS Energy Lett. 2 (5) (2017) 1177–1182, https://doi.org/10.1021/acsenergylett.7b00278.

[128] Y. Zhou, et al., Composition-tuned wide bandgap perovskites: from grain engineering to stability and performance improvement, Adv. Funct. Mater. 28 (2018) 1803130, https://doi.org/10.1002/adfm.201803130.

[129] Y. Zhou, et al., Benzylamine-Treated Wide-Bandgap Perovskite with High Thermal-Photostability and Photovoltaic Performance, Adv. Energy Mater. 7 1701048, https://doi.org/10.1002/aenm.201701048.

[130] X. Zheng, et al., Defect passivation in hybrid perovskite solar cells using quaternary ammonium halide anions and cations, Nat. Energy 2 (2017) 17102, https://doi.org/10.1038/nenergy.2017.102.

[131] Y. Lin, et al., Matching charge extraction contact for wide-bandgap perovskite solar cells, Adv. Mater. 29 (2017) 1700607, https://doi.org/10.1002/adma.201700607.

[132] J. Kim, et al., Amide-catalyzed phase-selective crystallization reduces defect density in wide-bandgap perovskites, Adv. Mater. 30 (2018) 1706275, https://doi.org/10.1002/adma.201706275.
[133] H. Tan, et al., Dipolar cations confer defect tolerance in wide-bandgap metal halide perovskites, Nat. Commun. 9 (2018) 3100, https://doi.org/10.1038/s41467-018-05531-8.
[134] J. Cheng, I. Choi, W. Kim, H. Li, B. Koo, M.J. Ko, ACS Appl. Mater. Interfaces 15 (19) (2023) 23077–23084, https://doi.org/10.1021/acsami.3c00895.
[135] Z. Liu, et al., Open-circuit voltages exceeding 1.26 V in planar methylammonium lead iodide perovskite solar cells, ACS Energy Lett. 4 (2019) 110–117, https://doi.org/10.1021/acsenergylett.8b01906.
[136] C.G. Bischak, et al., Origin of reversible photoinduced phase separation in hybrid perovskites, Nano Lett. 17 (2017) 1028–1033, https://doi.org/10.1021/acs.nanolett.6b04453.
[137] A.J. Knight, et al., Electronic traps and phase segregation in lead mixed-halide perovskite, ACS Energy Lett. 4 (2018) 75–84, https://doi.org/10.1021/acsenergylett.8b02002.
[138] I.L. Braly, et al., Current-induced phase segregation in mixed halide hybrid perovskites and its impact on two-terminal tandem solar cell design, ACS Energy Lett. 2 (2017) 1841–1847, https://doi.org/10.1021/acsenergylett.7b00525.
[139] Y. Lin, et al., Excess charge-carrier induced instability of hybrid perovskites, Nat. Commun. 9 (2018) 4981, https://doi.org/10.1038/s41467-018-07438-w.
[140] M.C. Brennan, S. Draguta, P.V. Kamat, M. Kuno, Light-induced anion phase segregation in mixed halide perovskites, ACS Energy Lett. 3 (2018) 204–213, https://doi.org/10.1021/acsenergylett.7b01151.
[141] D.J. Slotcavage, H.I. Karunadasa, M.D. McGehee, Light-induced phase segregation in halide-perovskite absorbers, ACS Energy Lett. 1 (2016) 1199–1205, https://doi.org/10.1021/acsenergylett.6b00495.
[142] A. Ruth, et al., Vacancy-mediated anion photosegregation kinetics in mixed halide hybrid perovskites: coupled kinetic Monte Carlo and optical measurements, ACS Energy Lett. 3 (2018) 2321–2328, https://doi.org/10.1021/acsenergylett.8b01369.
[143] G.F. Samu, C. Janáky, P.V. Kamat, A victim of halide ion segregation. How light soaking affects solar cell performance of mixed halide lead perovskites, ACS Energy Lett. 2 (2017) 1860–1861, https://doi.org/10.1021/acsenergylett.7b00589.
[144] A.J. Barker, et al., Defect-assisted photoinduced halide segregation in mixed-halide perovskite thin films, ACS Energy Lett. 2 (2017) 1416–1424, https://doi.org/10.1021/acsenergylett.7b00282.
[145] A.F. Gualdrón-Reyes, S.J. Yoon, I. Mora-Seró, Recent insights for achieving mixed halide perovskites without halide segregation, Curr. Opin. Electrochem. 11 (2018) 84–90, https://doi.org/10.1016/j.coelec.2018.09.007.
[146] K.A. Bush, et al., Compositional engineering for efficient wide band gap perovskites with improved stability to photoinduced phase segregation, ACS Energy Lett. 3 (2018) 428–435, https://doi.org/10.1021/acsenergylett.7b01255.
[147] Z. Yang, et al., Stabilized wide bandgap perovskite solar cells by tin substitution, Nano Lett. 16 (2016) 7739–7747, https://doi.org/10.1021/acs.nanolett.6b03857.
[148] M. Abdi-Jalebi, et al., Maximizing and stabilizing luminescence from halide perovskites with potassium passivation, Nature 555 (2018) 497, https://doi.org/10.1038/nature25989.
[149] R.A. Belisle, et al., Impact of surfaces on photoinduced halide segregation in mixed-halide perovskites, ACS Energy Lett. 3 (2018) 2694–2700, https://doi.org/10.1021/acsenergylett.8b01562.
[150] A.F. Gualdrón-Reyes, et al., Controlling the phase segregation in mixed halide perovskites through nanocrystal size, ACS Energy Lett. 4 (2018) 54–62, https://doi.org/10.1021/acsenergylett.8b02207.
[151] R.J. Stoddard, et al., Enhancing defect tolerance and phase stability of high-bandgap perovskites via guanidinium alloying, ACS Energy Lett. 3 (2018) 1261–1268, https://doi.org/10.1021/acsenergylett.8b00576.
[152] Z. Xiao, et al., Mixed-halide perovskites with stabilized bandgaps, Nano Lett. 17 (2017) 6863–6869, https://doi.org/10.1021/acs.nanolett.7b03179.
[153] A. Rajagopal, et al., Overcoming the photovoltage plateau in large bandgap perovskite photovoltaics, Nano Lett. 18 (2018) 3985–3993, https://doi.org/10.1021/acs.nanolett.8b01480.
[154] J.M. Howard, E.M. Tennyson, B.R.A. Neves, M.S. Leite, Machine learning for perovskites' reap-rest-recovery cycle, Joule 3 (2) (2018) 325–337, https://doi.org/10.1016/j.joule.2018.11.010.
[155] S. Chen, et al., Exploring the stability of novel wide bandgap perovskites by a robot based high throughput approach, Adv. Energy Mater. 8 (2018) 1701543, https://doi.org/10.1002/aenm.201701543.
[156] K. Yao, et al., A copper-doped nikel oxide bilayer for enhancing efficiency and stability of hysteresis-free inverted mesoporous perovskite solar cells, Nano Energy 40 (2017) 55–162, https://doi.org/10.1016/j.nanoen.2017.08.014.
[157] X.L. Yang, et al., A dopant-free twisted organic small-molecule hole transport material for inverted planar perovskite solar cells with enhanced efficiency and operational stability, Nano Energy 64 (2019) 103946, https://doi.org/10.1016/j.nanoen.2019.103946.
[158] C. Bi, et al., Non-wetting surface-driven high-aspect-ratio crystalline grain growth for efficient hybrid perovskite solar cells, Nat. Commun. 6 (1) (2015) 7747, https://doi.org/10.1038/ncomms8747.
[159] W.A. Dunlap-Shohl, et al., Synthetic approaches for halide perovskite thin films, Chem. Rev. 119 (5) (2018) 3193–3295, https://doi.org/10.1021/acs.chemrev.8b00318.
[160] G. Yang, et al., Interface engineering in planar perovskite solar cells: energy level alignment, perovskite morphology control and high performance achievement, J. Mater. Chem. A 5 (4) (2017) 1658–1666, https://doi.org/10.1039/C6TA08783C.
[161] T. Singh, et al., Sulfate-assisted interfacial engineering for high yield and perovskite solar cells with alkali-doped TiO_2 electron-transorting layers, Adv. Funct. Mater. 28 (14) (2018) 1706287, https://doi.org/10.1002/adfm.201706287.
[162] S.S. Zhang, Interface engineering of solution-processed hybrid organohalide perovskite solar cells, ACS Appl. Mater. Interfaces 10 (25) (2018) 21681–21687, https://doi.org/10.1021/acsami.8b02503.
[163] E.D. Jung, et al., Multiply charged conjugated polyelectrolytes as a multifunctional interlayer for efficient and scalable perovskite solar cells, Adv. Mater. 32 (30) (2020) 2002333, https://doi.org/10.1002/adma.202002333.
[164] J. Lee, et al., Achieving large-area planar perovskite solar cells by introducing an interfacial compatibilizer, Adv. Mater. 29 (22) (2017) 1606363, https://doi.org/10.1002/adma.201606363.
[165] X.X. Liu, et al., Multifunctional RbCl dopants for efficient inverted planar perovskite solar cell with ultral-high fill factor, negligible hysteresis and improved stability, Nano Energy 53 (2018) 567–578, https://doi.org/10.1016/j.nanoen.2018.09.023.
[166] K. Jiang, et al., Inverted planar perovskite solar cells based on CsI-doped PEDOT:PSS with efficiency beyond 20% and small energy loss, J. Mater. Chem. A 7 (38) (2019) 21662–21667, https://doi.org/10.1039/C9TA08995K.
[167] L.J. Hu, et al., Inverted planar perovskite solar cells with a high fill factor and negligible hysteresis by dual effects of NaCl-doped PEDOT:PSS, ACS Appl. Mater. Interfaces 9 (50) (2017) 43902–43909, https://doi.org/10.1021/acsami.7b14592.
[168] H. Yoon, et al., Hysteresis-free low-temperature processed planar perovskite solar cells with 9.1% efficiency, Energy Environ. Sci. 9 (7) (2016) 2262–2266, https://doi.org/10.1039/C6EE01037G, 2016.
[169] J.W. Jo, et al., Improving performance and flexibility of flexible planar-heterojunction perovskite solar cells using polymeric hole transport material, Adv. Funct. Mater. 26 (25) (2016) 4464–4471, https://doi.org/10.1002/adfm.201600746.
[170] K.G. Lim, et al., Universal energy level tailoring of self-organized hole extraction layers in organic solar cells and orgabic-inorganic hybrid perovskite solar cells, Energy Environ. Sci. 9 (3) (2016) 932–939, https://doi.org/10.1039/C5EE03560K.
[171] G. A. Al-Dainy, et al., Optimizing Lignosulfonic Acid-Grafted Polyaniline as a Hole Transport Layer for Inverted $CH_3NH_3PbI_3$ perovskite Solar Cells, ACS Omega 5(4):1887-1901, https://doi.org/10.1021/acsomega.9b03451.
[172] Y. Wu, et al., Highly efficient inverted perovskite solar cells with sulfonated ligin doped PEDOT as hole extract layer, ACS Appl. Mater. Interfaces 8 (19) (2016) 12377–12383, https://doi.org/10.1021/acsami.6b00084.

[173] Y. Li, et al., Poly (3, 4-Ethylenenedioxythiophene): methylnaphthalene sulfonate: the effect of work function and structural homogeneity on hole injection/extraction, Adv. Energy Mater. 7 (6) (2017) 1601499, https://doi.org/10.1002/aenm.201601499.
[174] C.T. Zuo, L.M. Ding, Modified PEDOT layer makes a 1.5V Voc for perovskite/PCBM solar cells, Adv. Energy Mater. 7 (2) (2017) 1601193, https://doi.org/10.1002/aenm.201601193.
[175] D.Y. Liu, et al., Improved performance of inverted planar perovskite solar cells with F4-TCNQ doped PEDOT:PSS hole transport layers, Mater. Chem. 5 (12) (2017) 5701–5708, https://doi.org/10.1039/C6TA10212C.
[176] Q.F. Xue, et al., Efficient and stable perovskite solar cells vid dual functionalization of dopamine semiquinone radical with improved trap passivation capabilities, Adv. Funct. Mater. 28 (18) (2018) 1707444, https://doi.org/10.1002/adfm.201707444.
[177] Q. Wang, et al., Modulation of PEDOT:PSS pH for efficient inverted perovskite solar cells with reduced potential loss and enhanced stability, ACS Appl. Mater. Interfaces 8 (46) (2016) 32068–32076, https://doi.org/10.1021/acsami.6b11757.
[178] T.C. Tsai, et al., A facial dedoping approach for effective tuning thermoelectricity and acidity of PEDOT:PSS films, Org. Electron. 15 (3) (2014) 641–645, https://doi.org/10.1016/j.orgel.2013.12.023.
[179] P. Qin, et al., Inorganic hole conductor-based lead halide perovskite solar cells with 12.4% conversion efficiency, Nat. Commun. 5 (1) (2014) 3834, https://doi.org/10.1038/ncomms4834.
[180] Y. Liu, et al., High-performance inverted perovskite solar cells using doped poly (triarylamine) as the hole transport layer, ACS Appl. Energy Mater. 2 (3) (2019) 1932–1942, https://doi.org/10.1021/acsaem.8b02047.
[181] F.H. Isikgor, et al., Scaling-up perovskite solar cells on hydrophobic surfaces, Nano Energy 81 (2021) 105633.
[182] J. You, et al., The fabrication of homogeneous perovskite films on nonwetting interfaces enabled by physical modification, J. Energy Chem. 38 (2019) 192–198, https://doi.org/10.1021/acsaem.8b02047.
[183] X. Liu X, et al., 20.7% highly reproducible inverted planar perovskite solar cells with enhanced fill factor and eliminated hysteresis, Energy Environ. Sci. 12 (2019) 1622–1633, https://doi.org/10.1039/C9EE00872A.
[184] R. Chen, et al., Robust hole transport material with interface anchors enhances the efficiency and stability of inverted formamidinium–cesium perovskite solar cells with a certified efficiency of 22.3, Energy Environ. Sci. 15 (2022) 2567–2580, https://doi.org/10.1039/D2EE00433J.
[185] X. Sun, et al., Efficient inverted perovskite solar cells with low voltage loss achieved by a pyridine-based dopant-free polymer semiconductor, Angew. Chem. Int. Ed. 60 (2021) 7227–7233, https://doi.org/10.1039/D2EE00433J.
[186] X. Xu, et al., Improving contact and passivation of buried interface for high efficiency and large-area inverted perovskite solar cells, Adv. Funct. Mater. 32 (2022) 2109968, https://doi.org/10.1002/adfm.202109968.
[187] Y. Yao, et al., Organic hole transport layers for efficient, stable and scalable inverted perovskite solar cells, Adv. Mater. 34 (2022) 2203794, https://doi.org/10.1002/adma.202203794.
[188] Y. Wang, et al., Teaching an old anchoring group new tricks: enabling lowcost, eco-friendly hole-transporting materials for efficient and stable perovskite solar cells, J. Am. Chem. Soc. 142 (2020) 16632–16643, https://doi.org/10.1021/jacs.0c06373.
[189] L. Zhang, et al., Hole-transporting layer based on a conjugated polyelectrolyte with organic cations enables efficient inverted perovskite solar cells, Nano Energy 57 (2019) 248–255, https://doi.org/10.1016/j.nanoen.2018.12.033.
[190] A. Ullah, et al., Versatile hole selective molecules containing a series of heteroatoms as self-assembled monolayers for efficient p-i-n perovskite and organic solar cells, Adv. Funct. Mater. 32 (2022) 2208793, https://doi.org/10.1002/adfm.202208793.
[191] G.H. Kim, et al., High-efficiency colloidal quantum dot photovoltaics via robust self-assembled monolayers, Nano Lett. 15 (2015) 7691–7696, https://doi.org/10.1021/acs.nanolett.5b03677.
[192] A. Magomedov, et al., Self-assembled hole transporting monolayer for highly efficient perovskite solar cells, Adv. Energy Mater. 8 (2018) 1801892, https://doi.org/10.1002/aenm.201801892.
[193] A. Al-Ashouri, et al., Conformal monolayer contacts with lossless interfaces for perovskite single junction and monolithic tandem solar cells, Energy Environ. Sci. 12 (2019) 3356–3369, https://doi.org/10.1039/C9EE02268F.
[194] A. Al-Ashouri, et al., Monolithic perovskite/silicon tandem solar cell with >29% efficiency by enhanced hole extraction, Science 370 (2020) 1300–1309, https://doi.org/10.1039/C9EE02268F.
[195] X. Deng, et al., Co-assembled monolayers as hole-selective contact for high-performance inverted perovskite solar cells with optimized recombination loss and long-term stability, Angew. Chem. Int. Ed. 60 (31) (2022), https://doi.org/10.1002/anie.202203088.
[196] Q. Liao, et al., Self-assembled donor-acceptor hole contacts for inverted perovskite solar cells with an efficiency approaching 22%: the impact of anchoring groups, J. Energy Chem. 68 (2022) 87–95, https://doi.org/10.1016/j.jechem.2021.11.001.
[197] W. Chen, et al., Engineering of dendritic dopant-free hole transport molecules: enabling ultrahigh fill factor in perovskite solar cells with optimized dendron construction, Sci. China Chem. 64 (2021) 41–51, https://doi.org/10.1007/s11426-020-9857-1.
[198] Y. Wang, et al., Dopant-free small-molecule hole-transporting material for inverted perovskite solar cells with efficiency exceeding 21, Adv. Mater. 31 (2019) 1902781, https://doi.org/10.1002/adma.201902781.
[199] S. Chen, X. Xiao, H. Gu, J. Huang, Iodine reduction for reproducible and high-performance perovskite solar cells and modules, Sci. Adv. 7 (10) (2021), https://doi.org/10.1126/sciadv.abe8130.
[200] H. Choi, et al., Congugated polyelectrolyte hole transport layer for inverted-type perovskite solar cells 6 (1) (2015) 7348, https://doi.org/10.1038/ncomms8348.
[201] H. Zhang, et al., Low-temperature solution-processed $CuCrO_2$ hole-transporting layer for efficient and photostable perovskite solar cells, Adv. Energy Mater. 8 (13) (2018) 1702762, https://doi.org/10.1002/aenm.201702762.
[202] G. Kakavelakis, et al., Extending the continuous operating lifetime of perovskite solar cells with a molybdenum disulfide hole extraction interlayer, Adv. Energy Mater. 8 (12) (2018) 1702287, https://doi.org/10.1002/aenm.201702287.
[203] Y. Chen, et al., Thermally stable methylammonium-free inverted perovskite solar cells with Zn2+ doped CuGaO2 as efficient mesoporous holetransporting layer, Nano Energy 61 (2019) 148–157, https://doi.org/10.1016/j.nanoen.2019.04.042.
[204] H. Zhang, et al., Low-temperature solution-processed CuCrO2 hole-transporting layer for efficient and photostable perovskite solar cells, Adv. Energy Mater. 8 (2018) 1702762, https://doi.org/10.1002/aenm.201702762.
[205] G. Kakavelakis, et al., Extending the continuous operating lifetime of perovskite solar cells with a molybdenum disulfide hole extraction interlayer, Adv. Energy Mater. 8 (2018) 1702287, https://doi.org/10.1002/aenm.201702287.
[206] F. Ma, et al., Nickel oxide for inverted structure perovskite solar cells, J. Energy Chem. 52 (2021) 393–411, https://doi.org/10.1016/j.jechem.2020.04.027.
[207] Y. Wei, et al., Improving the efficiency and environmental stability of inverted planar perovskite solar cells via silver-doped nickel oxide hole-transporting layer, Appl. Surf. Sci. 427 (2018) 782–790, https://doi.org/10.1016/j.apsusc.2017.08.184.
[208] S. Xiao, et al., An ultra-low concentration of gold nanoparticles embedded in the NiO hole transport layer boosts the performance of p-i-n perovskite solar cells, Sol. RRL 3 (2) (2019) 1800278, https://doi.org/10.1002/solr.201800278.
[209] W. Chen, et al., Understanding the doping effect on NiO: toward highperformance inverted perovskite solar cells, Adv. Energy Mater. 8 (19) (2018) 1703519, https://doi.org/10.1002/aenm.201703519.
[210] W. Chen, et al., Cesium doped NiOx as an efficient hole extraction layer for inverted planar perovskite solar cells, Adv. Energy Mater. 7 (19) (2017) 1700722, https://doi.org/10.1002/aenm.201700722.
[211] W. Chen, et al., Alkali chlorides for the suppression of the interfacial recombination in inverted planar perovskite solar cells, Adv. Energy Mater. 9 (19) (2019) 1803872, https://doi.org/10.1002/aenm.201803872.
[212] W. Chen, et al., Efficient and stable large-area perovskite solar cells with inorganic charge extraction layers, Science 350 (2015) 944–948, https://doi.org/10.1126/science.aad1015.

[213] W. Chen, et al., Molecule-doped nickel oxide: verified charge transfer and planar inverted mixed cation perovskite solar cell, Adv. Mater. 30 (20) (2018) 1800515, https://doi.org/10.1002/adma.201800515.
[214] P. Ru, et al., High electron affinity enables fast hole extraction for efficient flexible inverted perovskite solar cells, Adv. Energy Mater. 10 (2020) 1903487, https://doi.org/10.1002/aenm.201903487.
[215] C.C. Boyd, et al., Overcoming redox reactions at perovskite-nickel oxide interfaces to boost voltages in perovskite solar cells, Joule 4 (8) (2020) 1759–1775, https://doi.org/10.1016/j.joule.2020.06.004.
[216] T. Wu, et al., Elimination of light-induced degradation at the nickel oxideperovskite heterojunction by aprotic sulfonium layers towards long-term operationally stable inverted perovskite solar cells, Energy Environ. Sci. 15 (2022) 4612–4624, https://doi.org/10.1039/D2EE01801B.
[217] X. Zhu, et al., Inverted planar heterojunction perovskite solar cells with high ultraviolet stability, Nano Energy 103 (2022) 107849, https://doi.org/10.1016/j.nanoen.2022.107849.
[218] B. Yang, S. Peng, W.C. Choy, Inorganic top electron transport layer for high performance inverted perovskite solar cells, EcoMat 3 (5) (2021), https://doi.org/10.1002/eom2.12127.
[219] M. Kim, et al., Conformal quantum dot–SnO_2 layers as electron transporters for efficient perovskite solar cells, Science 375 (2022) 302–306.
[220] R. Fang, et al., [6, 6]-Phenyl-C61-butyric acid methyl ester/cerium oxide bilayer structure as efficient and stable electron transport layer for inverted perovskite solar cells, ACS Nano 12 (3) (2018) 2403–2414, https://doi.org/10.1021/acsnano.7b07754.
[221] J. Troughton, et al., A universal solution processed interfacial bilayer enabling ohmic contact in organic and hybrid optoelectronic devices, Energy Environ. Sci. 13 (2020) 268–276, https://doi.org/10.1039/C9EE02202C.
[222] R. Lin, et al., All-perovskite tandem solar cells with improved grain surface passivation, Nature 603 (2022) 73–78, https://doi.org/10.1038/s41586-021-04372-8.
[223] K. Xiao, et al., Scalable processing for realizing 21.7%-efficient all-perovskite tandem solar modules, Science 376 (2022) 762–767, https://doi.org/10.1126/science.abn7696.
[224] K. A. Bush, et al., Thermal and environmental stability of semi-transparent perovskite solar cells for tandems enabled by a solution-processed nanoparticle buffer layer and sputted ITO electrode, Adv. Mater. 28(20)3937-3943, https://doi.org/10.1002/adma.201505279.
[225] Z. Zhu, et al., Enhanced efficiency and sability of inverted perovskite solar cells using highly crystalline SnO_2 nanocrystals as the robust electron-transporting layer, Adv. Mater. 28 (30) (2016) 6478–6484, https://doi.org/10.1002/adma.201600619.
[226] K.O. Brinkmann, et al., Suppressed decomposition of the organometal halide perovskites by impermeable electron-extraction layers in inverted solar cells, Nat. Commun. 8 (1) (2017) 13938, https://doi.org/10.1038/ncomms13938.
[227] S. Seo, et al., Perovskite solar cells with inorganic electron and hole-transport layers exhibiting long-term (approx. 500 h) stability at 85^{o}C under continuous 1 sun illumination in ambient air, Adv. Mater. 30 (29) (2018) 1801010, https://doi.org/10.1002/adma.201801010.
[228] S. Guo, et al., Non-uniform chemical corrosion of metal electrode of p–i–n type of perovskite solar cells caused by the diffusion of CH_3NH_3I, Energy Technol. 8 (2020) 2000250, https://doi.org/10.1002/ente.202000250.
[229] C. Chen, et al., Effect of BCP buffer layer on eliminating charge accumulation for high performance of inverted perovskite solar cells, RSC Adv. 7 (2017) 35819–35826, https://doi.org/10.1039/C7RA06365B.
[230] S. Wu, et al., A chemically inert bismuth interlayer enhances long-term stability of inverted perovskite solar cells, Nat. Commun. 10 (2019) 1–11, https://doi.org/10.1038/s41467-019-09167-0.
[231] X. Li, et al., Chemical anti-corrosion strategy for stable inverted perovskite solar cells, Sci. Adv. 6 (51) (2020), https://doi.org/10.1126/sciadv.abd1580.
[232] X. Lin, et al., Efficiency progress of inverted perovskite solar cells, Energy Environ. Sci. 13 (2020) 3823–3847, https://doi.org/10.1039/D0EE02017F.
[233] B. Parida, et al., Boosting the conversion efficiency over 20% in $MAPbI_3$ perovskite planar solar cells by employing a solution-processed aluminum doped nickel oxide hole collector, ACS Appl. Mater. Interfaces 12 (2020) 22958–22970, https://doi.org/10.1021/acsami.0c04618.
[234] W. Chen, et al., Metal acetylacetonate series in interface engineering for full low-temperature-processed, high-performance, and stable planar perovskite solar cells with conversion efficiency over 16% on 1 cm2 scale, Adv. Mater. 29 (2017) 1603923, https://doi.org/10.1002/adma.201603923.
[235] J. Ning, et al., Gaining insight into the effect of organic interface layer on suppressing ion migration induced interfacial degradation in perovskite solar cells, Adv. Funct. Mater. 30 (2020) 2000837, https://doi.org/10.1002/adfm.202000837.
[236] K.O. Brinkmann, et al., Suppressed decomposition of organometal halide perovskites by impermeable electron-extraction layers in inverted solar cells, Nat. Commun. 8 (2017) 13938, https://doi.org/10.1038/ncomms13938.
[237] S. Zhang, et al., Barrier designs in perovskite solar cells for long-term stability, Adv. Energy Mater. 10 (2020) 2001610, https://doi.org/10.1002/aenm.202001610.
[238] T. Gahlmann, et al., Impermeable charge transport layers enable aqueous processing on top of perovskite solar cells, Adv. Energy Mater. 10 (2020) 1903897, https://doi.org/10.1002/aenm.201903897.
[239] T. Wahl, et al., Sputtered indium zinc oxide rear electrodes for inverted semitransparent perovskite solar cells without using a protective buffer layer, Org. Electron. 54 (2018) 48–53, https://doi.org/10.1016/j.orgel.2017.12.020.
[240] J. Xu, et al., Triple-halide wide–band gap perovskites with suppressed phase segregation for efficient tandems, Science 367 (2020) 1097–1104, https://doi.org/10.1126/science.aaz5074.
[241] S. Ye, et al., CuSCN-based inverted planar perovskite solar cell with an average PCE of 15.6, Nano Lett. 15 (6) (2015) 3723–3728, https://doi.org/10.1021/acs.nanolett.5b00116.
[242] S. Liu, et al., Boost the efficiency of nickel oxide-based formamidinium-cesium perovskite solar cells to 21% by using coumarin 343 dye as defect passivator, Nano Energy 94 (2022) 106935, https://doi.org/10.1016/j.nanoen.2022.106935.
[243] Z. Liu, et al., Additives inmetal halide perovskite films and their applications in solar cells, J. Energy Chem. 46 (2020) 215–228, https://doi.org/10.1016/j.jechem.2019.11.008.
[244] S. Xiong, et al., Direct observation on p- to n-type transformation of perovskite surface region during defect passivation driving high photovoltaic efficiency, Joule 5 (2021) 467–480, https://doi.org/10.1016/j.joule.2020.12.009.
[245] K. Liu, et al., Zwitterionic-surfactant-assisted room-temperature coating of efficient perovskite solar cells, Joule 4 (2020) 2404–2425, https://doi.org/10.1016/j.joule.2020.09.011.
[246] M. Jiang, et al., Engineering green-to-blue emitting $CsPbBr_3$ quantum-dot films with efficient ligand passivation, ACS Energy Lett. 4 (2019) 2731–2738, https://doi.org/10.1021/acsenergylett.9b02032.
[247] C. Liu, et al., Tuning structural isomers of phenylenediammonium to afford efficient and stable perovskite solar cells and modules, Nat. Commun. 12 (2021) 1–9, https://doi.org/10.1038/s41467-021-26754-2.
[248] S. Liu, et al., Effective passivation with size-matched alkyldiammonium iodide for high-performance inverted perovskite solar cells, Adv. Funct. Mater. 32 (2022) 2205009, https://doi.org/10.1002/adfm.202205009.
[249] Q. Cao, et al., Efficient and stable inverted perovskite solar cells with very high fill factors via incorporation of star-shaped polymer, Sci. Adv. 7 (2021), https://doi.org/10.1126/sciadv.abg0633.
[250] Q. Cao, et al., Star-polymer multidentate-cross-linking strategy for superior operational stability of inverted perovskite solar cells at high efficiency, Energy Environ. Sci. 14 (2021) 5406–5415, https://doi.org/10.1039/D1EE01800K.
[251] M. Stolterfoht, et al., The impact of energy alignment and interfacial recombination on the internal and external open-circuit voltage of perovskite solar cells, Energy Environ. Sci. 12 (2019) 2778–2788, https://doi.org/10.1039/C9EE02020A.
[252] P. Caprioglio, et al., On the relation between the open-circuit voltage and quasi-fermi level splitting in efficient perovskite solar cells, Adv. Energy Mater. 9 (2019) 1901631, https://doi.org/10.1002/aenm.201901631.
[253] M. Du, et al., Surface redox engineering of vacuum-deposited NiOx for top-performance perovskite solar cells and modules, Joule 6 (2022) 1931–1943, https://doi.org/10.1016/j.joule.2022.06.026.

[254] Y. Li, et al., Recent progress of critical interface engineering for highly efficient and stable perovskite solar cells, Adv. Energy Mater. 12 (2022) 2102730, https://doi.org/10.1002/aenm.202102730.
[255] N. Fakhri, et al., Simulation of perovskite solar cells optimized by the inverse planar method in SILVACO: 3D electrical and optical models, Energies 14 (18) (2021) 5944, https://doi.org/10.3390/en14185944.
[256] H. Hu, L. Schmidt-Mende, P. Baun, The Fabrication, Characterization and Simulation of Inverted Perovskite Solar Cells, PhD Thesis, Department of Physics, Faculty of Mathematics and Natural Sciences, Universitat, Kontanz, 2019, p. 12.
[257] S. Ma, et al., Efficient and flexible solar cells with improved stability through incorporation of a multifunctional small molecule at PEDOT:PSS/perovskite interface, Sol. Energy Mater. Sol. Cell. 208 (2020) 110379, https://doi.org/10.1016/j.solmat.2019.110379.
[258] M. Younas, M.A. Gondal, M.A. Dastageer, M. A. Fabrication of perovskite solar cells using novel 2D/3D-blended perovskite single crystals, Int. J. Energy Res. (2020) 1–12, https://doi.org/10.1002/er.6183.
[259] Q. Ping, et al., High-performance rigid and flexible perovskite solar cells with low-temperature solution processable binary metal oxide hole-transporting materials, Sol. RRL 1 (8) (2017) 1700058, https://doi.org/10.1002/solr.201700058.
[260] L.Q. Ping, Copper-doped chromium oxide hole-transporting layer for perovskite solar cells: interface engineering and performance improvement, Adv. Mater. Interfac. 3 (14) (2016) 1500799, https://doi.org/10.1002/admi.201500799.
[261] C.W. Chen, et al., Efficient and uniform planar-type perovskite solar cells by simple sequential vacuum deposition, Adv. Mater. 26 (38) (2014) 6647–6652, https://doi.org/10.1002/adma.201402461.
[262] X. Jiang, et al., High-performance regular perovskite solar cells employing low-cost poly(ethylenedioxythiophene) as a hole-transporting material, Sci. Rep. (7) (2017), https://doi.org/10.1038/srep42564. ID42564.
[263] L. Hao, et al., A tin-based perovskite solar cell with an inverted hole-free transport layer to achieve high energy conversion efficiency by SCAPS device simulation, Opt. Quant. Electron. 53 (2021) 524, https://doi.org/10.1007/s11082-021-03175-5.
[264] M.S. Shamna, et al., Simulation and optimization of $CH_3NH_3SnI_3$ based inverted perovskite solar cell with NiO as Hole transport material, Mater. Today: Proc. 33 (2) (2020) 1246–1251, https://doi.org/10.1016/j.matpr.2020.03.488.
[265] S. Rahman, Simulation based investigation of inverted planar perovskite solar cell withAll metal oxide inorganic transport layers, in: Proceedings of the 2019 International Conference on Electrical, Computer and Communication Engineering (ECCE), Cox's Bazar, Bangladesh, February, 2019, https://doi.org/10.1109/ECACE.2019.8679283, 7–9.
[266] M. Goudarzi M. Banihashemi, Simulation of an inverted perovskite solar cell with inorganic electron and hole transfer layers, J. Photon. Energy 7 (2) (2017), https://doi.org/10.1117/1.JPE.7.022001.
[267] J. Gong, S. Krishnan, Simulation of Inverted Perovskite Solar Cells. Proceedings of the ASME 201812th International Conference on Energy Sustainability, LakeBuena Vista, FL, USA, 2018, pp. 24–28, https://doi.org/10.1115/ES2018-7227. June.
[268] M. Stolterfoht, et al., Visualization and suppression of interfacial recombination for high-efficiency large-area pin perovskite solar cells, Nat. Energy 3 (10) (2018) 847–854, https://doi.org/10.1038/s41560-018-0219-8.
[269] S.Z. Yue, et al., Efficacious engineering on charge extraction for realizing highly efficient perovskite solar cells, Energy Environ. Sci. 10 (12) (2017) 2570–2578, https://doi.org/10.1039/C7EE02685D.
[270] S. Chatterjee, A.J. Pal, Introducing Cu_2O thin films as a hole-transport layer in efficient planar perovskite solar cell structure, J. Phys. Chem. C 120 (3) (2016) 1428–1437, https://doi.org/10.1021/acs.jpcc.5b11540.
[271] N. Arora, et al., Perovskite solar cells with CuSCN hole extraction layers yield stabilized efficiencies greater than 20, Science 358 (6364) (2017) 768–771, https://doi.org/10.1126/science.aam5655.
[272] E. Jokar, et al., Anomalous charge-extraction behavior for graphene-oxide (rGO) films as efficient p-contact layers for high-performance perovskite solar cells, Adv. Energy Mater. 8 (3) (2018) 1701640, https://doi.org/10.1002/aenm.201701640.
[273] E.B. Bi, et al., Efficient perovskite solar cell modules with high stability enabled by iodide diffusion barriers, Joule 3 (11) (2019) 2748–2760, https://doi.org/10.1016/j.joule.2019.07.030.
[274] Y.Z. Lin, et al., Matching charge extraction contact for widw-bandgap perovskitesolar cells, Adv. Mater. 29 (26) (2017) 1700607, https://doi.org/10.1002/adma.201700607.
[275] S.K. Jung, et al., Nonfullerene electron transporting material based on naphthalene diimide small molecule for highly stable perovskite solar cells with efficiency exceeding 20, Adv. Funct. Mater. 28 (20) (2018) 800346, https://doi.org/10.1002/adfm.201800346.
[276] R. Azmi, et al., High-efficency low-temperature ZnO based perovskite solar cells based on highly polar, nonwetting self-assembled molecular layers, Adv. Energy Mater. 8 (5) (2018) 1701683, https://doi.org/10.1002/aenm.201701683.
[277] S. Sutthana, et al., Interface modification of $CH_3NH_3PbI_3$/PCBM by pre-heat treatment for efficiency enhancement of perovskite solr cells, Curr. Appl. Phys. 17 (4) (2017) 488–494, https://doi.org/10.1016/j.cap.2017.01.015.
[278] Y. Hou, et al., A band-edge potential gradient heterostructure to enhance electron extraction efficiency of the electron transport layer in high-performance perovskite solar cells, Adv. Funct. Mater. 27 (27) (2017) 1700878, https://doi.org/10.1002/adfm.201700878.
[279] D.B. Khadka, Y. Shirai, M. Yanagida, K. Miyano, Insights into accelerated degradation of perovskite solar cells under continuous illumination driven by thermal stress and interfacial junction, ACS Appl. Energy Mater. 4 (2021) 11121–11132, https://doi.org/10.1021/acsaem.1c02037.
[280] M. Wong-Stringer, et al., High-performance multilayer encapsulation for perovskite photovoltaics, Adv. Energy Mater. 8 (2018) 1801234, https://doi.org/10.1002/aenm.201801234.
[281] Z. Wang, et al., Applications of machine learning in perovskite materials, Adv. Compos. Hybrid Mater. 5 (2022) 2700–2720, https://doi.org/10.1007/s42114-022-00560-w.